Spring 5-15-2020

First-principles Studies of Anion Engineering in Functional Ceramics

Steven Timothy Hartman

Washington University in St. Louis

Recommended Citation

Hartman, Steven Timothy, "First-principles Studies of Anion Engineering in Functional Ceramics" (2020). *McKelvey School of Engineering Theses & Dissertations*. 544.
https://openscholarship.wustl.edu/eng_etds/544

WASHINGTON UNIVERSITY IN ST. LOUIS

Institute of Materials Science and Engineering

Dissertation Examination Committee:
Rohan Mishra, Chair
Zohar Nussinov
Vijay Ramani
Bryce Sadtler
Elijah Thimsen

First-principles Studies of Anion Engineering in Functional Ceramics
by
Steven Timothy Hartman

A dissertation presented to
The Graduate School
of Washington University in
partial fulfillment of the
requirements for the degree
of Doctor of Philosophy

May 2020
St. Louis, Missouri

Table of Contents

List of Figures

Acknowledgments

First, I would like to thank my adviser, Prof. Rohan Mishra, for his help and advice over the last 4 years. I've learned a lot from him, not just technical knowledge about electronic materials, but also the other aspects of a scientific career, such as giving effective presentations. In addition, I thank my committee members for generously offering their time to review my thesis work. I'm also grateful to the other members of the M-Cube lab for their help, especially Arashdeep Thind, who has provided several very useful Python scripts as well as advice on VASP calculation parameters. Seeking out low-budget conference lodging simply won't be the same without him. On the administrative side, Beth Gartin has enabled me to navigate paperwork requirements with minimal difficulty.

The work would not have been possible without the funding from several sources. The oxyfluoride multiferroics research and YBCO vacancy study were supported by NSF grants CBET-1729787 and DMR-1806147, and the Consortium for Clean Coal Utilization at Washington University. Computational resources for all projects were provided by the eXtreme Science and Engineering Discovery Environment (XSEDE), which is supported by the NSF ACI-1053575 and ACI-1548562 grants.

Finally, I'd like to thank the people who supported me personally while I did this research. Cameron and Elsa Puffenberger not only convinced me to apply to Washington University in the first place, they also shared an apartment with me for my first year, which was a great help both socially and financially. Most importantly, my wife Amanda has filled the last four years with happiness, and I look forward to a lifetime of loving her. Nothing I achieve in my scientific career will ever bring me as much satisfaction as her companionship.

Steven Hartman

Washington University in St. Louis

May 2020

ABSTRACT OF THE DISSERTATION

First-principles Anion Engineering of Functional Ceramics

by

Steven Timothy Hartman

Doctor of Philosophy in Materials Science and Engineering

Washington University in St. Louis, 2020

Assistant Professor Rohan Mishra, Chair

Ceramic materials display a wide variety of valuable properties, such as ferroelectricity, superconductivity, and magnetic ordering, due to the partially covalent bonds which connect the cations and anions. While many breakthroughs have been made by mixing multiple cations on a sublattice, the equivalent mixed-anion ceramics have not received nearly as much attention, despite the key role the anion plays in the materials' properties. There is great potential for functional ceramics design using anion engineering, which aims to tune the materials properties by adding and removing different types of anions in existing classes of ceramic materials. In this dissertation, I present our theoretical studies, — supplemented by experiments, where available, — of : 1) oxygen vacancies in superconducting oxides, 2) oxyfluorides to achieve multiferroic materials, 3) oxynitrides-based ferroelectric semiconductors, and 4) electride-based materials predicted to serve as promising fluorine-ion intercalation batteries.

First, I will set the stage by describing the functions which we seek to gain or improve by anion engineering, and the theoretical methods which we use to predict improved materials. The first topic is the crystal site preference of oxygen vacancies in the high-temperature superconductor $YBa_2Cu_3O_{7-x}$ (YBCO). We find that it is favorable to form a small concentration of apical oxygen vacancies, in addition to the well-studied vacancies in the Cu-O chains. I will also show new experimental evidence that this apical vacancy occurs frequently under some conditions. Next, I describe our research on transition metal oxyfluoride perovskites. We predict that low-temperature fluorination of anion-deficient iron and manganese oxides can lead to multiferroic compounds with simultaneous ferroelectric and magnetic ordering. In the third topic, we employ a similar strategy of anion substitution to search for ABO_2N semiconductors, where B is a *p*-block element. We propose a new class of stable tin oxynitrides-based ferroelectric semiconductors. These oxynitrides have tunable bandgaps across the entire visible spectrum, in addition to light electron effective masses which are expected to promote electrical conductivity. The new materials are also non-centrosymmetric, with a large polarization which may lead to switchable ferroelectricity. Finally, I will examine a new family of fluoronitrides and fluorocarbides that we predict to serve as fluorine-ion intercalation electrodes for use in high-capacity batteries. These materials utilize the unique chemistry of electrides to achieve excellent voltage and diffusion kinetics. Together, these examples demonstrate the power of anion engineering to create new functional ceramics with desirable properties.

Chapter 1: Properties and Potential of Mixed-Anion Ceramics

Ceramics are a broad class of insulating or semiconducting materials characterized by strong, partially ionic bonding between positively charged cations and negatively charged anions. Ceramics have been prized since ancient times, with heat- and water-resistant fired clays used extensively for practical or artistic purposes, but the modern applications of ceramics now often depend on the functions they exhibit in response to a stimulus, and are referred to as functional ceramics. Due to the urgency of the technological challenges facing modern society, there is a great effort to accelerate the development of new functional ceramics, and the optimization of existing ones, beyond the speed of conventional trial-and-error synthesis.[1] The first section of this chapter will briefly review the recent rise of anion engineering in ceramic materials, a technique which adds and removes negatively charged ions to tune the properties of functional materials. The relatively small number of existing studies of anion engineering have already made remarkable achievements, illustrating its great but mostly unexplored potential. In the second, I will outline some of the valuable functionalities which can be optimized using anion engineering techniques, to provide background for the detailed research reports presented in Chapters 3-6.

1.1 Anion Engineering

Since the anion-cation bonding dictates ceramic materials' properties, it follows that the properties can be tuned by changing the composition and ordering of the two sublattices. While simply replacing or adding one ion can create powerful modifications, constraints such as charge balance and ionic radii mismatch sometimes require simultaneous modification of both sublattices. Therefore, it is necessary to control the anion sublattice in order to have full control of a material's properties. Here, I will illustrate the potential of anion engineering by briefly reviewing the current status of mixed-anion ceramics research.

1.1.1 Anion Vacancies

The simplest kind of anion engineering is the control of anion vacancy concentrations and their order in materials with a single type of anion. Vacancy control offers a "dial" to adjust several relevant properties. Perhaps the most important is electron doping; if the anion has an ionic charge of $-n$, then each neutral anion vacancy effectively donates n electrons to the surrounding crystal lattice. This can be observed in many complex metal oxides, because oxygen vacancies are relatively stable in such materials and can be created by annealing at high temperatures.[1] For example, annealing TiO_2 at 200-550 °C creates oxygen vacancies and reduces some of the Ti^{4+} to Ti^{3+}, boosting the oxide's efficiency for photocatalytic water splitting above 1%.[2] Creating anion vacancies also greatly enhances a ceramic's ionic conductivity, since the remaining anions have empty sites to pass through as they diffuse. Besides annealing, cation substitution also offers control of the anion vacancy concentration through charge balance; a solid solution of $La_{1-x}Ba_xF_{3-x}$ has the same structure as LaF_3 for small Ba^{2+} concentrations, but the introduction of F^- vacancies with Ba^{2+} addition increases fluoride conductivity by an order of magnitude.[3]

1.1.2 Oxyfluorides

Even more control over the materials' properties can be obtained through the use of heteroanionic materials, which have an anion sublattice with two or more anions.[4,5] Although the introduction of a second anion has received less attention than cation engineering, it is now emerging as another promising route to control ceramic properties.[6-8] The two anions will differ in important properties, most notably electronegativity, ionic charge and size, and this will tune the properties of the cation-anion bonding. One of the oldest and best studied families of heteroanionic ceramics are the oxyfluorides.[9,10]

Replacing oxygen with fluorine, while keeping the cation fixed, makes the compound more ionic, since fluorine is the most electronegative element at 3.98 on the Pauling scale, compared to oxygen at 3.44.[11] Fluoride's charge of –1, compared to oxide's –2, also reduces the oxidation state of metal cations if oxygen is replaced with fluorine. An early application for fluorination of metal oxides was the electron doping of superconductors,[12] in which fluoride substitution acted as a complementary technique to oxide vacancy creation. The oxyfluoride $Sr_{1.4}Ba_{0.6}CuO_2F_{2+\delta}$ is superconducting up to 64 K, warmer than any other known material in the La_2CuO_4 structural family.[12] Electron doping by fluorination has also been applied to transition metal oxide thin films to tune their conductivity and magnetism. For example, fluorination of a thin film of $SrFeO_{3-\delta}$ reduced the film's electrical resistance by five orders of magnitude[13], by creating a Fe^{3+}/Fe^{4+} mixed-valence state. Fluorination of $NdNiO_3$ changed it from a semiconductor with 2.1 eV band gap to a metal.[14] Fluorination can also strengthen magnetic ordering by changing the cation *d*-electron configuration to one which has stronger interactions between cations.[15,16] This approach was used in $BaFeO_{3-\delta}F_x$ to increase its Néel temperature (T_N), above which it transitions from an antiferromagnet to a paramagnet, >700 K, compare to a T_N of 130 K in $BaFeO_3$.[15]

Fluorination is not only used to tune the electronic properties of materials; the differences between F^- and O^{2-} can also have significant consequences for the oxyfluorides' crystal structure.

Many studies have also attempted to create non-centrosymmetric oxyfluorides,[17-21] based on Chen et al.'s anionic group theory of second harmonic generation.[22] According to this theory, the optical second harmonic generation of a crystal is dominated by local interactions within asymmetric anionic polyhedra, with the essentially spherical cations playing little role. With this principle in mind, it is natural to break the symmetry by incorporating multiple anions into the same polyhedron. Mixed-anion octahedra such as MOF_5 offer result in local symmetry breaking, since the difference between oxide and fluoride bonds generates a large dipole – up to 6.1 Debye for the MoO_3F_3 octahedra within $Ag_6Mo_2O_7ClF_3$.[21,23,24] However, local symmetry breaking is not enough for many applications; designing non-centrosymmetric materials requires an understanding of the anion order across multiple scales, as the averaged crystal structure may be centrosymmetric due to disorder even if the individual polyhedra are polar.[25] Alternately, the anion-ordered polyhedra may come in oppositely oriented pairs, resulting in no net polarization.[19,26,27] It is challenging to determine the effect of anion ordering on structural symmetry, because oxide and fluoride are difficult to distinguish by diffraction techniques alone.[28-30] Some insight could be gained by empirical methods based on Pauling's second crystal rule,[31] such as bond valence sum calculations,[29,32] but a detailed study found that these rules predicted the anion ordering incorrectly about 20% of the time,[33] even if the accurate atomic positions were already known from experiment. Recent advances in first-principles calculations are helpful in these studies for calculating the most stable anion ordering, especially in novel systems that have not yet been characterized experimentally.[34-36]

Despite the structural changes associated with solid-state fluorination, this reaction does not necessarily require a complete rebuilding of the crystal structure. Many of these applications of solid-state fluorination utilize topochemical transformations,[37] in which the overall structure of the material remains unchanged when certain ions are replaced. The small size (1.33 Å)[38] and charge of the fluoride ions allow them to move easily through the crystal lattice even at low temperatures. This technique is especially effective when the starting structure has many anion vacancies already.[39] However, it is important to note that oxide ions are also somewhat mobile even at the temperatures ~200 °C used for fluorination, so there is no guarantee that fluoride will stay only in the vacant sites.[40,41] The low temperature of these reactions allows the synthesis of metastable oxyfluoride phases, and reduces the entropic driving force for anion disorder.[6,42,43]

1.1.3 Oxynitrides

Moving in the opposite direction on the periodic table relative to oxide, nitride substitution has the opposite set of effects as fluoride substitution, increasing covalency and oxidizing the cations. Many studies have shown the ability of nitride substitution to decrease the band gap of a metal oxide by up to 2 eV.[44-46] Since the *p*-orbitals of N are 2.8 eV higher in energy than those of O,[47] nitridation tends to raise the valence band maximum, making oxynitrides easier to dope *p*-type than oxides.[45] In the past decade, such tuning of the band gap through nitridation has been applied successfully to generate efficient perovskites for photocatalysis, which are able to absorb in the 2-3 eV range of the visible spectrum much more efficiently than oxides, while still having a large enough band gap (>1.3 eV) to drive the water splitting reaction.[48-54] The non-perovskite oxynitride photocatalyst ZnO:GaN has also proven capable of reducing CO_2, with a CO production rate up to 1.06 μmol g^{-1} h^{-1}, greater than paradigmatic TiO_2 photocatalysts.[55]

In nearly every case, oxynitrides with octahedral cations prefer a *cis*-coordination of identical ligands, as shown in Figure 1.1. This ordering is stable because it maximizes the covalent orbital overlap of the central cation with the nitride, which forms a stronger bond than oxide.[56-58] The energy difference between *cis* and *trans* anion order is typically about 100 meV/atom,[59] which is sufficient to maintain local ordering even up to high temperatures.[60] Exceptions to the *cis*-bonding preference are rare, and are most likely to occur in strained materials.[61,62] The long zig-zag chains of *cis* M-N-M bonds have several energetically degenerate choices of direction at each metal, so oxynitride perovskites rarely show complete segregation of O and N to different anion sites, even though the configurational entropy of such zig-zag chains scales as only $N^{2/3}$ where N is the crystal size.[56,63,64] This has generally prevented them from exhibiting classical ferroelectricity, but a few of them display relaxor-type behavior due to nanoscale polar domains arising from O/N ordering.[27,65] The anion ordering also plays an important role in photocatalysis, with a shift in band edge positions up to 0.5 eV calculated for different anion orderings of $CaTaO_2N$.[52]

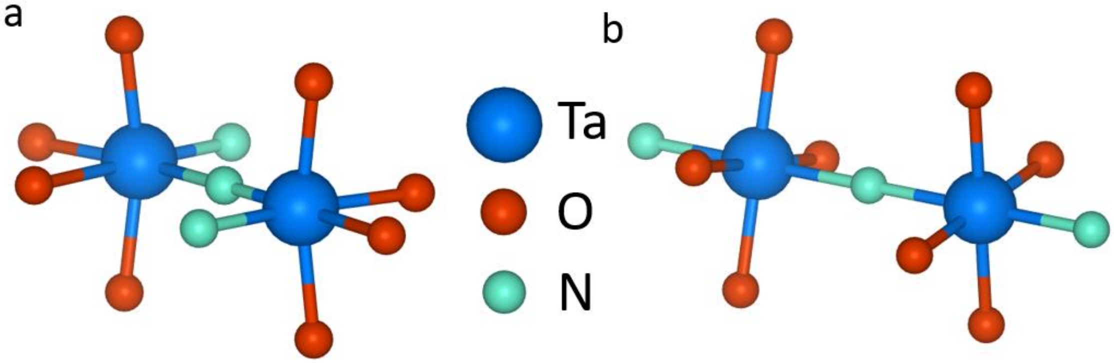

Figure 1.1 Anion-ordered oxynitride octahedra.

a. Two TaO_4N_2 octahedra with cis ordering of the N^{3-}, creating zig-zag chains of N – Ta – N bonds. b. The trans anion ordering.

1.1.4 Other Mixed-anion Ceramics

In addition to the oxyfluorides and oxynitrides, there are several other families of mixed-anion materials worth mentioning briefly. Nitride-fluorides are relatively rare, but their structures can be interesting due to the strong differences between metal-nitride and metal-fluoride bonds.[66] Many form “pseudo-oxide” structures in which F^- and N^{3-} substitute for O^{2-} in equal proportions and form a structure similar to the analogous oxide.[67] However, others possess a rigid nitride framework in which F^- plays the role of an interstitial defect,[68-71] and these materials may be valuable for electronic applications in the future, such as electrochromic materials[72] or superconductors,[73] if the fluoride content can be controlled precisely. The low stability of many nitride fluorides means that low-temperature synthesis techniques are essential for their further development.[74]

The last decade has also seen advances in the design and characterization of metal oxysulfides,[75-78] particularly for application as photovoltaics or photocatalysts. Addition of sulfide to an oxide plays a similar role to nitride, in terms of the modified properties, since sulfide is also less electronegative than oxide. However, S^{2-} has the same charge as O^{2-}, eliminating the redox chemistry of nitridation, and its 1.84 Å ionic radius does not always fit easily on the same site as oxide, which is only 1.4 Å.[38] This size mismatch plays an important role in driving anion ordering for the relatively small group of oxysulfides which have been studied in detail so far.[75,77,79] First-principles calculations of $BaZr_yTi_{1-y}O_2S$ compounds indicate that the preferred anion ordering is *trans*, rather than *cis* as in the oxynitrides, and the anion ordering can induce a large polar distortion of up to 88 $\mu C/cm^2$.[75] This materials system is of particular interest for the study of mixed-anion compounds because the *trans* ordering and the resulting distortions make the perovskite strongly tetragonal (c/a = 1.5), and the metal-sulfide-metal bonds are expected to point only out-of-plane if it is grown epitaxially on a cubic substrate, providing researchers with a very direct means of creating long-range anion ordering.

Despite its recent rise to prominence, anion engineering of functional ceramics has already proven to be a valuable tool for modifying important material properties. To achieve further progress, it is essential to gain a better understanding of the underlying physical principles. In the next section, I will take a closer look at some of the functionalities which we are hoping to tune using anion engineering.

1.2 Functional Ceramics

Modification of the anion sublattice is a powerful tool to incorporate useful functionalities and enable novel electronic devices, but its possibilities remain largely unexplored in most materials systems. For this thesis, I have applied anion engineering to four classes of ceramics, designing them for optimal performance using density functional theory (DFT). Each class of ceramics is tuned for one or more functions, which I will introduce in the following sub-sections.

1.2.1 Multiferroism

Ceramic materials are excellent platforms for the study of stable order parameters, such as ferroelectricity and magnetism. When multiple order parameters exist simultaneously in the same material, it is known as a multiferroic.[80] For example, a ferroelectric has internal electric dipoles which are ordered over long range to form domains, and the direction of the dipoles can be switched with an external electric field. Ferromagnets also form long-ranged domains, but the order parameter in this case is the spin alignment of unpaired electrons. Materials with more than one order parameter offer significant advantages for electronic devices, especially if the order parameters are coupled. Coupled order parameters can allow a stimulus of one type to produce a response of the other, such as by using an electric field to read and write a magnetic storage medium.[81]

One specific class of ceramics, the complex metal oxides, frequently exhibit one order parameter at a time. For example, $BaTiO_3$, $LiNbO_3$, and $PbTiO_3$ are all complex metal oxides with wide application as ferroelectrics.[82] Likewise, materials such as $La_{1-x}Sr_xMnO_3$ and Fe_3O_4 exhibit valuable magnetic properties, either ferromagnetism or antiferromagnetism. [83,84] But the two phenomena rarely occur together, since they both are likely to originate from the *d*-orbitals of transition metals. Classic ferroelectrics, such as $BaTiO_3$, are polar because the empty 3*d*-orbitals of Ti allow it to displace from the center of its octahedral coordination, breaking inversion symmetry and creating a large dipole.[85] However, this mechanism does not work in room-temperature magnetic oxides, which require unpaired electrons associated with transition metals. [86] Obtaining multiferroism in complex metal oxides requires a special design strategy, to avoid a conflict between the requirements of the different order parameters.

In Chapter 3 of this thesis, I illustrate the use of anion engineering to enable multiferroism in $AA'BO_5F$ transition metal oxyfluoride perovskites.[87] The mixing of O^{2-} and F^{-} provides control over the charge state of the transition metal (B = Fe, Mn), ensuring a strong magnetic ordering which pairs with the electric dipole to create a multiferroic. There are several possible variants of the perovskite structure, only one of which is electrically polar, and we establish that the size and charge difference of the A and A' cations determine the ground state of $AA'BO_5F$.

Finally, we predict that the new family of multiferroics will have high polarization up to 19 μC/cm^2 and robust antiferromagnetism above room temperature.

1.2.2 High-temperature Superconductivity

Most electrically conductive materials lose significant energy to resistance, but certain materials enter a superconducting state of zero resistance when cooled below a critical temperature T_C. The superconducting transport is enabled by the formation of Cooper pairs of travelling electrons, which cannot be scattered by defects or thermal phonons.[88] This behavior was first observed in liquid mercury at 4 K,[89] and subsequent research pushed the temperature up to 23 K in Nb_3Ge,[90] but the major breakthrough came with the introduction of cuprate superconductors, such as $YBa_2Cu_3O_{7-x}$ (YBCO), that have a T_C of 93 K, which is above the boiling point of liquid nitrogen.[91] Since their discovery, cuprate superconductors have been the subject of a Nobel Prize and hundreds of studies, but their properties are still not fully understood.

The cuprates are very complex systems, with the oxygen non-stoichiometry playing a fundamental role in the superconducting properties, such as T_C and the maximum current density J_C. YBCO has four inequivalent oxygen anion sites. Two of them are in the two-dimensional CuO_2 planes, which must have the correct amount of electron doping in order to maximize T_C and J_C, as shown in Figure 1.2.[92-94] This role is filled by the other oxygen sites, which sit in a "charge reservoir" of variable stoichiometry. Nearly all prior research has assumed that the oxygen vacancies occur only at the CuO chain site, since these vacancies, at higher concentrations, are readily detected by diffraction.[95] A handful of reports indicated vacancies also occurred at the fourth site, the apical position,[96-99] but no first-principles calculations have been done to study their stability or effect on superconductivity, and they have not been observed using direct methods.

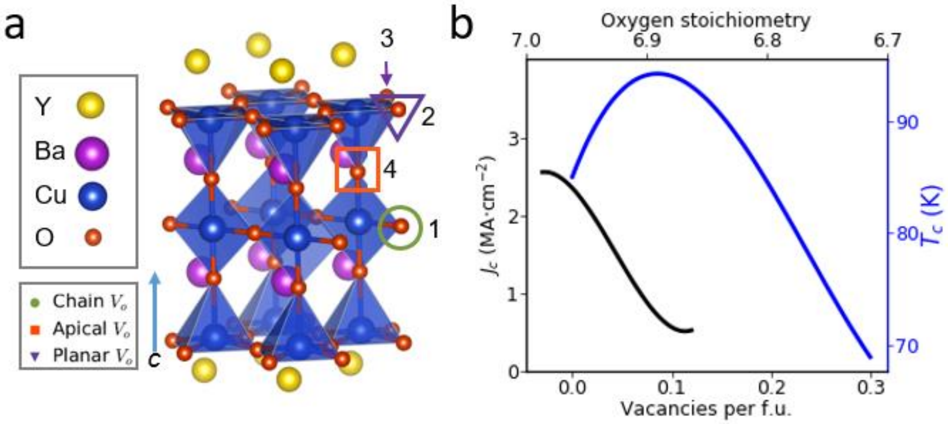

Figure 1.2 Effect of YBCO Oxygen Stoichiometry.

The structure of YBCO, with the four oxygen sites marked. b. The experimentally measured critical current density *J*c and superconducting transition temperature T_C in $YBa_2Cu_3O_{7-\delta}$, as a function of δ.

In Chapter 4 of this thesis, I present our joint theoretical and experimental study of apical oxygen vacancies in YBCO.[100] We find that apical oxygen vacancies are stable at low concentrations, and predict the crystal structure distortions which occur around a missing apical oxygen. These predictions are then confirmed by using scanning transmission electron microscopy (STEM) to image YBCO samples with optimal oxygen doping, revealing a crystal structure distortion which matches our predictions. We also show that the apical oxygen vacancy electron-dopes the adjacent superconducting CuO_2 plane, which is likely to influence T_C. Finally, we demonstrate that the apical vacancy can be selectively stabilized using uniaxial strains, such as those associated with certain stacking fault defects that are abundant in YBCO samples.

1.2.3 Polar Oxynitride Semiconductors

Many of the most valuable electronic devices rely on semiconductors. These materials have a moderate band gap, and their electronic conductivity can be tuned under an applied electric field or under thermal and optical excitations. The usefulness of a semiconductor depends on several factors, including the size of the band gap, the dielectric constant, the effective masses of charge carriers, and the properties of defects. In addition to their well-known application in transistors, semiconductors are vital for optoelectronics due to their ability to emit bright photons, and in solar energy harvesting wherein they can capture an incoming photon from solar radiation and convert it into free charge carriers. High-performance semiconductors such as amorphous Si and thin-film GaAs have powered the development of photovoltaics, while $In_xGa_{1-x}N$ has revolutionized the design of light-emitting diodes.

In the last decade, the lead-halide perovskites such as $CH_3NH_3PbI_3$ (MAPBI) have risen to prominence in optoelectronics and photovoltaics due to their combination of low cost and useful optical properties.[101] These lead-halide perovskites have excellent optical absorption and emission, and the excited electron-hole pairs are rarely lost to non-radiative recombination processes, even in thin, solution-processed films with many defects.[102,103] Their high performance can be traced to the electronic structure of lead-halides perovksites, which feature spatially delocalized *s* states of the Pb, with antibonding character, near the valence band maximum, greatly improving charge carrier mobility.[104] In addition, they have high dielectric constants, which screen charged defects effectively, and there is some evidence that they are also ferroelectric.[105] Electric polarity offers several advantages for optoelectronic semiconductors, most notably the ability to separate oppositely charged electrons and holes before they recombine,[106] and so semiconducting ferroelectrics have recently become the subject of intensive research.[107]

In spite of the useful properties of lead-halide perovskites, their potential for application is limited by the toxicity of lead and the materials' tendency to decompose when exposed to heat, light, and moisture.[108] From this perspective, it would be preferable to use oxide or nitride materials, which are much more stable.[104] Many oxides are ferroelectric, as discussed in section 1.2.1, but nearly all of the known ferroelectric oxides are insulators with band gaps greater than 2 eV,[109] which prevents them from absorbing the solar spectrum efficiently. Moreover, ferroelectric oxides have less mobile electrons — that are the majority charge carriers in oxides as opposed to holes — as their conduction band is composed of localized d-states. We can tune the band gap and conductivity of polar oxides by replacing some of the oxide anions with nitride, which forms much more covalent bond to metal cations, resulting in narrower gaps.[58] Simultaneously, we can improve the electronic conductivity by avoiding transition metal cations.

In Chapter 5, I describe our computational search for a stable oxynitride semiconductor with a cation from the *p*-block of the periodic table, to mimic the electronic structure of the lead-halide perovskites. We uncover a new family of $A\text{SnO}_2\text{N}$ ferroelectrics, in which the predicted band gap can be tuned from 1.6 to 3.3 eV by varying the *A*-site cation. Two new oxynitrides, YSnO_2N and EuSnO_2N, are stable against decomposition to competing phases, while the rest are likely to be synthesizable at low temperatures due to kinetic trapping.[110] The *s*-states of Sn at the conduction band edge lead to very good electron mobility, with electron effective masses as low as 0.12 times that of a free electron, comparable to successful electron conductors such as In_2O_3.[111]

1.2.4 Intercalation Battery Electrodes based on Fluorinated Electrides

A redox reaction requires an electron transfer between the reducing and oxidizing agents, but the two can be physically separated as long as electrons and charged ions can travel from one to the other, allowing the construction of batteries. In a battery, the two reactants are the electrodes, which act as a host for charged ionic species. During spontaneous operation, the half-reaction at the anode releases electrons, which travel to the cathode and reduce it in the other half-reaction, and the resulting Gibbs energy decrease provides a driving force for electrical work in the attached wires. Many batteries can also be recharged with an external potential that forces the reaction to proceed in the opposite direction. To maintain charge balance, the electron transport from cathode to the anode must be matched by an opposing ionic current, which completes the circuit.

Modern batteries can be broadly classified by their active ionic transport species. The dominant chemistry now is the Li-ion battery, which offers excellent energy density because Li is light (6.9 g/mol.) and its oxidation to Li^+ is very favorable with an appropriate cathode. The practical application of Li-ion batteries is also greatly aided by the small size (0.76 Å VI-coordinate) and charge of Li^+, which enable it to intercalate quickly and reversibly into empty atomic sites of the chosen electrodes, as shown in Figure 1.3. However, after decades of intensive development the performance of Li-ion batteries is approaching fundamental limits, and Li-ion batteries also require scarce material resources, such as Co.[112] Researchers are now turning to other ionic species; F^- shares many of Li^+'s advantages, but no intercalation electrodes have been found yet which can hope to match the performance of Li-ion electrodes, which have theoretical capacities > 200 mAh/g and voltages > 3 V.

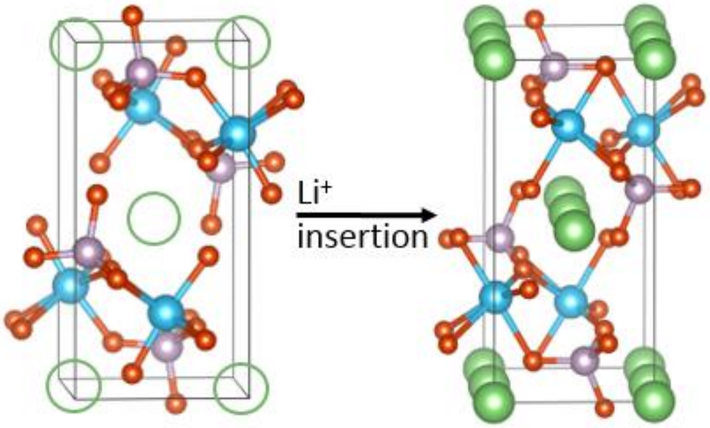

Figure 1.3 Intercalation of Li^+.
The charged (left) and discharged (right) states of a Li-ion intercalation cathode, in this case $LiFePO_4$.
The empty green circles mark the vacant lithium sites.

In Chapter 6 of this thesis, I show our search for high-performance F^- intercalation electrodes, that we predict to have good energy density, reaction speed, and long-term stability. Our first-principles calculations allow us to predict the voltage and current capacity of fluoride intercalation, even in materials which have never been used in batteries. We identify a promising class of layered electrides which have free electron density localized between sheets of atoms, providing good sites to host the intercalated fluoride ions. The calculated performance of the best electrode, Ca_2N/Ca_2NF, is almost as good as $CoO_2/LiCoO_2$.

Chapter 2: Rational Materials Design from First Principles

This chapter will review the fundamentals of our first-principles materials design strategy. The foundation is DFT, which we use to calculate the energy and electronic structure of a given crystal structure, providing the input for any further analysis. To compare two or more structures with each other, we need to understand the thermodynamic differences between the two, which can be encapsulated in a grand canonical model. Likewise, the energy cost for transition between two symmetry-related phases is found by calculating the energy along a transition path. This path can be expressed as a set of symmetrized distortions, written in the language of group theory.

2.1 Density-Functional Theory

DFT is the core of our materials design process since it allows us to calculate accurate energies for the crystal structures of different ceramics. The most immediate application of this capability is structural relaxation – moving atoms along the gradient of decreasing energy to find the ground state – but we can also compare the energies of multiple competing phases, to predict which will be the ground state structure. Here I will summarize the DFT calculation methods to accommodate a better understanding of the subsequent chapters.

The quantum-mechanical theory of the atom provides an accurate description of the electronic structure of atoms, which is expressed in a many-electron wavefunction, the time-dependent Schrödinger equation[113]:

$$i\hbar \frac{d}{dt}\left|\Psi(t)\right\rangle = \hat{H}\left|\Psi(t)\right\rangle \qquad [1]$$

where ħ is the Planck's constant 6.23 x 10^{-34} Joule-seconds , Ψ(t) is the electronic wavefunction, and *H* is the Hamiltonian of that wavefunction. For a stationary state of one particle, the specific form becomes:

$$\left[\frac{-\hbar^2}{2m}\nabla^2 + V(\boldsymbol{r})\right]\Psi(\boldsymbol{r}) = E\Psi(\boldsymbol{r}), \quad [2]$$

where *m* is the particle's mass, *V*(**r**) is the potential energy at position **r**, and *E* is the particle's total energy. The eigenvectors of this differential equation are the allowed electronic states, while the eigenvalues are the states' energies. The Schrödinger equation is exact, at least if Dirac's relativistic corrections are incorporated,[114] but it has *3N* variables where *N* is the number of interacting electrons. Therefore, an analytical solution is impossible for complex systems involving more than a few atoms.

DFT avoids this problem by replacing the many-electron wavefunction Ψ with a set of 1-electron wavefunctions, in which the electron of interest sees the other electrons simply as a charge density distribution. This is viable according to the Hohenberg-Kohn theorems; [115] the first demonstrates that the true electronic ground state is determined only by the electron density distribution, given by:

$$n(\mathbf{r}) = \sum_{i}^{N} \left|\psi_i(\mathbf{r})\right|^2, \quad [3]$$

where the ψ_i are the wavefunctions of the *N* electrons. The second theorem states that the ground-state density is the one that minimizes energy according to:

$$E[n] = \int v(\mathbf{r}) n(\mathbf{r}) d\mathbf{r} + \frac{1}{2} \int \int \frac{n(\mathbf{r}) n(\mathbf{r}')}{|\mathbf{r} - \mathbf{r}'|} d\mathbf{r} d\mathbf{r}' + G[n], \qquad [4]$$

where $v(\mathbf{r})$ is the external potential, n is the electron density, and G[n] is an unknown functional of the electron density. The exact form of G[n] remains unknown, but further work by Kohn and Sham showed that the missing many-body exchange and correlation effects contained in $G[n]$ could be approximated well, by treating the electron density as a homogeneous electron gas.[116] The exchange-correlation functional for the electron gas was subsequently calculated,[117] and the electrons' kinetic energy can be calculated by choosing any convenient eigenfunction of the Schrödinger equation, which generates the correct n(r) according to equation 3. The total energy of the i^{th} electron is then given by the differential equation:

$$\left[-\frac{\hbar^2}{2m} \nabla^2 + v(\mathbf{r}) + \int \frac{e^2 n_s(\mathbf{r}')}{|\mathbf{r} - \mathbf{r}'|} d\mathbf{r} + V_{XC}[n_s(\mathbf{r})] \right] \psi_i(\mathbf{r}) = E_i \psi_i \; [5]$$

where n_{s} is the total electron density of the system and V_{XC} is the exchange-correlation functional of choice.

V_{XC} must correct for a number of effects, most notably the unphysical interaction of an electron with itself in equation 5. Many different varieties of V_{XC} have been tried, to improve on the homogeneous electron gas approximation, with the two most popular classes being the Local Density Approximation (LDA)[116] and the Generalized Gradient Approximation (GGA);[118] GGA functionals also account for the first derivative of electron density at each point.[118]

In crystalline solids like those considered in this thesis, the electrons are best represented by a plane-wave expansion, as outlined by Bloch,[119] similar to the expansion of an arbitrary periodic function in a Fourier series. The form of the plane waves is

$$\psi(\boldsymbol{r}) = e^{i\mathbf{k}\bullet\mathbf{r}}u(\mathbf{r}) \qquad [6]$$

where **k** is a reciprocal-space wavevector, and $u(\mathbf{r})$ is a function with the same periodicity as the crystal lattice. Bloch's theorem states that an expansion of these Bloch waves forms a basis of eigenvectors for the Schrodinger equation,[119] with the eigenstates equal to the electronic energy; in practice, the expansion typically converges to an accurate energy with a manageable number of waves.[120,121] This convergence can be improved even further by modeling the core electrons of an atom using a pseudopotential, which reproduces the properties of the true potential but has smoother wavefunctions.[120]

The **k** in equation 6 has considerable physical significance, so we will look at it in slightly more detail. Instead of existing in isolated atomic orbitals, the electrons in periodic solids live in bands, which have the coordinates of energy and **k**. To describe the entire periodic crystal, it is sufficient to let **k** vary through the first Brillouin zone of the reciprocal lattice. The energy is evaluated at a set of special **k**-points, generally chosen as a uniformly spaced grid to minimize numerical errors. The symmetry of a crystal can be used to reduce the first Brillouin zone to an irreducible region; every point outside the irreducible first Brillouin zone is symmetrically equivalent to a point inside, so it is only necessary to calculate **k**-points inside the irreducible region. The simplest grid is that with its origin at (0,0,0) in reciprocal space, the gamma point, but Monkhorst and Pack demonstrated that the irreducible first Brillouin zone could often be sampled more efficiently by adding a constant shift to all the **k**-point positions.[122]

Once the special **k**-points are selected, the total energy is obtained by numerical averaging over the irreducible first Brillouin zone according to: [123]

$$\overline{f} = \frac{\Omega}{(2\pi)^3} \int_{BZ} f(\mathbf{k}) d^3\mathbf{k} \tag{7}$$

Here Ω is the Brillouin zone volume and *f*(**k**) is the energy at **k**. To integrate over the Brillouin zone, the zone is typically divided into tetrahedra with grid **k**-points at the vertices.[124] Because the grid points are evenly spaced, the tetrahedra have equal volume. Therefore, any operator $\langle X \rangle$ can be evaluated as:

$$\langle X \rangle = \sum_{j,n} X_n\left(\boldsymbol{k}_j\right) w_{n,j} \tag{8}$$

where $w_{n,j}$ is the weight of band *n* at **k**-point *j*. The weights are given by:

$$w_{nj} = \frac{1}{V_G} \int_{V_G} d^3\mathbf{k} w_j\left(\mathbf{k}\right) f\left(\varepsilon_n\left(\mathbf{k}\right)\right) \tag{9}$$

where V_G is the reciprocal unit cell, w_j is an individual **k**-point weight which equals one at the point, and goes linearly to zero at adjacent grid points, and *f* is the Fermi occupation function of band *n* at point **k**, which is a step function at zero temperature.

Since the energy of each band is a function of **k**, it can be very informative to plot the electronic band structure along a high-symmetry path through the Brillouin zone, as shown theoretically for In_2O_3 in Figure 2.1.[125] **k** has units of momentum, and it can be shown that the effective mass of electrons is inversely proportional to the curvature of the band in energy/momentum space.[126] Therefore, an electron excited to the bottom of the conduction band in Figure 2.1 ought to be very light, and indeed, experimental measurements of In_2O_3's electron effective mass are around 0.3 times the mass of a free electron,[127] giving excellent conductivity.

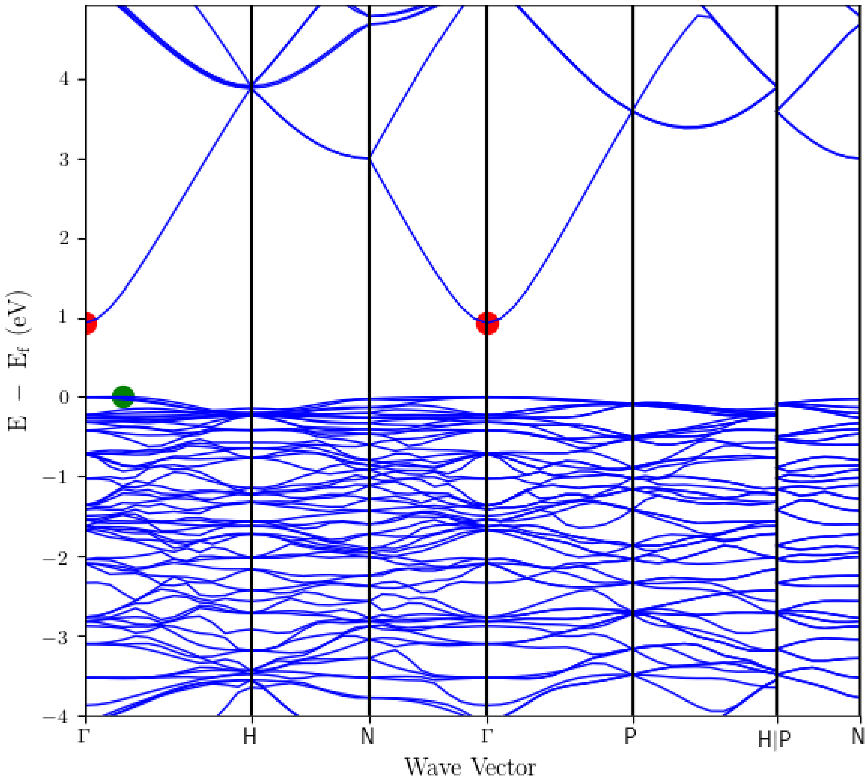

Figure 2.1 Electronic Band Structure of In_2O_3.
This calculated band structure from the Materials Project[125] was obtained with the PBE exchange-correlation functional.

It is important to remember that standard DFT methods almost always underestimate the band gap of materials, between the occupied and unoccupied bands. For example, the experimental band gap of In_2O_3 is 2.9 eV,[127] compared to the theoretical 0.9 eV calculated with the PBE exchange-correlation functional and displayed in Figure 2.1.[125] [118] Multiple factors contribute to this error. An incomplete cancelation of the electron's self-interaction by most exchange-correlation functionals plays a role, but more fundamentally, common functionals are differentiable for any number of electrons, while the (unknown) exact functional's derivative is discontinuous at integer electron counts.[128] Real excited states in many materials also feature electron-hole interactions and other effects which are not featured in a ground-state theory like DFT.[129]

There are many methods used to correct the band gap, but in this thesis we only employ two. The first is the addition of a Hubbard-like energy penalty function to certain atomic orbitals, which allows single occupation but penalizes double occupation.[130] This DFT + U method is especially effective for the *d*-states of transition metal compounds, which are highly localized and have a strong self-interaction error. While it is undesirable to have a tunable free parameter, a good choice of the U, and appropriate structural relaxations, can open up a realistic gap and spin polarization in metal oxides which would otherwise be nonmagnetic metals in DFT,[131] while the addition of U hardly increases computational cost. When calculating transition-metal-free compounds, we instead use hybrid functionals which take a weighted average of DFT and more expensive Hartree-Fock results; since Hartree-Fock overestimates band gap, hybrid functionals can give accurate gaps across a wide range of materials.[132]

2.2 Phase Stability

For any given chemical stoichiometry, there can be many stable crystal structures, which are referred to as polymorphs, but only one of them is the ground state under a specific set of conditions. To predict which phase or mixture of phases will be observed in experiments, we need to compare the energies of the different phases. While in principle we can account for temperature, pressure, electric field, etc., this thesis is mainly concerned with two effects: configurational entropy, and the chemical potential of any element whose amount is not fixed. Both effects can be incorporated using the formalism of a grand canonical model.

The grand canonical model considers a system of interacting particles, which is free to exchange both energy and atoms with external reservoirs.[133] There are many good overviews of the grand canonical model, so in this section I will look specifically at its application to DFT studies of phase stability,[134] building from simple cases to more complex. Consider first the transformation of β-Sn to α-Sn. A DFT calculation indicates that the α phase's energy/atom is -4.009 eV, while the β phase is -3.963 eV/atom.[125] There is a driving force for the β phase to change spontaneously to α, since the excess 0.046 eV/atom is released from the chemical bonds to the surrounding heat bath, raising its entropy.

However, there are several other effects to consider. To begin with, the calculated volume of the α phase is 36.7 Å^3/atom, while the β phase is only 28.4 Å^3/atom, so a Sn sample changing from β to α must do 8.17x10^{-7} eV/atom of expansion work. We see that we can neglect this term for solid state reactions at atmospheric pressure, but it can become relevant if one of the phases is a gas. Likewise, the two phases may have different entropy. Even if both crystals are perfect with no defects, they have different intrinsic vibrational entropies. This contribution is frequently ignored, because it is expensive to calculate, but it may be significant at high temperatures since the free energy reduction due to entropy is given by:

$$\frac{\delta G}{\delta S} = -T \qquad [10]$$

For example, a DFT study of $Cu_{0.5}Au_{0.5}$ alloy found that including vibrational entropy increased the driving force for mixing from –57 to –73 meV/atom at 800K.[135] Defects also make a large contribution to the free energy, and if defects are present, they have a configurational entropy of:

$$S = -Nk_B\left[\frac{N-1}{N}\ln\left(\frac{N-1}{N}\right)+\frac{1}{N}\ln\left(\frac{1}{N}\right)\right] \qquad [11]$$

where N is the number of possible atomic sites for each defect and k_B is Boltzmann's constant. This is illustrated in Chapter 4, where we calculate that oxygen vacancies in a complex metal oxide are stabilized by around 0.3 eV per vacancy when entropy is considered, with 5% vacancy concentration at 700K.

Finally, we moved beyond the closed system to consider the exchange of particles with an external reservoir. This is governed by the chemical potential, which is simply:

$$\mu = \frac{\delta G}{\delta N} \qquad [12]$$

and it measures the energy cost of "buying" or "selling" *N* particles from the reservoir. The system and reservoir are typically assumed to be in equilibrium, meaning that the chemical potential of a species is the same in both. For solid-state reactions, this μ is obtained by doing a DFT calculation of the reservoir phase and adding any necessary entropy corrections. For example, μ_{Li} for the lithiation of a battery cathode vs. a Li metal anode is simply the DFT energy/atom of Li metal; this is the energy cost of each Li that is imported from the anode, and the reaction is spontaneous, if the cathode's DFT energy decreases by more than μ_{Li} when a Li atom is added.[136] Thus the driving force per Li is:

$$V = \frac{CLi_{x+N} - CLi_{x} - N\mu_{Li}}{N} \qquad [13]$$

where CLi_x is the energy of the unlithiated cathode, and CLi_{x+N} is the energy of the same cathode with *N* Li added. This is how the grand canonical model enables first-principles calculations of battery voltage, as seen in Chapter 6.

The ability to handle the transfer of atoms or particles between phases is also essential for predicting whether a phase is stable, because a structure may still be unstable even if it is the lowest energy structure of a given chemical composition. A phase $A_xB_yC_z$ can undergo decomposition to form individual elements or binary compounds. If the energy per formula unit of each possible decomposition phase is known, the grand canonical linear programming approach shows which phase or combination of phases has the lowest energy.[137] $A_xB_yC_z$ is treated as the vector

$x\hat{\mathbf{A}} + y\hat{\mathbf{B}} + z\hat{\mathbf{C}} + \mathbf{E}_{ABC}$ in energy-composition space, and all other phases in the space are also vectors of lower dimension. The valid decomposition pathways are those whose products form a linear combination, with positive coefficients, equal to $x\hat{\mathbf{A}} + y\hat{\mathbf{B}} + z\hat{\mathbf{C}} + \mathbf{E}_{decomp}$. The convex hull of stable phases is a surface composed of the lowest- energy combination at each composition point, illustrated for the Ca-N phase diagram in Figure 2.2. A phase on this convex hull is stable, while phases above the hull ($E > E_{\mathrm{decomp}}$) will spontaneously decompose, although this decomposition may not happen quickly if the phases are separated by a large energy barrier.

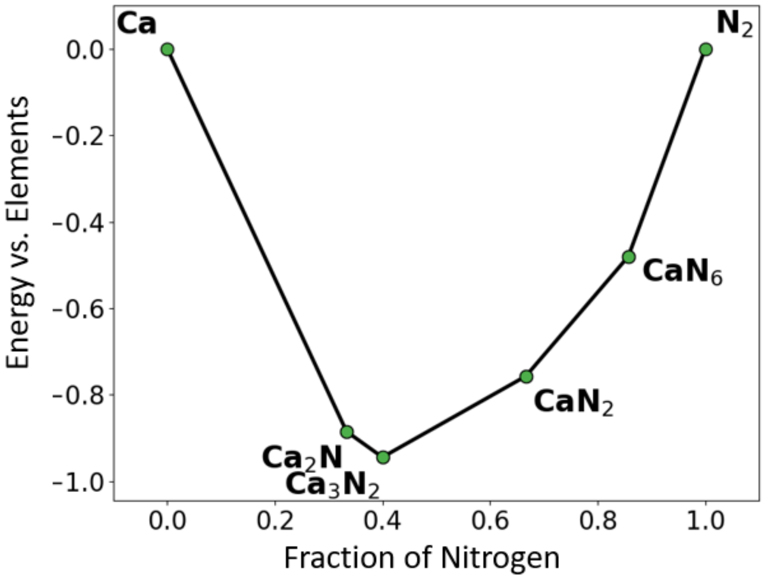

Figure 2**Error! No text of specified style in document.**.2 Calculated convex hull of Ca-N system.
This convex hull is calculated using the Materials Project data for phases in the Ca-N compositional space,[125,138] which has been projected into one compositional dimension by plotting the fraction of N.

2.3 Group Theory and Distortions

The thermodynamic phase stability discussed in 2.2 determines which phase(s) will predominate if the system has time to reach equilibrium. However, some systems experience large kinetic barriers that can trap them in non-equilibrium states for long timescales, so the experimentally observed state may not be the thermodynamic ground state. If two phases share common symmetrical properties, the dynamic transition between phases is best studied using the language of group theory, which classifies the crystal symmetry according to the symmetry operations which leave the structure unchanged. In addition to describing the symmetry of crystal structures, group theory also describes the phonon modes which connect phases of different symmetry, and is crucial to understand the switching process of ferroelectrics.

There are 230 possible space groups, each defined by a list of symmetry operators.[139] For example, space group #1 (*P*1 in the international notation) contains only the identity operator, which does nothing, so a *P*1 structure has no symmetry. By contrast, space group #2 (*P*–1) also has the inversion operator, designated x̄, ȳ, z̄. This means that for at least one choice of origin in a *P*–1 structure, position x, y, z is identical to –x, –y, –z for all x, y, and z, as illustrated in Figure 2.3. This origin site is known as an inversion center.

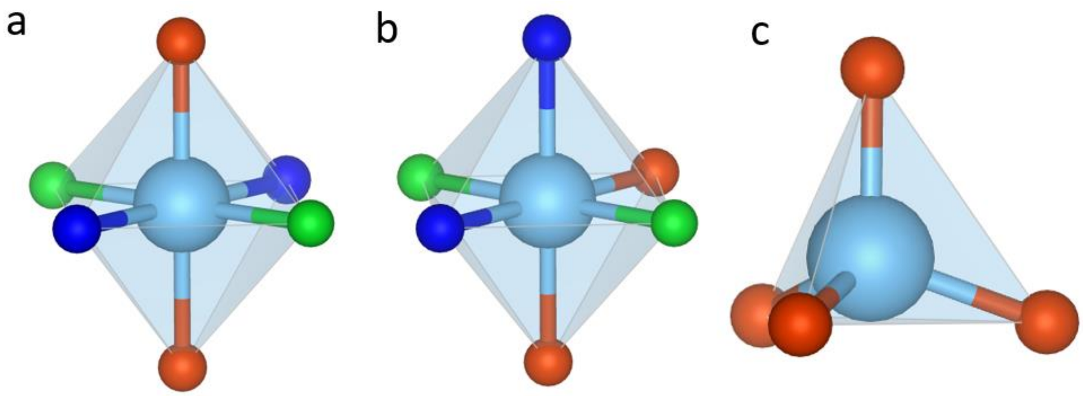

Figure 2.3 Inversion centers.
a. This octahedron has an inversion center on the central atom. b. Re-arranging the atoms breaks the inversion symmetry. c. This tetrahedron cannot have an inversion center on the central atom, regardless of the atoms' identities.

For this thesis, the most important category of symmetry transitions are the ferroelectric transitions, in which a structure has two or more degenerate non-centrosymmetric structures with different electric polarizations. These polarized states act as a "switch" which is sensitive to an external electric field or strain. For switching to be possible, the oppositely polarized states should be connected by a centrosymmetric structure of slightly higher energy; $Ca_3Ti_2O_7$ has a calculated barrier of 6 meV/atom,[140] and barriers on the order of 10 meV/atom are quite typical for other oxides like $BaTiO_3$.[125] If the barrier is too high, the material cannot be switched and is pyroelectric instead of ferroelectric.

In many cases, the non-centrosymmetric phase is known experimentally, while the centrosymmetric phase is not observed, at least at room temperature. This raises the question of how to identify a ferroelectric transition when only one of the two structures is known. For this situation, we take advantage of the group-subgroup relations between the phases. The centrosymmetric phase's space group must be a supergroup of the non-centrosymmetric group, meaning that it contains every symmetry operator of the subgroup, plus additional operators including inversion. Because of this requirement, the number of centrosymmetric structures is greatly limited. In this thesis, we use the PSEUDO program to take a polar structure and search for small distortions, which increase the structure's symmetry to a centrosymmetric supergroup.[141]

We illustrate these concepts using an example taken from Chapter 5, the ferroelectricity of $YSnO_2N$, in Figure 2.4. Having identified the polar $P6_3cm$ structure from a high-throughput DFT search, we then use PSEUDO to obtain the structure with centrosymmetric supergroup $P6_3/mmc$. The distortion connecting the two structures can be expressed as a phonon mode, which in this case is a concerted tilting of the polyhedra and motion of the Y^{3+} cations. When we calculate the phonon frequencies of the two structures, we see that the centrosymmetric structure has negative frequencies, indicating that the ferroelectric transition mode is unstable. The polar structure has no negative phonon frequencies because it is a local minimum of energy, and there is a spring-like restoring force resisting any distortion. By interpolating image structures between the two endpoints, we obtain the double-well energy plot with a switching barrier height of 31 meV/atom. We also use these images to calculate the polarization according to the modern theory,[142,143] and find that it is 11.5 $\mu C/cm^2$.

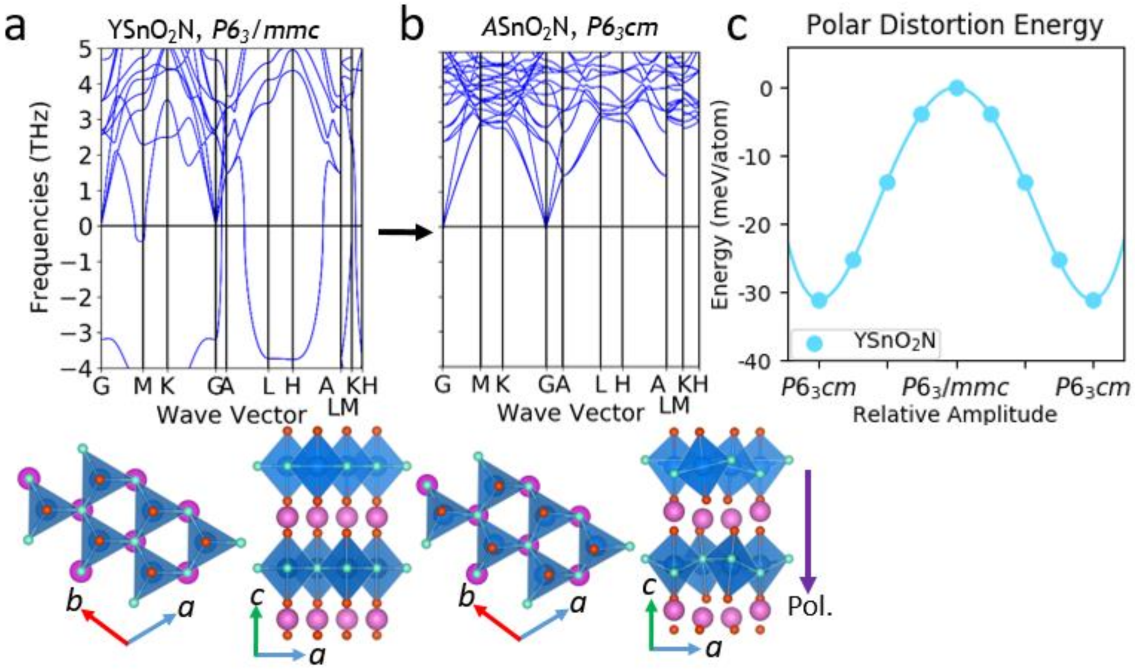

Figure 2.4 Ferroelectric transition in $YSnO_2N$.

a. The centrosymmetric *P6$_3$/mmc* structure and its unstable negative phonon frequencies. b. The stable *P6$_3$cm* polar structure, with its stable positive phonon frequencies. c. The energy along the pathway connecting the structures, showing the double-well potential of a ferroelectric.

Chapter 3: Multiferroism in Iron and Manganese Oxyfluoride Perovskites

The material on iron oxyfluorides has been published in as S. T. Hartman, S. B. Cho, and R. Mishra "Multiferroism in Iron-based Oxyfluoride Perovskites" *Inorganic Chemistry* 57(17) 10616-10624 (2018).[87] S. B. Cho contributed to this work by calculating the stability of alternate structural polymorphs not discussed here, and by testing different approaches for converging some of the calculations.

3.1 Abstract

Multiferroic materials with simultaneous magnetic and ferroelectric ordering that persist above room temperature are rare. Recent studies have demonstrated that double perovskites with the formula $AA'B_2O_6$ (where A, A' and B are cations) can achieve both the orderings if the A,A' cations have a layered ordering. However, if Fe^{3+} is used at the B-site to sustain magnetic ordering at higher temperatures, charge neutrality requires that A and A' are both +3 ions, and their polar displacements nearly cancel each other. We use first-principles calculations to study fluorination to $AA'Fe_2O_5F$ as a means to lift this restriction. We find that the polarization of the non-centrosymmetric $a^-a^-c^+$ phase with space group $Pmc2_1$ can be as high as 19.3 μC/cm^2, and that the stable ground state of the perovskite depends on the sizes and size difference of the A-site cations. In addition, we show that the superexchange interactions in these materials are strong enough to sustain magnetic order well above room temperature. Replacement of Fe with Mn

stabilizes the polar phase across a wider variety of *A*-site cations, due to the Jahn-Teller activity of Mn^{3+}.

3.2 Introduction

While ferroelectricity and magnetic are each common in perovskites, there are very few perovskites which possess both properties at the same time, especially above room temperature. This incompatibility is due to the conflicting restraints which the two types of ordering place on the *B*-site cation. Magnetism usually originates due to transition-metal cations with partially filled *d*-orbitals, while the conventional ferroelectric mechanism, seen in perovskites such as $BaTiO_3$, requires *B*-site cations with empty *d*-orbitals.[86] This constraint can be lifted to achieve multiferroism by selecting two different cations, one for each task. For instance, in $EuTiO_3$, magnetism arises due to the unpaired *f*-electrons of Eu, while the $3d^0$ Ti cation undergoes polar distortion.[144] In $BiFeO_3$, polarization arises due to the steric hindrance of the $6s^2$ lone-pair electrons of Bi,[145] while the $3d^5$ electrons of Fe^{3+} undergo magnetic ordering. In the family of hybrid improper ferroelectrics, the layered ordering of two cations at the *A*-site, when coupled with the correct combination of octahedral tilts, results in a finite polarization.[146-149] This is because the tilts lead to displacement of *A*-site cations along opposite directions in successive layers, but if the two *A*-site cations do not have identical size or charge, the resulting dipoles do not cancel completely, leaving a net polarization, as shown in Figure 3.1. This polarization can, in principle, be switched by changing the direction of octahedral tilting.[150,151] Since the ferroelectricity in this case results from the *A*-site cations, the *B*-site cations can have magnetic moments due to occupied *d*-orbitals.

With the *B*-site reserved for magnetism, which cation is best? Antiferromagnets are promising for multiferroics, since they can have very high Néel ordering temperature if there is a strong superexchange interaction between the *B*-site cations, operating through the *B*-*X*-*B* bonds. Fe^{3+} meets this criterion very well,[15,152] with $LaFeO_3$ showing an antiferromagnetic Néel temperature of 750 K compared to 100 K for $LaMnO_3$ or 320 K for $LaCrO_3$.[153] For this reason, $AA'Fe_2O_6$ is a promising family of potential multiferroics, while multiferroics with other *B*-site cations rarely have room temperature magnetic ordering. However, this robust magnetism comes at a price. Charge balance in an Fe^{3+} double perovskite oxide requires that the oxidation states of the two *A*-site cations sum to +6, and since small +4 cations rarely occupy the *A*-site, in practice these hybrid improper ferroelectrics must have two +3 *A*-site cations such as lanthanides.[154-156] The net polarization in this case results only from the size difference between the two lanthanides, and the two ionic displacements cancel to a large extent. It would be preferable to use a larger +2 cation at one of the *A* sites to maximize the polarization[157] and improve the precision of cation layer ordering.[155] But if the total cation charge is altered in this way, charge balance then leads to oxygen-deficient structures to avoid the formation of the less favorable Fe^{4+} oxidation state.[158-162] Furthermore, the oxygen vacancies in such perovskites are often observed to undergo ordering along specific planes, which results in the breaking of the cooperative octahedral tilt pattern necessary for the hybrid improper ferroelectric mechanism. Substitution of fluoride with −1 charge, compared to oxide's −2, lifts this constraint and permits the *A*-site charge to take values other than +3. Therefore, fluorination of oxide perovskites offers the chance to optimize the ferroelectricity with minimal effect on the magnetism.

3.3 Computational Methods

We studied $AA'Fe_2O_5F$ perovskites using the plane wave DFT code Vienna Ab initio Simulation Package (VASP)[163] version 5.4 with the projector augmented-wave (PAW) method. We used the PBEsol exchange-correlation functional,[164] which has been found to be optimal for perovskite oxyfluorides.[165] Additionally, to describe the strong correlations arising from the localized *d*-electrons of Fe, we used a Hubbard *U* parameter of 4 eV using the method of Dudarev et al.[130] In agreement with a previous work,[166] we found that this value accurately reproduced the charge and magnetic ordering of a possible unfluorinated starting compound, $YBaFe_2O_5$.[167] While this parameter is empirical and against the first-principles nature of DFT, it is necessary to describe transition metal *d*-states accurately. *G*-type antiferromagnetism, in which each Fe has a spin opposite to all its nearest neighbors, was imposed on each system unless stated otherwise. We also imposed layered ordering of the *A*, *A′* cations along the *c*-axis in all the compounds investigated in this work. To find the likely ground states of this perovskite family, we studied $YBaFe_2O_5F$ and $LaCaFe_2O_5F$ because they represent two extremes of the size difference at the *A*-site. For these two systems, we relaxed them in many different combinations of octahedral tilt patterns and O/F anion orderings to find the ground state. The polar state with its preferred anion ordering is shown in Figure 3.1c. To reduce the computational cost, the remaining 10 systems with *A*-site pairs: LaBa, YBa, LaSr, LuSr, YSr, EuCa, YCa, YbCa, LuCa, and InCa, were only relaxed in the few most stable configurations observed in the two prototypes. We then used $YCaFe_2O_5F$ as a model system for the calculation of ferroelectric and magnetic properties because it has a stable polar ground state.

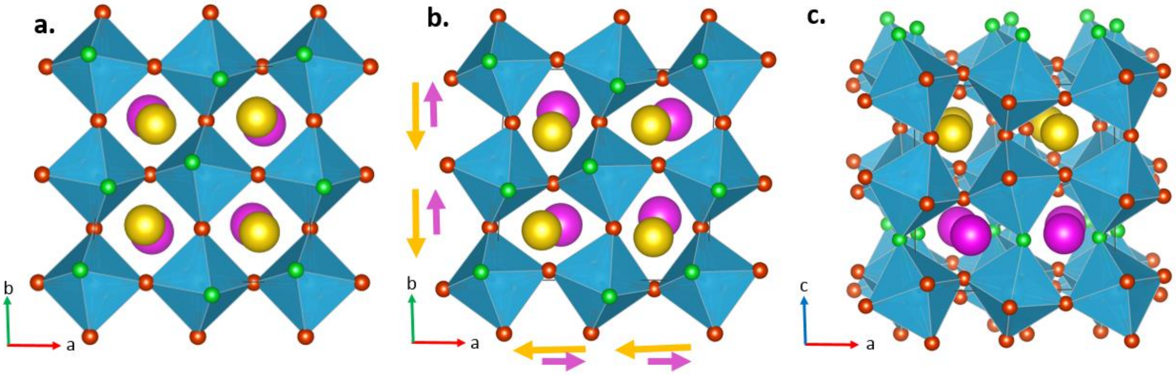

Figure 3.1 Crystal structures of $YCaFe_2O_5F$ with various tilt patterns.
(a.) Centrosymmetric phase having *Pmma* symmetry with $a^-a^-c^0$ tilts. (b.) A polar phase with $Pmc2_1$ symmetry is obtained from (a.) by adding in-phase octahedral rotations about the *c*-axis (c^+), coupled with non-compensating displacements of *A*-site cations, Y (yellow) and Ca (pink) here, in alternate layers. As indicated by arrows, Y atoms displace toward the left or bottom of the figure, while Ca atoms displace toward the right or top. (c.) Structure of the polar phase as viewed along the b-axis, showing the antiphase a^-a^- tilts. We find that the polar phase is most stable with F (green) in the layer of Ca^{2+} cations. Oxygen atoms are shown in red and FeO_5F octahedra are shown in blue color.

3.4 Results

We begin by briefly discussing the effect of fluorination of $YCaFeO_5$ on its electronic structure. Although $YCaFe_2O_5$ has not been synthesized, we can model it as a mixed-valence Fe^{2+}/Fe^{3+} structure with ordered oxygen vacancies in the Y layer, which has been observed for many $RBaM_2O_{6-x}$ compounds such as $YBaFe_2O_5$ and $YBaMn_2O_5$.[160,168,169] There are several possible combinations of magnetic and charge ordering; here, we have chosen to impose the $YBaMn_2O_5$ type. The low temperature phase of $YBaMn_2O_5$ shows G-type antiferromagnetism, which when combined with the "checkerboard" charge ordering produces an overall ferrimagnetic state because Mn^{4+} has a smaller magnetic moment than Mn^{3+}. It is possible that $YCaFe_2O_5$ could have striped charge ordering instead, in which case the unit cell size would double and the compound would have zero net magnetic moment. Fluorination of $YCaFe_2O_5$ is an oxidative process if the fluorine does not displace any of the oxygen, so the Fe^{2+} cations with d^6 configuration are oxidized to Fe^{3+} state with d^5 configuration. We observe this effect in the density of states (DOS) shown in Figure 3.2, where the occupied Fe^{2+} *d*-states present near the Fermi level in $YCaFe_2O_5$ (the solid filled states in Fig 2b.) are absent in the fluorinated compound (Fig. 2d). We also observe that fluorination of $YCaFe_2O_5$ increases the band gap.

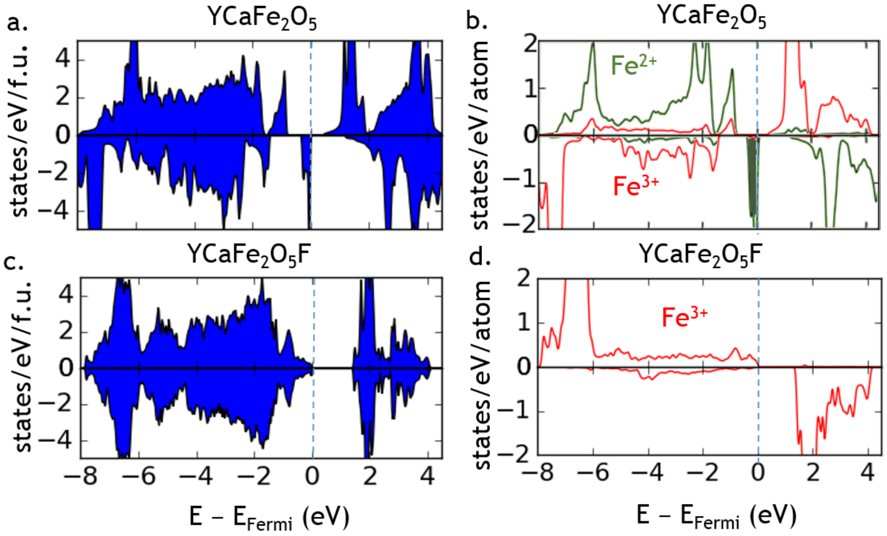

Figure 3.2 Electronic structure of $YCaFe_2O_5$ and $YCaFe_2O_5F$.
(a.) The electronic density of states (DOS) of unfluorinated $YCaFe_2O_5$, (b.) DOS projected onto the Fe *d*-states for both Fe^{2+} and Fe^{3+} oxidation states in $YCaFe_2O_5$. (c.) and (d.) show the same data for the ground state of $YCaFe_2O_5F$ with Ca-layer fluorination in the $a^-a^-c^+$ tilt pattern. Fluorination leads to oxidation of Fe^{2+} ions to Fe^{3+}.

We will now examine the magnetic properties of $YCaFeO_5F$ and its likelihood of remaining magnetically ordered at room temperature. Based on the Goodenough-Kanamori rules for superexchange,[16,170] this compound is expected to be an antiferromagnet due to the presence of antiferromagnetic interactions between neighboring Fe^{3+} cations. Our calculations confirm that *G*-type antiferromagnetism is more stable than *A*- and *C*-type antiferromagnetism, as well as the ferromagnetic state. The calculated magnetic moments on Fe^{3+} are 4.0-4.1 μ_B, less than the theoretical value of 5 μ_B, but it is important to note that the calculated value comes from integration across a somewhat arbitrary atomic sphere, while the theoretical value assumes that Fe^{3+} has exactly 5 *d*-electrons which corresponds to purely ionic bonding.[171] To estimate the Néel temperature (T_N) for transition from antiferromagnetic to paramagnetic ordering, it is necessary to determine the strength of the individual superexchange interactions acting through the Fe–O–Fe or Fe–F–Fe bond pathways. We considered magnetic interactions up to the third nearest-neighbors and extracted the interactions $J_1 - J_9$ by fitting a Heisenberg model to the total energy of 10 different magnetic configurations that were chosen randomly, subject to the constraint that the resulting set of equations were linearly independent. The Hamiltonian is given by

$$H = E_0 - \sum_{i \neq j} J_{ij} S_i S_j \ , \quad [14]$$

where $S = 5/2$ is the theoretical spin of the Fe^{3+} ion. We found the exchange constants for $YCaFe_2O_5F$ with the ground state $a^-a^-c^+$ tilting and Ca-layer fluorination. We made the approximation that structure is the same along *a* and *b* directions, since it has $a = 7.635$ Å and $b = 7.607$ Å, but we considered two different types of in-plane nearest-neighbors interactions, J_3 and J_4, as shown in Figure 3.3. There are two types of in-plane bonds due to the broken mirror symmetry from cation ordering: interaction J_3 with an Fe–Fe distance of 3.71 Å and an Fe-O-F bond angle of 143^0; and J_4 with an Fe-Fe distance of 3.93 Å and a bond angle of 151^0.

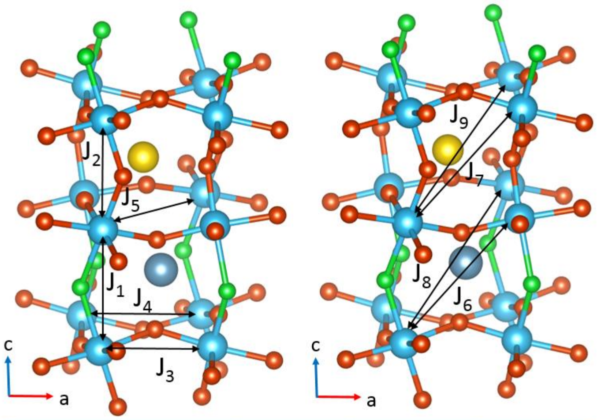

E$_0$/f.u.	J_1	J_2	J_3	J_4
-75.10 eV	-1.4 meV	-8.4 meV	-9.4 meV	-5.9 meV
J_5	J_6	J_7	J_8	J_9
-0.43 meV	0.16 meV	0.07 meV	-0.27 meV	-0.38 meV

Figure 3.3 Magnetic exchange constants between Fe3+ ions in $YCaFe_2O_5F$.
A positive sign indicates a ferromagnetic interaction. The atomic model on the left shows the nearest-neighbor interactions, which are stronger than the 2nd and 3rd nearest-neighbor interactions shown on the right. The size of the *A*-site cations has been reduced for clarity.

Based on the calculated strengths of various exchange interactions, as shown in Figure 3.3, we find that the nearest-neighbor interactions $J_1 – J_4$ are dominant, with strong antiferromagnetism leading to the *G*-type AFM ground state. The total magnetic stabilization of each Fe ion with respect to the magnetically disordered state is given by[166]

$$\frac{1}{2}\sum_i J_i z_i \left(\frac{5}{2}\right)^2 = -136\ \text{meV} \quad [15]$$

where z_i is the number of interactions of each type that the ion has. If only the nearest-neighbor interactions $J_1 – J_4$ are taken into account, this value becomes −125 meV/Fe. While T_N could in principle be calculated from the exchange constants using a mean-field approximation or with Monte Carlo simulations, in practice this may give inaccurate results due to the empirical nature of the Hubbard U parameter.[154,172] Instead we have compared the magnetic stabilization for $YCaFe_2O_5F$ with those calculated using the same DFT parameters for related compounds whose T_N are known experimentally. For $YFeO_3$, with T_N = 655 K,[173] we calculate an energy stabilization in G-type AFM of −106 meV/Fe, including only nearest-neighbor interactions. For $YBaFe_2O_5$, with a slightly different structure and T_N = 410 K,[167] the calculated stabilization of G-type AFM is −115 meV/Fe including up to second-nearest-neighbor interactions, which is similar to a previous report.[166] Therefore, we expect that the strong exchange interactions in $YCaFe_2O_5F$ will lead to a robust magnetic ordering with a Neél temperature at least as high as 410 K. We note that the Fe-F-Fe exchange constant J_1 is only −1.4 meV, much smaller than the Fe-O-Fe interactions $J_{2\text{-}4}$. The reason for this is the decreased covalency of the bond through F, which has much lower valence orbital energies than O.

To confirm if $YCaFe_2O_5F$ is a hybrid improper ferroelectric, we have calculated the polarization of its ground-state phase with F atoms in the Ca layer, having a $Pmc2_1$ space group and $a^-a^-c^+$ tilts, using the Berry-phase method.[142,143] We find that $YCaFe_2O_5F$ has a spontaneous polarization of 10.3 μC/cm^2. The expected switching mode is a reversal of the c^+ tilt, moving through a *Pmma* centrosymmetric phase with a calculated energy barrier of 64 meV/f.u. The switching barrier of a useful ferroelectric should be large enough to be stable against thermal fluctuations, but low enough that a reasonable coercive field can overcome it. It is not possible to calculate the ferroelectric/paraelectric transition temperature or required coercive field directly from the height of the theoretical switching barrier, since the actual switching mechanism may involve domain wall motion rather than a concerted motion of all the atoms as we have calculated here.[174] However, the calculated barrier of 64 meV/f.u. is exactly the same as that of the

Ruddlesden-Popper phase $Ca_3Ti_2O_7$,[174] which has a different switching mechanism but is known to be experimentally switchable.[151]

To investigate the presence of any magnetoelectric coupling, we have calculated the exchange interactions along the distortion mode that switches the polarization. We find that switching the polarization also affects the magnetic exchange constants, since the switching pathway temporarily eliminates the c^+ octahedral rotations. This improves the overlap of Fe *d*-states with the *p*-states of O/F and increases the strength of the superexchange interactions. As we have established that longer-ranged interactions are relatively unimportant in this system, for clarity, we have used a simplified Heisenberg model with only a single nearest-neighbor interaction (J_{NN}), as shown in Figure 3.4. We find that the centrosymmetric *Pmma* phase shows increased superexchange between nearest neighbors with the average nearest-neighbor exchange constant being −8.18 meV compared to −7.17 eV in the ground state. The ground state $Pmc2_1$ phase is also expected to show a linear magnetoelectric coupling through the Dzyaloshinskii-Moriya effect because there is no inversion center between the neighboring iron atoms.[154] Therefore, the magnetic moments are expected to be canted and to respond to the switching mode. However, quantifying the strength of this coupling would require expensive non-collinear magnetism calculations, which are outside the scope of this article.

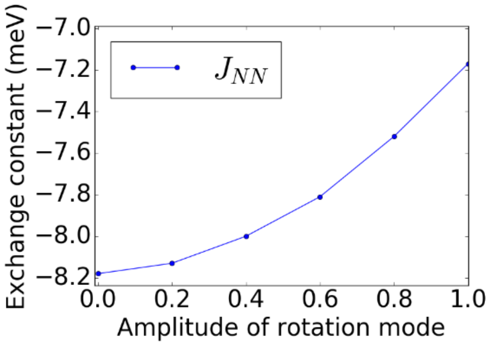

Figure 3.3 Variation of the nearest-neighbor (NN) exchange constant J_{NN}
The amplitude of the polarity-switching mode combines opposite polar displacements of successive *A*-site layers and the reversal of the c^+ octahedral tilt.

The polarization predicted (10.3 μC/cm^2) for $YCaFe_2O_5F$ is not unusually large. For comparison, $LuLaFe_2O_6$ with exclusively +3 cations at the *A*-site was predicted to have a polarization of 11.6 μC/cm^2.[154] While the introduction of the Ca^{2+} tends to reduce the cancellation of the opposing *A*-site displacements, the size difference between Y^{3+} and Ca^{2+} is only 0.1 Å according to their 8-coordinate Shannon radii.[175] Hence, in the following, we have investigated the possibility to achieve higher polarization by changing the size-ratio of the two *A*-site cations, but keeping their charge ratio fixed at +2/+3.

The substitution of different cations at the *A*-site is expected to have a strong influence on the octahedral tilt pattern, since the main purpose of these tilts is to optimize the coordination environment of the *A*-site cation.[176] Specifically, a smaller *A*-site cation causes increased tilting, and tends to favor the $a^-a^-c^+$ tilt pattern, which mitigates the anion-anion repulsion around the small cation.[176] We considered Ba, Sr, and Ca for the 2+ cation and chose the 3+ cation from La, Y, Eu, Lu, Yb, and In. For each pair of *A*-site cations, we show the calculated polarization in Figure 3.5. Compounds having the polar phase ($a^-a^-c^+$, $Pmc2_1$) as the ground state are shown in blue and those having a non-polar phase, such as $a^0b^-c^-$, as the ground state are shown in red. We find that compounds having small 2+ cations, such as Ca, are more likely to prefer the polar phase, which is consistent with the expectation that small *A*-site cations favor $a^-a^-c^+$ tilt pattern. However, other factors such as size difference also play a role. CaIn and SrLu have average *A*-site cations sizes less than or equal to those of stable polar compounds, but their calculated ground state has $a^0b^-c^-$ tilt pattern and fluorine in the Fe layers of the compound. Two of the compounds, EuCa and LaCa, are listed as having zero polarization even though they are both non-centrosymmetric. In these compounds, the small ionic polarization is screened almost completely by an opposing electronic polarization. We find that the polarization generally increases with increasing size difference, as predicted by previous first-principles calculations on oxide hybrid improper ferroelectrics.[157,177]

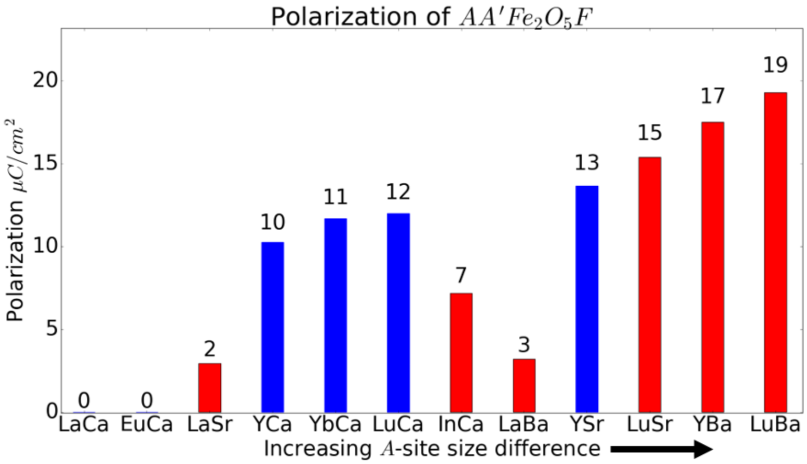

Figure 3.4 The calculated polarization of $AA'Fe_2O_5F$ double perovskites with varying size difference of the *A* and *A'* cations.

The polarization has been calculated in the non-polar $Pmc2_1$ space group with $a^-a^-c^+$ tilt and F in the layer of the +2 cations. Blue bars indicate that the system prefers this polar phase, while red bars indicate that there is a competing non-polar phase that is more stable.

Finally, we have considered whether it is likely that these fluorinated multiferroics can be synthesized. The data in Figure 3.5 indicate that a small *A*-site size difference is required to achieve the $a^-a^-c^+$ tilt pattern. However, this small size difference when combined with the small charge difference of +2 and +3 cations makes it unlikely that the compounds will spontaneously order into alternating layers at the *A*-site, as required by the hybrid improper mechanism. To test this possibility, we have calculated the energy of a cation-disordered special quasirandom structure (SQS)[178,179] of $YCaFeO_6$ in the $a^-b^+c^-$ tilt pattern, which the untilted structure spontaneously adopted during relaxation. We find that the ordered and disordered structures have the same energy to within 1 meV/f.u., with entropy likely to produce disorder at experimental temperatures. Therefore, we expect that it will be necessary to use layer-by-layer growth techniques to impose layered *A*-site cation ordering artificially.

We have also considered the possibility of decomposition to competing binary and ternary phases. Similar oxyfluoride perovskites are often metastable,[6] due to the high stability of the binary fluorides which would result from decomposition. We can calculate the stability of a compound by comparing its energy with respect to its most stable reactants or products. Compounds that cannot decompose into more stable products lie on the convex hull of the phase diagram, while those that can, are above the hull. Previous data-mining of the calculated formation energies of known compounds has shown that the 90th percentile of metastable compounds are 67 meV/atom above the convex hull.[110] Hence, we can use a formation energy of < 70 meV/atom as a criterion to evaluate metastable compounds that can be synthesized. We have used the Open Quantum Materials Database[180] to identify the most favorable decomposition pathway for six of our compounds, then calculated the formation energy relative to the convex hull. For this calculation, we found the energy of the decomposition products using the same DFT settings we previously used for the oxyfluorides. As an example, $YCaFe_2O_5F$ is most susceptible to decompose by the reaction

$$YCaFe_2O_5F \text{ -> } YFeO_3 + 0.5(CaFe_2O_4) + 0.5(CaF_2)$$

and the change in energy of this process is -41.7 meV/atom, placing $YCaFe_2O_5F$ 41.7 meV/atom above the convex hull but within the region where metastable compounds are plausible. The formation energies vs. the convex hull of 6 representative compounds are shown in Figure 3.6a.

Synthesis of metastable compounds usually occurs when the compound is kinetically trapped and cannot transform to more stable phases. In perovskites, cations are not mobile at low temperatures, but anions are, which is the basis for the ‘soft chemistry’ topochemical techniques which modify the anion sublattice of a stable oxide but leave the rest of the structure unchanged.[6,37,181] Because the cations are not mobile, they cannot phase segregate to low-energy binary or ternary compounds once fluorine is added.[182] It is interesting to note that $LaSrFe_2O_5F$, which we predict to be metastable based on the formation energy (32 meV/atom), has been synthesized with cation disorder at the *A*-site using low-temperature fluorination.[42] Centrosymmetric $La_{2-x}Sr_xFe_2O_{6-x}F_x$ was obtained across the wide composition range $x = 0$ to $x = 2$, using fluorine like a co-dopant to maintain charge balance.[42,183] As expected, the compound was metastable but could be made as a single phase at relatively a low temperature (400 ^{0}C). Therefore, we expect that similar low-temperature fluorination techniques combined with layered *A*-site ordering can be used to produce many of the compounds considered here.

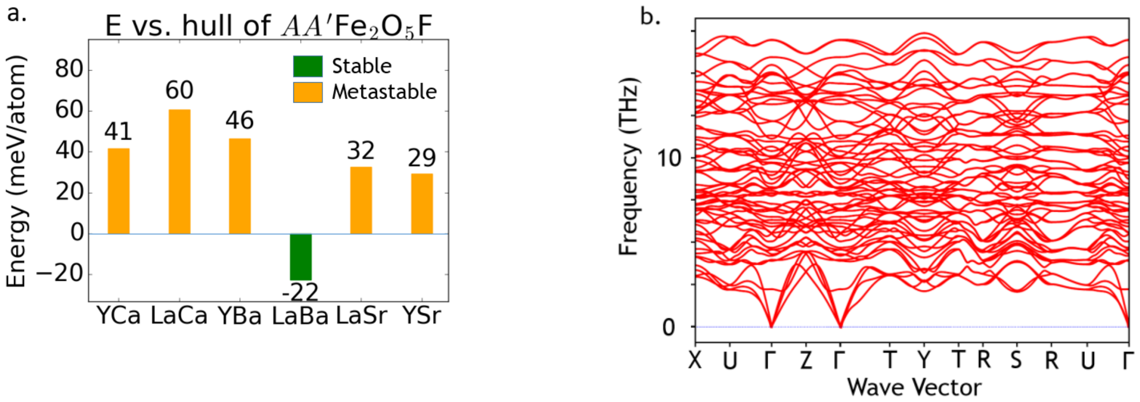

Figure 3.5 Thermodynamic and dynamic stability of polar $AA'Fe_2O_5F$ multiferroics.
(a.) The calculated formation energies of 6 representative compounds, including YCa. A negative energy corresponds to a stable compound that lies on the convex hull. (b.) Phonon band structure of the polar ground state of $YCaFe_2O_5F$, which has no soft phonon modes and is therefore dynamically stable.

For ease of synthesis, it is desirable to produce materials in bulk rather than in thin films. Is it possible to obtain transition metal oxyfluoride multiferroics in bulk, with a polar ground state? We have also studied the use of Mn instead of Fe at the *B*-site. Mn^{3+} has a d^4 electronic state which has 1 electron present in 2 degenerate states, making it susceptible to a Jahn-Teller (J-T) octahedral distortion which lengthens some of the bonds and shortens others. This is likely to influence the preferred octahedral tilt pattern, so for $AA'Mn_2O_5F$ (AA' = LuSr, LuBa, YCa, YSr, YBa) we have searched for the ground state using the same techniques we used for the iron compounds. We find that for all of these compounds, the polar $a^-a^-c^+$ state is the most stable. This state experiences an unusual non-cooperative J-T distortion, in which all of the long bonds are along a single axis, instead of the alternating long and short bonds in two dimensions seen in the more typical cooperative J-T distortion.[184] This is illustrated in Figure 3.7a. The alignment of long bonds along the *c*-axis leads to a large tetragonal distortion, $c/a = 1.16$ for YBa, which may be responsible for stabilizing the polar state with polarization 15 μC/cm^2. The calculated formation energies of the Mn compounds are shown in Figure 3.7b. For these, we used the Materials Project database[125], so the results are not completely comparable with those for Fe compounds. In addition, the formation energies show the same trend as the difference in the ionic radii of the two *A*-site cations.

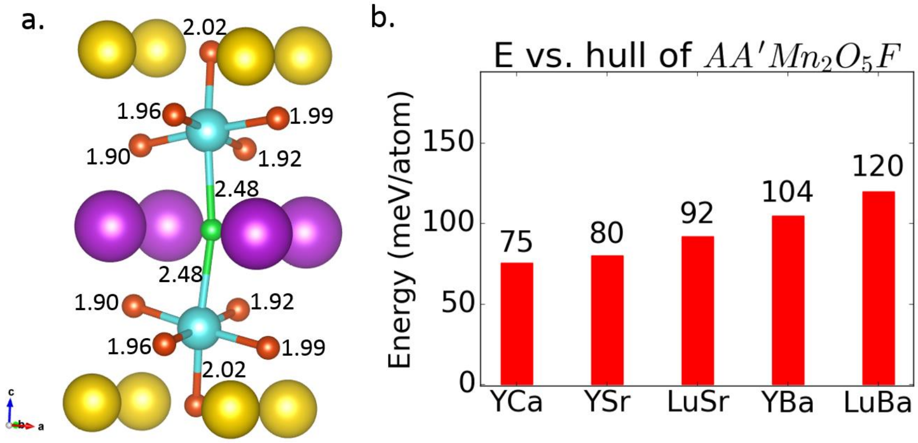

Figure 3.6 Stabilization of the polar phase in Mn compounds.
a. A formula unit of the polar ground state of $YBaMn_2O_5F$, marked with the length of each Mn-*X* bond (Å). b. Formation energy of 6 *AA'*Mn_2O_5F compounds, arranged in order of increasing *A*-site size difference.

3.5 Conclusion

In summary, we have used DFT calculations to investigate the addition of fluorine to layer-ordered double perovskites with Fe or Mn at the *B*-site, with the goal of developing new hybrid improper ferroelectrics with high magnetic ordering temperature. We find that using a +2 and a +3 cation at the *A*-site can increase the polarization of the polar phase with $a^-a^-c^+$ tilts to as high as 19.3 μC/cm^2. The fluorinated Fe perovskites are expected to have high magnetic ordering temperatures due to the strong superexchange interactions between Fe^{3+} ions, while the Mn perovskites may be synthesizable in bulk crystals. Based on these results, we expect that low-temperature fluorination combined with layered ordering of cations will be a valuable tool for synthetic researchers attempting to create new multiferroics. The main advantage of hybrid improper ferroelectrics for this purpose is that the ferroelectricity is generated at the *A*-site, while the magnetism is generated at the *B*-site, which avoids the incompatibility between the two types of ordering which would otherwise make multiferroics very rare.[86] However, the two cation states are still linked by the requirement that the sum of their charges equal +6 per ABX_3 cell to avoid anion deficiency. The use of anion engineering to balance charge provides another degree of freedom which loosens this constraint.

Chapter 4: Prediction and Direct Observation of Apical Oxygen Vacancies in the High-temperature Superconductor $YBa_2Cu_3O_{7-x}$

Sections 4.1-4.4 have been published as S. T. Hartman, B. Mundet, J. C. Idrobo, X. Obradors, T. Puig, J. Gazquez, and R. Mishra, “Direct observation of apical oxygen vacancies in the high-temperature superconductor $YBa_2Cu_3O_{7-x}$” *Physical Review Materials* 3(11), 114806 (2019). Section 4.5 is taken from B. Mundet, S. T. Hartman, R. Guzman, X. Obradors, T. Puig, R. Mishra, and J. Gazquez “Local strain-driven migration of oxygen vacancies to apical sites in $YBa_2Cu_3O_{7-x}$” *Nanoscale* (pages not yet assigned, 2020). I did all of the theoretical calculations presented here. Our collaborators, Dr. Bernat Mundet and Dr. Jaume Gazquez at Institut de Ciència de Materials de Barcelona, performed the synthesis and electron microscopy experiments to characterize the vacancies in YBCO samples.

4.1 Abstract

The properties of the high-temperature superconductor $YBa_2Cu_3O_{7-x}$ (YBCO) depend on the concentration of oxygen vacancies (V_O). It is generally agreed upon that V_O form in the CuO chains, even at low concentrations where the critical temperature for superconductivity peaks ($x \approx 0.07$), with only a handful of reports suggesting the presence of V_O at the apical sites. In this chapter, we show direct evidence of apical V_O in optimally doped YBCO samples. Using density-functional-theory calculations, we predict that isolated V_O are equally favorable to form in either

the CuO chains or the apical sites, which we confirm using atomic-resolution scanning transmission electron microscope imaging and spectroscopy. We further show that apical V_O lead to significant lattice distortions and changes in the electronic structure of YBCO, indicating they should be considered on an equal footing with chain V_O to understand the superconducting properties of YBCO in the optimal doping region. Finally, we examine the underlying cause of apical vacancy formation, and demonstrate that the apical vacancies relieve the compressive strain introduced by the common Y124 stacking fault.

4.2 Introduction

Subtle changes in structure and stoichiometry stemming from defects influence many functional properties of ceramics. A paradigmatic example is the high-temperature superconductor $YBa_2Cu_3O_{7-x}$ (YBCO), where its critical temperature (T_c) and critical current density (J_c) are governed by oxygen vacancies (V_O) [94,185,186]. The structure of YBCO, shown in Fig. 1(a), is that of an oxygen-deficient perovskite. Oxygen is absent from the Y layers, and from half of the sites in the CuO layers present between two BaO layers, which are commonly referred to as CuO chains [187]. The bridging oxygen in these chains can also be removed under reducing conditions, allowing the stoichiometry to vary continuously from $YBa_2Cu_3O_7$ to $YBa_2Cu_3O_6$. Chain V_O lead to structural distortions in their vicinity and dope the system with electrons [185]. Optimal doping, at $x = 0.07$, gives a maximum T_c of 92 K, while $x > 0.55$, destroys the superconducting state [185], thus controlling the oxygen stoichiometry allows a way to tune T_c. J_C is also modulated by the oxygen content, since the magnetic vortex pinning is sensitive to both the carrier concentration and the distortions around V_O [94,186,188].

Oxygen vacancies have received enormous attention, but nearly all past studies have focused on the chain V_O, O(1) in Fig. 1(a). There are three other oxygen sites in YBCO, one apical site in the BaO layer, O(4), and two inequivalent sites in the CuO_2 planes, O(2) and O(3). The attention to the chain vacancies over others can be attributed to two factors. First, the full deoxygenation of the chains under reducing conditions suggests that the chain vacancy ought to be energetically preferable. Second, the position of V_O is commonly detected using diffraction-based techniques involving either X rays, neutrons, or electrons. However, owing to their large interaction volume, such techniques are sensitive only when the vacancy concentration is large; and at large concentrations, V_O in YBCO prefer to order in the chains [189]. Both of these factors obscure the behavior of V_O at small concentrations, or low x, where T_c peaks. Nonetheless, there are a few reports of V_O at sites other than the chains. For instance, neutron diffraction studies [96-98,190,191] have indicated small vacancy concentrations at the apical site O(4), depending on the annealing process. There have been attempts of atomic-scale characterization of V_O on surfaces of cleaved YBCO crystals having optimal doping using scanning tunneling microscopy (STM) [99,192-194]. Pan et al. [99] observed modulations in the intensity of the BaO surface and attributed them to apical vacancies; however, subsequent STM studies did not find any apical vacancies [193] and concluded that the previously observed modulations were due to electronic ordering in the underlying CuO_2 plane [192]. To summarize, while there is some evidence that apical vacancies can form in YBCO at optimal doping, the results are inconclusive owing to either the low spatial resolution of the characterization techniques or to the sample preparation methods. Furthermore, little is known about the conditions that favor the formation of apical vacancies and their effect on YBCO's structure and properties.

In this chapter, we provide direct evidence of apical V_O in optimally doped thin films and single crystals of YBCO by using a combination of aberration-corrected scanning transmission electron microscopy (STEM) and first-principles density-functional-theory (DFT) calculations. Based on DFT calculations, we find that isolated apical V_O have a small formation energy, comparable to that of isolated chain V_O, and should exist across the entire doping range. Using atomic-resolution STEM imaging, we show that apical vacancies are most common in the vicinity of $YBa_2Cu_4O_8$ (YBCO-124) intergrowths, which are prevalent stacking faults formed by the inclusion of a second layer of CuO chains. Furthermore, the observed distortions around the apical vacancies in the STEM images match the equivalent DFT-optimized structural distortions, confirming their origin. We find that the apical vacancies modify the electronic structure of adjacent plane Cu atoms, as shown by simultaneously acquired electron energy loss spectra (EELS) in STEM. DFT calculations show that the apical vacancies increase the electron density of the adjacent superconducting CuO_2 planes. Finally, we compare our results with prevalent models of cuprate superconductivity, and consider how apical vacancies might affect YBCO's superconductive properties.

4.3 Methods

4.3.1 DFT Methods

DFT calculations were performed in the Vienna Ab Initio Simulation Package (VASP) [121,163] using projector-augmented wave potentials and an energy cutoff of 525 eV. *k*-point meshes were created using the generalized Monkhorst-Pack method [122] as implemented on the K-Point Grid Server [195]; relaxations used a minimum real-space distance of 32 Å while high-quality static calculations used 60 Å. Electronic states were smeared with a Gaussian smearing and a smearing width of 0.05 eV. We used the PBEsol exchange-correlation functional [164], and did not use a Hubbard *U* parameter because the metallic state of $YBCO_7$ is reproduced adequately at the GGA level.

4.3.2 STEM Simulations

STEM simulations were done using μSTEM [196]. The input cell was a $(4 \times 4 \times 1)$ supercell with 4 apical vacancies in a row along *b*, which was tiled after relaxation to create a supercell of at least 30 Å in each in-plane direction. The image in Fig. 2(d) uses a 200 kV accelerating voltage with 200 Å sample thickness, 0 defocus, and a 30 mrad aperture cutoff. We used the Quantum Excitation of Phonons method with 20 passes to simulate thermal scattering, and collected electrons from 10 to 30 mrad for the ABF image.

4.3.3 Synthesis

Y123 thin films used in this work were grown by Chemical Solution Deposition. Pristine Y123 thin films were prepared from a methanol-based metal-organic solution containing stoichiometric amounts of Y, Ba and Cu anhydrous trifluoroacetates with a cation molar ratio Y:Ba:Cu of 1:2:3 [197]. This solution was spin coated on 5 x 5 mm $LaAlO_3$ (LAO) single crystal substrates and subsequently exposed to a pyrolysis and crystallization steps to obtain epitaxial c-axis oriented films. The crystallization step takes place at 810-830ºC in a wet atmosphere of 0.2mbar of oxygen (P_{O2}) and the oxygenation process is performed at 450ºC and 1 bar of oxygen pressure. Further details on film preparation can be found elsewhere [198]. These processing conditions lead to a critical temperature Tc = 92 K, and to critical current densities at 77 K of 3 MA cm^{-2}.

4.3.4 STEM/EELS Characterization

A combination of high angle annular dark field (HAADF), or Z-contrast, annular bright field (ABF) and electron energy loss spectroscopy (EELS) have been used to characterize the atomic and chemical structure of the synthesized YBCO thin film. A Nion UltraSTEM 200^{TM} operated at 200 kV, which is equipped with a 5th order aberration-corrector has been used for acquiring the HAADF and ABF images. A Nion UltraSTEM 100 operated at 100 kV, which is equipped with a 5th order aberration-corrector and a Gatan Enfina EEL spectrometer has been used for studying the electronic structure with atomic resolution.

4.4 Results

4.3.1 Vacancy Formation Energy

To assess the favorability of different V_O in the optimal doping region, we calculated the formation energies (E_{form}) of apical, chain, and planar V_O in YBCO by varying x from 0.05 to 0.25 vacancies per formula unit. For $x < 0.15$, we find that isolated apical O(4) and chain O(1) vacancies have similar E_{form}, as shown in Figure 4.1b. For instance, at $x = 0.06$, E_{form} of an isolated apical and chain V_O is 1.35 eV and 1.39 eV, respectively, suggesting that the two are likely to exist at similar concentrations. Although a previous work has examined the ordering of chain vacancies in YBCO at higher V_O concentrations using DFT [189], we are not aware of any first-principles studies comparing the stability of isolated apical and chain vacancies. It is not favorable to form vacancies at the planar sites O(2) and O(3), as they have E_{form} of 1.90 eV and 1.91 eV, respectively, at $x = 0.06$. At higher concentrations, we find that chain vacancy formation benefits from ordering. For instance, for $x = 0.25$, E_{form} of the chain vacancy decreases to 1.13 eV, while it increases for the apical vacancy to 1.58 eV. We find that the lowest energy ordering of chain V_O is an entire chain emptied of oxygen, in agreement with previous experiments [187] and theory [189].

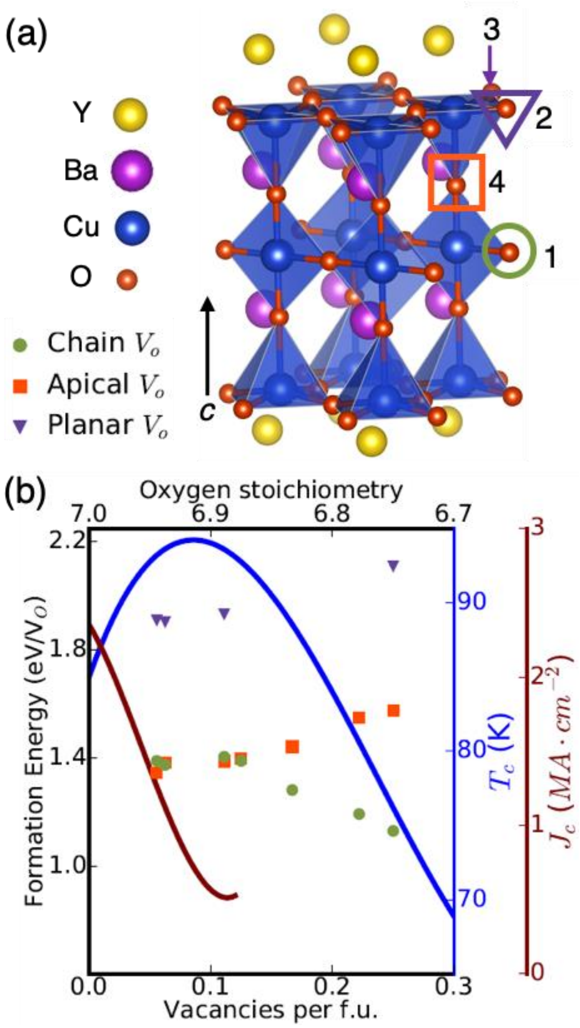

Figure 4.1 Vacancy Formation in YBCO.

(a) The atomic structure of fully oxygenated $YBa_2Cu_3O_7$ ($YBCO_7$). The locations of the four possible oxygen vacancies are marked. (b) Oxygen vacancy formation energy as a function of oxygen stoichiometry, using the same colors and symbols as (a). The solid blue line shows T_C, based on experimental data (Ref.[93] , while the solid brown line shows J_C (Ref. [94] . O(2) and O(3) are combined because they have nearly identical formation energies.

To study the interaction between apical and chain vacancies, we have taken a 3×3×1 supercell having a row of three chain vacancies along the *b* axis, and added an additional vacancy in various positions. We find that adding an apical vacancy to the position above an intact Cu-O chain costs 77 meV more than adding a fourth chain oxygen vacancy. By contrast, placing the apical vacancy directly above the chain vacancies costs 1.88 eV more than the fourth chain vacancy. Therefore, we conclude that apical vacancies are repelled by chain vacancies, as well as by other apical vacancies.

4.3.2 STEM Imaging

We have used STEM annular bright-field (ABF) imaging, which is sensitive to lighter elements [199,200], to identify oxygen vacancies in YBCO samples synthesized by chemical solution deposition. Fig. 2(a) shows an ABF image of YBCO. Fig. 2(b) shows the same image with its contrast inverted to show the oxygen columns in the BaO layers and the CuO chains with more clarity. We show the intensity trace measured along two BaO layers close to a YBCO-124 stacking fault. While the Ba columns have the same intensity for both layers, the O(4) column closer to the film surface has a lower intensity than the O(4) column farther from the surface, indicating the presence of apical vacancies. We observe similar intensity difference for pairs of BaO layers several unit cells away from the faults, with the layer closer to the surface consistently having more apical vacancies. Crystallographically, the near and far planes are equivalent, so the asymmetry in vacancy concentration may be due to kinetic factors during the growth process. We have also performed STEM image simulations on DFT-optimized structures containing O(4) vacancies to directly compare with the experimental images. Fig. 2(d) shows a simulated contrast-inverted ABF image of a DFT-optimized supercell having 25% V_O in one of the BaO planes. We find good agreement between the simulated and experimental intensity profile changes, confirming the presence of apical V_O.

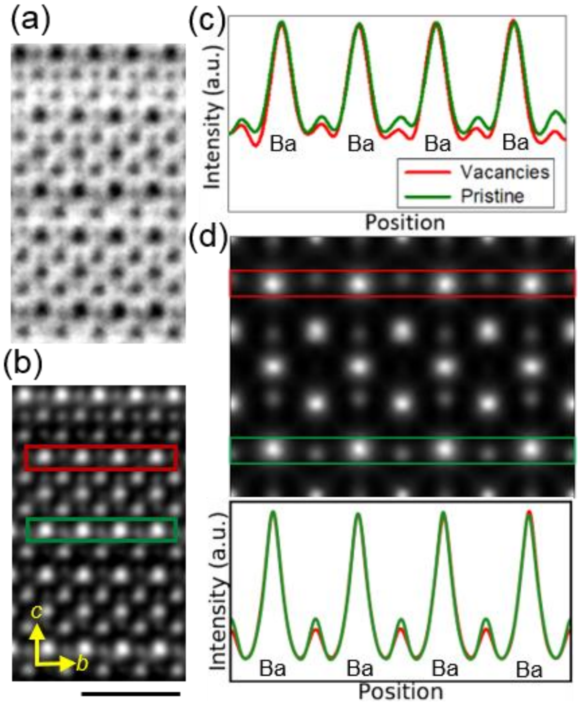

Figure 4.2 Direct Imaging of Apical Oxygen Vacancies.
(a) Raw ABF image of a YBCO thin film with a YBCO-124 intergrowth viewed along the [100] zone axis. (b) The same ABF image with its contrast inverted to show the atomic columns as bright spots. The image has been filtered to reduce the noise. Scale bar: 1 nm. (c) Panel showing two horizontal intensity profiles measured along the BaO planes near to the intergrowth. (d) A simulated ABF image of a YBCO supercell relaxed with 25% oxygen vacancies in one of the apical planes, marked with a red box, which corresponds to the red intensity trace.

Apical vacancies are expected to create structural distortions in their vicinity that serve as additional evidence of their presence. We have quantified these distortions from the ABF images by locating the different atomic columns using a center-of-mass refinement method. By measuring the change in various lattice spacings around BaO layers with or without apical V_O, we have obtained a detailed real-space map of the vacancy-induced structural distortions. For comparison, we have used DFT to optimize a 3×3×1 supercell of stoichiometric $YBCO_7$ with one apical vacancy. We show the largest distortions caused by the apical V_O, both in experiments and DFT calculations, in Fig. 3(a). Due to the apical V_O, the spacing along the *c*-axis between Y and Ba is reduced by 1.5% relative to the regions without apical V_O. The planar Cu atom, adjacent to the vacancies, shifts closer to Y, whereas O(2) and O(3) atoms shift in the opposite direction, changing the planar O–Cu–O angle from 165±2° to 176±2°. This motion also reduces the inter-plane Cu–Cu distance by 5.3%, and increases the distance between planar Cu and the remaining apical O(4) in the atomic column by 8±3%. We find excellent agreement between these observed distortions and the calculated distortions, as shown in Figure 4.3b. The calculated apical V_O causes the copper atoms above and below to move away by 0.18 Å and 0.23 Å, respectively, flattening the in-plane O–Cu–O bond angle from 163^0 to 175^0 and buckling the usually straight (180^0) chain O–Cu–O angle to 154^0. In addition, the adjacent chain oxygen moves towards the vacancy by 0.23 Å.

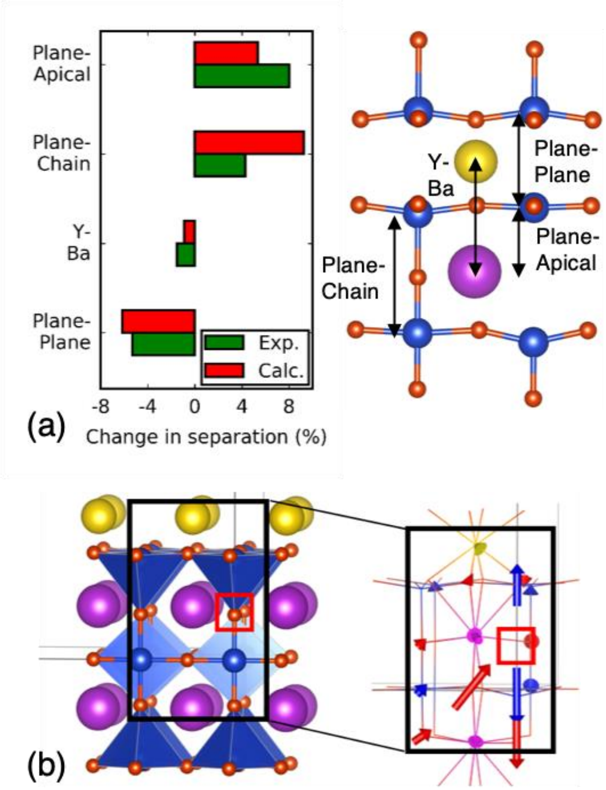

Figure 4.3 Structural Distortions Induced by Apical Vacancies.
(a) The change in the inter-layer separations for the experimental STEM images and the DFT-calculated YBCO structure with apical vacancies. Each separation is labeled in the schematic. (b) Structural relaxation around an apical V_O as calculated using DFT. The left panel shows the location of the vacancy in the pristine $YBCO_7$, while the right panel is a wireframe of the relaxed structure with vectors showing the atomic displacements. The vectors follow the same color scheme as the atoms; red vectors show O movement, blue Cu, magenta Ba, and yellow Y. The vector length is magnified five-fold for clarity.

The presence of apical V_O and the associated distortions affect the local electronic structure of YBCO, as observed from simultaneously acquired EEL spectra. Fig. 4(a) compares the fine structure of the O *K* edge in CuO_2 planes and CuO chains that were acquired from a region of the thin film away from apparent apical V_O. Our results match well with those obtained by Gauquelin et al. [201] from a YBCO single crystal that we take as a reference to validate the quality of our EELS measurements. The pre-peak of the O *K* edge is sensitive to the filling of the unoccupied, hybridized O-*2p* and Cu-*3d* states, and is observed to shift to higher energies with oxygen vacancies, due to the electron doping [201]. In addition, our observation of the pre-peak onset at 527 eV for the CuO chains and 528.5 eV for the CuO_2 planes is consistent with previous results for $YBCO_{6.97}$ single crystals [201], indicating that our thin films have the optimal oxygen concentration.

We now show the difference in O *K* and Cu *L* edges in the EEL spectra of two superconducting CuO_2 planes with and without adjacent apical V_O in Fig. 4(b) and 4(c), respectively. For the planar O *K* edge, the most notable difference is the decrease in the intensity of the pre-peak in the planes adjacent to the apical V_O. We attribute this to electron doping by the adjacent apical V_O of the previously unoccupied O 2*p* states hybridized with Cu 3*d* in the superconducting planes. The Cu *L*-edge also changes when comparing the two superconducting

CuO_2 planes. Notice that the intensity of the Cu L_3-edge (centered at 931.5 eV) increases with apical vacancies, which constitutes a second experimental evidence of an electronic reconstruction. The DFT-calculated electronic density of states (DOS) for the planar Cu and planar O adjacent to an apical V_O are shown in Fig. 4(d), compared with the same atoms in pristine YBCO. The formation of an apical V_O eliminates the overlap between the apical oxygen's $2p_z$ states and the neighboring planar copper's $3d_{z^2}$ states, reducing the bandwidth by ~2 eV. This interaction is anti-bonding near the Fermi energy, so the resulting non-bonding Cu $3d_{z^2}$ state drops below the Fermi energy. The remaining planar Cu DOS at the Fermi energy comes from the $3d_{x^2-y^2}$ states, which retain their bandwidth after the apical vacancy formation.

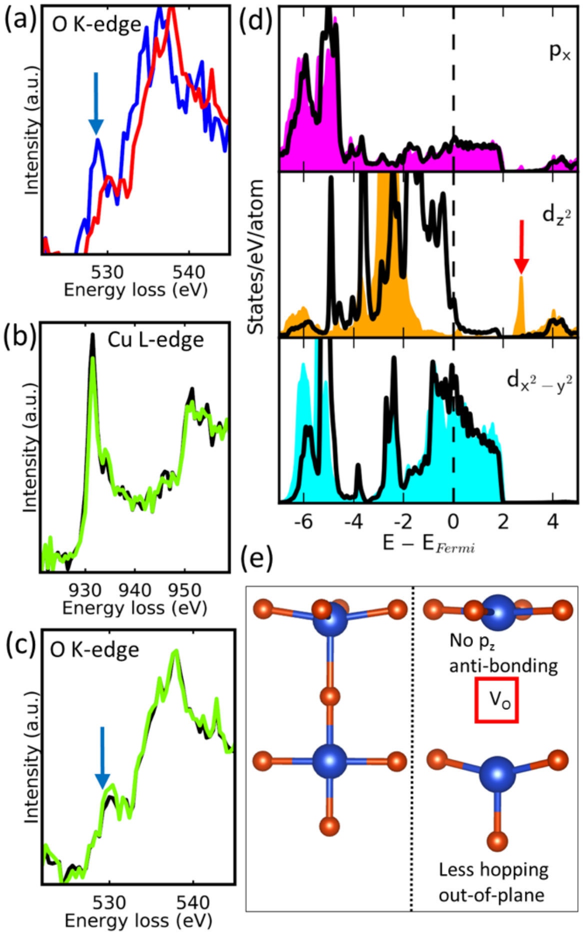

Figure 4.4 Electronic Effects of Apical Vacancies.

(a) EELS O *K*-edge spectra obtained from the chain O(1) (blue) and plane O(2), O(3) (red) of optimally doped YBCO thin films. The pre-peak is marked with an arrow. (b) Comparison of Cu *L*-edge spectra from CuO_2 planes closer to the film surface (black) with more apical V_O and farther from it with fewer apical V_O (green). (c) Comparison of O *K*-edge spectra from the same CuO_2 planes as in (b). (d) The orbital-projected DOS of the superconducting CuO_2 plane atoms directly adjacent to an apical vacancy. The planar O p_x, Cu $3d_{z^2}$ and Cu $3d_{x^2-y^2}$ states are in magenta, gold, and blue, respectively. The states near 3 eV, highlighted by an arrow correspond to the axial orbital as proposed by Pavarini et al. [202]. The black line in the DOS plots corresponds to pristine YBCO, shown for comparison. (e) Schematic of the plane-chain system before and after the apical oxygen is removed.

4.4 Apical Vacancies and Superconductivity

The apical oxygen has been shown to affect the superconducting properties of YBCO. For instance, a recent investigation [203] of the magnetic excitations in cuprates with zero, one, or two apical oxygen per CuO_2 plane concluded that the structure without apical oxygen had the most long-range electron hopping. Likewise, any strain or distortion of the CuO_2 planes is likely to alter the pair condensation energy and its J_C [186]. Hence, we consider the implications of apical V_O.

Pavarini et al., [202] have ascribed an important role to the "axial" molecular orbital, composed of planar Cu 4*s* and $3d_{z^2}$ states antibonding to apical O $2p_z$ states. The axial orbital is above the Fermi energy, and its calculated energy is correlated with T_c; as the axial orbital approaches the Fermi energy, T_c goes up. Increasing the planar Cu–O(4) bond length is predicted to raise T_c by reducing the antibonding contribution to the axial orbital. Removing the apical oxygen is equivalent to a large bond length increase, along with the addition of electrons. It results in the axial orbital, located ~3 eV above Fermi energy as shown in Fig. 4(d), being entirely composed of Cu 4*s* states. The change may favor in-plane superconductivity, as it has been shown that the single-layer cuprate superconductor having the highest T_c, $HgBa_2CuO_4$, has the most Cu *4s* character in its axial orbital [202]. However, later studies of the role of apical bonding have not all followed the same conclusion. One recent study found no correlation between apical bond length and T_c across many different cuprates, and instead found T_c was correlated with the strength of the bond between the O(4) and the chain Cu [204].

A second well-known model focuses on out-of-plane transport, treating the CuO_2 planes as perfect superconductors and modeling conductivity out of plane as tunneling through a Josephson junction [205]. According to this model, the tunneling barrier between CuO_2 planes is the limiting factor, and anything which shortens the planar Cu–O(4) bond might raise T_c. For example, vacancy-ordered $YBCO_{6.5}$ showed coherent transport near room temperature on optically exciting a phonon mode specific to the Cu–O(4) bond [206,207]. Time-resolved diffraction and theoretical calculations indicated that the excited mode increased planar buckling [207], which ought to reduce in-plane transport but improve out-of-plane transport. According to this model, apical V_O is likely to weaken the out-of-plane superconductivity.

4.5 Effect of Compressive Strain

We have seen that the apical V_O can be stable, and we have observed them in optimally doped YBCO samples, but we want to know more about what promotes or hinders their formation. Since apical V_O are likely to influence superconductivity, gaining experimental control of their concentration is also a matter of significant practical importance when optimizing synthesis procedures. Our STEM imaging provides an important clue regarding the cause of apical V_O formation: the apical vacancies are most common near the Y124 intergrowths, which are a stacking fault consisting of a doubled chain of Cu-O-Cu instead of the usual single chain.[208]

As the Y124 intergrowths have a finite length, they expand the crystal lattice locally by a sixth of the c-axis (c/6) along the out-of-plane direction. We can measure this expansion precisely using a center-of-mass refinement method with picometer resolution to locate each atomic column, as previously shown by Roger et al. [30]. We have applied this procedure to each unit cell in an area like the one shown in Figure 4.5a, which shows a high-resolution Z-contrast image with two Y124 intergrowths in the center separated by 4-unit cells. While the lower intergrowth crosses the full image, the upper one begins in middle of the image (the yellow cross signals the associated partial dislocation). Accordingly, the right side of the image contains one additional Cu-O plane, which implies that the system adapts to include the c/6 out-of-plane expansion. We can generate a c-axis map, where each pixel in the map represents the interplanar distance per atomic row. We have plotted two averaged line profiles in Figure 4.5a, left inset, which extend across either one intergrowth (profile 1 in red) or two intergrowths (profile 2 in cyan). The given values of profile 1 and 2 have been calculated taking 13-unit cells along the basal plane, leading to a statistical error of 0.09 Å. The yellow line represents the YBCO out-of-plane parameter (c=11.68 Å) of the bulk. From these values, we have also calculated their corresponding c-axis strain depth-profiles (see Fig.4a right inset), which are obtained from the following expression: $\varepsilon_c = (c_{imaged} - c_{bulk})/c_{bulk} \times 100$.

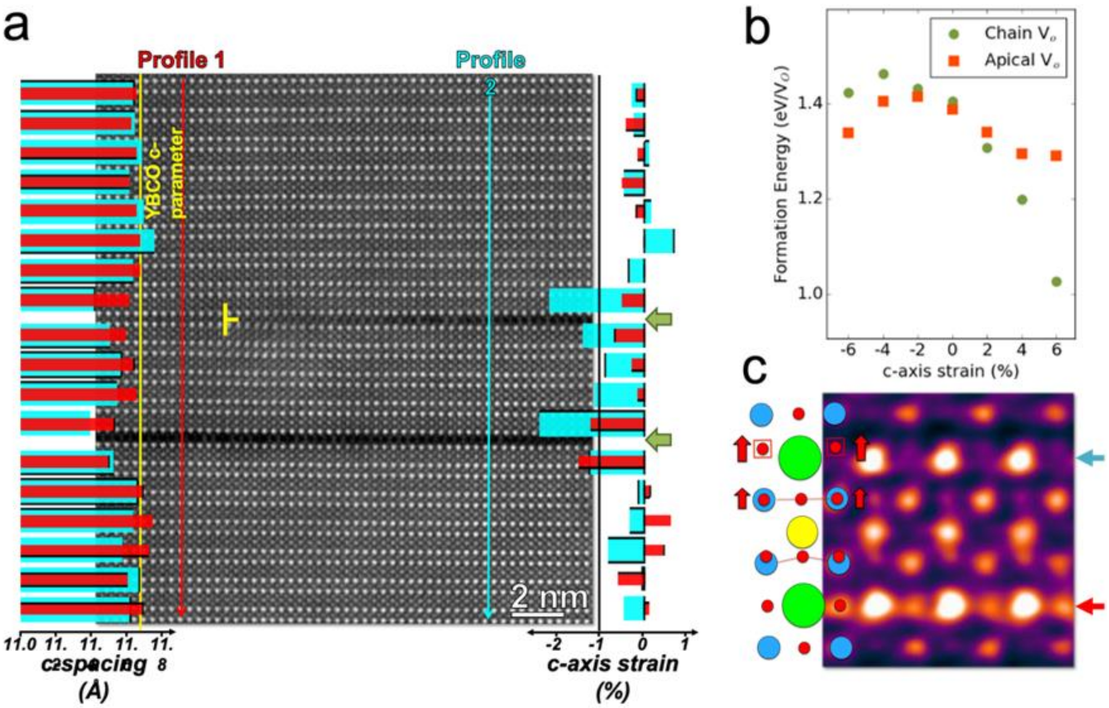

Figure 4.5 Strain Stabilization of Apical Vacancies.

(a) HAADF image of a YBCO film region containing two Y124 intergrowths (green arrows), one crossing the full image and the other one starting at the middle of the viewed area (yellow cross). Superimposed at the left side of the HAADF image are the c-parameter depth-profiles measured at the left (red vertical arrow) and right (blue vertical arrow) sides of the HAADF image. One of the Ba-Ba spacings located between both intergrowths has been used twice in the calculations, as the crystal periodicity is broken at the planar defect. The yellow line represents the fully relaxed YBCO c-axis parameter. Superimposed at the right side of the HAADF image are the depth-profiles of c-axis strain calculated from the previous c-parameter depth-profiles. (b) DFT-calculated formation energy of one

VO located at either the chain (green dots) or apical (orange squares) sites as a function of uniaxial strain along the c-axis. Negative/positive strain values represent compressive/tensile uniaxial strains. (c) Illustration of the distorted YBCO unit cell, which is superimposed onto an enlarged image region of the contrast-inverted ABF image shown in Fig. 1c. Ba, Y, Cu and O atoms are represented with green, blue, yellow and red circles. The red arrows represent the atomic shifts occurring in the oxygen sub-lattice.

Profile 1 and profile 2 show that far from the Y124 intergrowths the c-parameter matches that of bulk YBCO. However, the cells located close to the Y124 intergrowths are significantly compressed, especially in the first unit cell on either side of the intergrowth, with compressive strain values larger than −1%. This effect is magnified in the area between the two intergrowths (crossed by profile 2), where the compression exceeds −2%. These results show that Y124 intergrowths induce a local compressive deformation along the *c*-axis. Accordingly, we have calculated how the formation energy of isolated chain $V_{O(1)}$ and apical $V_{O(4)}$ changes as a function of strain along the c-axis. The results are plotted in Fig. 4b, which shows that for a tensile deformation (positive strain values), both vacancies, $V_{O(1)}$ and $V_{O(4)}$, are more probable to appear when compared to bulk YBCO (strain-free), as their formation energy is lowered. Yet, as the tensile strain increases, the formation energy of the chain $V_{O(1)}$ decreases more rapidly. On the other hand, under a small compressive strain ($< -2\%$), the formation energy of both $V_{O(1)}$ and $V_{O(4)}$ increases, but the increase is weaker for the apical $V_{O(4)}$ and it becomes more stable than the $V_{O(1)}$. With large compressive strains ~ −6%, the formation energy of $V_{O(4)}$ is lowered that that in bulk YBCO. These results suggest that the local compressive strain arising due to Y124 intergrowth increases the formation of apical oxygen vacancies than chain vacancies.

We have used ABF imaging to monitor the picometer-scale lattice distortions occurring within the oxygen sub-lattice near to $V_{O(4)}$. Fig. 4c displays an enlarged view of the contrast-inverted ABF image that is shown in Fig. 1c. As sketched in the inset, the oxygen atoms belonging to the upper superconducting plane and apical positions are shifted upwards. On the one hand, these atomic shifts enlarge the spacing between the upper superconducting plane and its corresponding apical oxygen (the one located within the BaO(2) plane) by (8±3)%, compared to the same spacing of the superconducting plane that is connected to the fully oxygenated BaO(1) plane. On the other hand, the oxygen displacements occurring in the upper superconducting plane also increase the Cu–O–Cu buckling angle up to a value of (176±2)º, nearly eliminating the rippling pattern that is commonly displayed by the Cu and O atoms when moving along the basal direction in the undistorted superconducting planes.

Using DFT, we have investigated how the combination of compressive strain and apical vacancies affect the atomic structure and electronic properties of YBCO. We show the variation of three key quantities with uniaxial strain along the *c*-axis in Fig. 5: the planar O–Cu–O buckling angle in Fig. 5a; the in-plane O–Cu bond length in Fig. 5b, and the apical O–Cu bond length in Fig. 5c. All quantities are calculated for the pristine YBCO unit cell, and for 3×3×1 supercells containing a single oxygen vacancy either at the apical or chain site. In the presence of vacancies, the above quantities are measured next to the vacancy. Looking first at the buckling angles in Fig. 5a, we see that the CuO_2 planar unit next to a $V_{O(4)}$, which is flatter than normal even without strain, becomes almost perfectly flat (approaching 180°) under compression.

Comparing this relation with that of the pristine YBCO immediately suggests a reason $V_{O(4)}$ are preferred under compression. A planar Cu adjacent to an apical vacancy is underbonded and will tend to move closer to the planar O. This coincides with the strain-induced tendency to reduced buckling of the CuO_2 planes, which stabilizes the structure. We note that Poisson's effect leads to an expansion of the planar units under compression, as shown in Fig. 5b. In principle, this in-plane expansion could make the planar Cu underbonding near a $V_{O(4)}$ even worse, but Poisson's effect also lengthens the Cu-O chains by an equal amount, and so it has little influence on the relative stability of different V_O. Finally, we note that the apical bond length reduction in Fig. 5c might destabilize the pristine and chain vacancy structures, but this is not an issue if the apical O is no longer present.

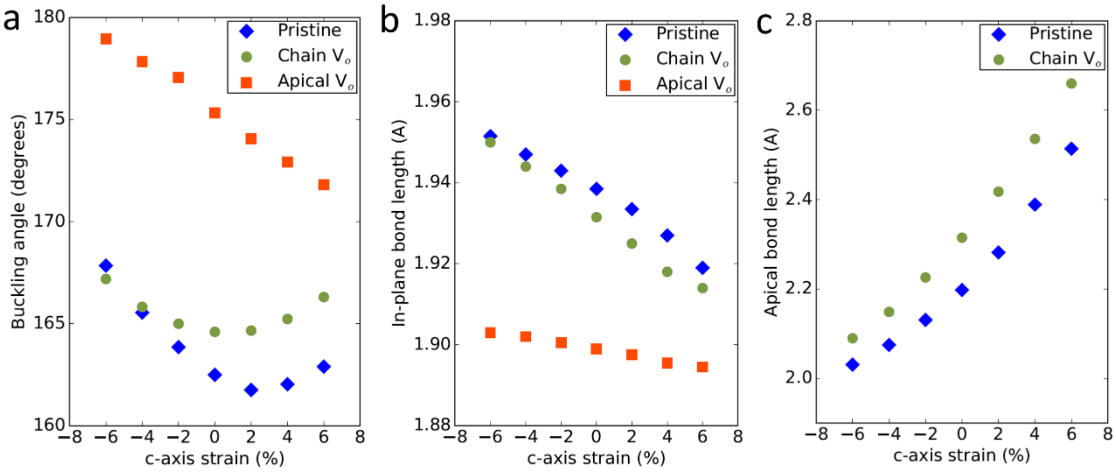

Figure 4.6 Local Structural Response to Applied Strain.
(a) The in-plane O-Cu-O buckling angle for a 331 DFT-calculated YBCO supercell, as a function of applied strain along the *c*-axis. If the cell contains a chain V_O (green dot) or apical V_O, the buckling angle is measured in the CuO_2 planar unit closest to the vacancy. (b) The planar Cu/planar O bond length for the same planar units as (a). (c) The planar Cu/apical O bond length for the pristine and chain vacancy structures, again for the same cells as (a).

Finally, we examine the electronic effects of these structural distortions in the presence of both apical vacancies and compressive strain. As shown in Fig. 5a, the planar buckling is one of the key variables in YBCO which changes in response to structural disturbances, especially apical vacancies. We wish to separate the electronic effects caused directly by the apical vacancy, from those caused indirectly by its effect on the planar buckling, and so in Fig. 6a we show the electronic effects in pristine YBCO of varying one of the phonon modes associated with planar buckling. Image #5, with flat CuO_2 planes, most closely resembles the apical vacancy structure. There are two main effects; first, the planar increases in bandwidth by about 1.5 eV as the planar flattening improves the in-plane orbital overlap. Second, the unfilled band composed of planar Cu 4*s*, planar , and apical O , which is the "axial orbital" of Pavarini et al. [42], moves 2 eV closer to the Fermi level and becomes narrower. These effects are due to the motion of the apical O away from the plane, which is coupled to the motion of the planar O as part of the buckling mode, and creates effects similar to the presence of an apical vacancy.

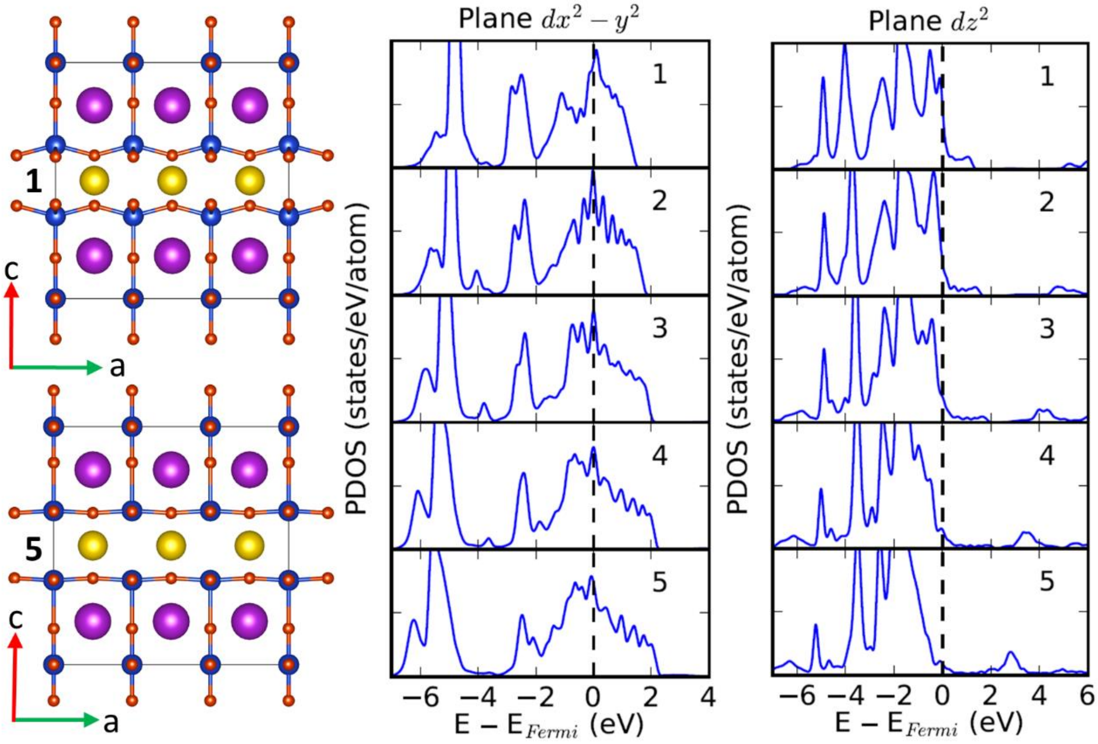

Figure 4.7 The effect of a planar buckling mode on the planar copper's electronic density of states.

The plots show the density of states of pristine YBCO, projected onto a local orbital basis (PDOS). We take five images of the mode, with image 1 having maximum buckling and image 5 having completely flat planes, as shown by the structures at left. Energies are given relative to the Fermi energy.

Summing up, we predict with first-principles calculations that apical oxygen vacancies are stable in YBCO at low concentrations, and then we use the combination of Z-contrast and annular bright-field imaging modes to observe them directly. The observed crystal structure distortions agree well with those predicted theoretically, providing further evidence for apical vacancy formation. Due to their structural effect on the CuO_2 plane, which is to flatten the buckled Cu-O bonds, we expect that the apical vacancies will influence the superconducting properties of optimally doped YBCO. In subsequent work, we examine the driving force for apical vacancy formation. We demonstrate using STEM that they are present whenever a Y124 intergrowth is formed, either in a YBCO thin film or in a single crystal. The regions of apical vacancy formation are compressively strained, and DFT calculations confirm that compressive strain favors the apical vacancy relative to the better-known chain oxygen vacancy.

Chapter 5: New Ferroelectric Semiconductors with Band Gaps in the Visible Spectrum

Chapter 5 is in preparation for submission as S. T. Hartman, A. S. Thind, and R. Mishra "New Ferroelectric Semiconductors with Band Gaps in the Visible Spectrum" (2020). A. S. Thind did preliminary calculations of certain oxynitrides in the perovskite structure.

5.1 Abstract

The valuable electronic properties of the lead-halide and tin-halide perovskites are derived from the substantially covalent bonding between halide anions and *p*-block cations. However, the weakness of these bonds leads to stability problems under realistic operating conditions for many devices. This study proposes a new family of $A^{3+}SnO_2N$ tin oxynitrides in the $LuMnO_3$ structure, which can combine the strong bonding of metal oxides with the electron mobility and small, tunable band gaps of the halide perovskites. The new materials have predicted band gap values ranging from 1.6 to 3.3 eV, and electric polarization up to 17 μC/cm^2. Since the conduction band minima are composed of dispersive Sn *s*-orbitals, the electron effective masses are as light as 0.12 m_0.

5.2 Introduction

Lead-halide perovskites, such as methylammonium lead trihalide ($CH_3NH_3PbI_3$), have emerged as promising, high-performance semiconductors for solar cell absorbers with power conversion efficiency surpassing 25%.[209] They have tunable band gaps and high optical absorbance to efficiently utilize the incoming solar radiation.[210] They also possess long charge carrier lifetimes and carrier diffusion lengths that enables effective separation of the photogenerated electrons and holes.[211-213] The large carrier lifetimes and diffusion lengths are due to an interplay of various factors including low effective mass of the carriers,[214] large dielectric constant,[215] and their high defect tolerance,[216-219] wherein the semiconductors are able to retain the electronic properties of their pristine form even in the presence of common defects. Another factor that can enhance carrier separation is the presence of ferroelectric domains wherein the in-built electric field can facilitate transport of the electrons and holes to opposite domain boundaries.[220] Ordered domain structures can further provide pathways for efficient carrier extraction at the surface of the absorber layer.[221] However, the extent to which ferroelectricity enhances charge separation in $CH_3NH_3PbI_3$ is under significant debate as there are conflicting reports on the ferroelectric nature of $CH_3NH_3PbI_3$ with some suggesting $CH_3NH_3PbI_3$ to be ferroelectric[222-225] while others implying it to be non-ferroelectric,[226-228] or even antiferroelectric.[229] Polar ordering in $CH_3NH_3PbI_3$ is weak as it originates from the orientation of the rotating and vibrating polar organic cations ($CH_3NH_3^+$) and their weak interaction with the neighboring halide ions through hydrogen bonds.[221,227,230]

Despite their superior performance, $CH_3NH_3PbI_3$ and other organic lead-halide perovskites are plagued with issues related to environmental and thermodynamic instability,[231,232] which combined with the highly toxic nature of lead, makes them less prospective for widespread commercialization.[233,234] Hence, there is ongoing search for stable, lead-free perovskites that can emulate the performance of lead-halide perovskite solar cells.[211,235-240] Such searches, for the most part, have been restricted to halides of heavier *p*-block cations, such as Ge, Sn, and Bi, having the perovskite framework. The band edges of such compounds are made up of spatially delocalized *s* or *p*, states which combine with the three-dimension corner connectivity of the perovskite framework to create dispersive bands with low carrier effective masses.[214,241,242] However, these lead-free halides also suffer from long-term stability issues on exposure of ambient air, temperature and light.[238] Their low stability can be attributed to the strength of the metal-halide bond, which is weaker than metal-oxide or -nitride bonds.[104] In the context of stability, Bi-based oxide double perovskites,[243] such as $KBaTeBiO_6$,[236] have been recently shown as a promising composition space to search for lead-free replacements. However, the proposed alternatives have not been able to replicate the increase in efficiency that lead-halide perovskite solar cells have undergone. The ideal replacement should display similar direct band gap, carrier effective masses, and absorbance as $CH_3NH_3PbI_3$ with added stability. The performance of such semiconductors in solar cells could be further enhanced if they display robust polarization.

In this work, we use a first-principles computational approach to design a new family of stable, Sn-based oxynitride ferroelectric semiconductors, as potential replacements for lead-halide perovskites. We search a vast composition space of ABO_2N and $ABON_2$ stoichiometries, where B is a *p*-block cation, and A is an alkaline, alkali-earth, rare-earth or transition metal cation, and identify 10 new ABO_2N oxynitrides that we expect to be formable. Of these, the $A\mathrm{SnO_2N}$ family stands out for its promising electronic properties. We find $YSnO_2N$ and $EuSnO_2N$ to be on the convex hull of competing phases, and three others $A\mathrm{SnO_2N}$ (A = La, In, Sc) have a formation enthalpy <94 meV/atom from the hull, within the typical range of formability for oxides and nitrides.[110] These Sn-oxynitrides adopt the $LuMnO_3$ structure,[244] in which a concerted motion of the *A*-site cations couples with polyhedral tilting [245] to create a sizeable spontaneous polarization between 7 – 17 μC/cm^2. We predict that the *A*SnO_2N materials have band gaps ranging from 1.6 to 3.3 eV, with a dispersive conduction band leading to low electron effective masses of (0.1 – 0.3)m_0 (where m_0 is the mass of a free electron), values comparable to $CH_3NH_3PbI_3$.[214] Specifically, we predict $InSnO_2N$ — that has a direct band gap of 1.6 eV, a spontaneous polarization of 9.9 μC/cm^2 and good formability (50 meV/atom above the convex hull) — to be a promising candidate for solar cell absorbers. With their unique combination of properties and band gaps spanning the entire visible spectrum, we expect *A*SnO_2N ferroelectric semiconductors will find useful applications as photovoltaics, photocatalysts, and for optoelectronics.

5.3 Design and Search Strategy

Our interest in oxynitrides stems from their potential to combine many of the favorable aspects of both halides and oxides. The poor stability of the heavy-metal halide perovskites could be overcome by replacing the halogens with oxygen or nitrogen, since metal oxides and nitrides are much more strongly bonded. However, the large electronegativity of oxygen results in a low valence band maximum (VBM),[246] and the resulting materials have large band gaps, making them sub-optimal for solar energy harvesting. This band gap increase can potentially be mitigated by incorporating nitrogen to raise the VBM.[58,247] For instance, while the oxide perovskite $CaNbO_3$ shows a large band gap of 4.03 eV,[248] its isostructural oxynitride counterpart, $CaNbO_2N$, shows a band gap of 2.1 eV.[247] Previous works on *AB*O_2N oxynitrides have mainly focused on transition-metal cations at the *B*-site, especially those that prefer oxidation states of +4 and higher such as Ta^{5+}, Nb^{5+}, and Hf^{4+}.[249,250] These transition metal oxynitrides have proven useful for photocatalysis, but their localized *d*-orbitals at the band edge reduce their electron and hole mobility. Because we want to find good semiconducting materials, we move beyond the known oxynitrides to focus on *p*-block cations at the *B*-site, to discover semiconductors with dispersive bands and band gap in the visible region.

Our search strategy for finding heavy-metal oxynitrides is illustrated in Figure 5.1 (see methods section and for additional details). We choose *A*-site cations from the left side of the periodic table, while *B* is a *p*-block cation, and we require that each composition be charge-balanced in common oxidation states of the cations. The charge-balance requirement restricts the number of ABO_2N and $ABON_2$ compositions to 130 and 76, respectively. We then construct each composition in different structural prototypes observed in ABO_3 oxides, chosen from the perovskite, $LiNbO_3$, $FeTiO_3$, $BaSiO_3$, $CdSiO_3$, $AlSbO_3$, $GePbO_3$, $BaGeO_3$, and $YSiO_2N$ structure types. Specifically, we tested perovskites in the common $a^-a^-c^+$, $a^0a^0c^-$, and $a^-a^-a^-$ octahedral tilting patterns. For the polymorphs with a 6-coordinate *B*-site, we considered several different O-N anion orderings, most *cis*-ordered about each octahedra with either 2D or 3D N-M-N chains.[60] In some cases, we also tested *trans* anion ordering but it was not stable. For the 4-coordinate *B*-sites, we always placed the N at the bridging position which connected adjacent tetrahedra, since this is likely to have the highest site potential. We did not test every potential charge-balanced composition with every structure; for example, we did not calculate the $BaGeO_3$ or $BaSiO_3$ structures with transition metals at the *A* site, due to the large ionic size mismatch between Ba (1.42 Å VIII-coordinate) and transition metals such as Zr (0.84 Å VIII-coordinate).

Then we calculate the new oxynitride's thermodynamic stability after structural relaxation. We do this by calculating the formation enthalpy of the most stable ABO_2N structure with respect to the convex hull of most stable reactants, which can be either elements or compounds, as found in the Materials Project database.[125] This first step reveals that all the *AB*ON$_2$ materials which we calculate are >140 meV/atom above the convex hull, and so they are not considered further.

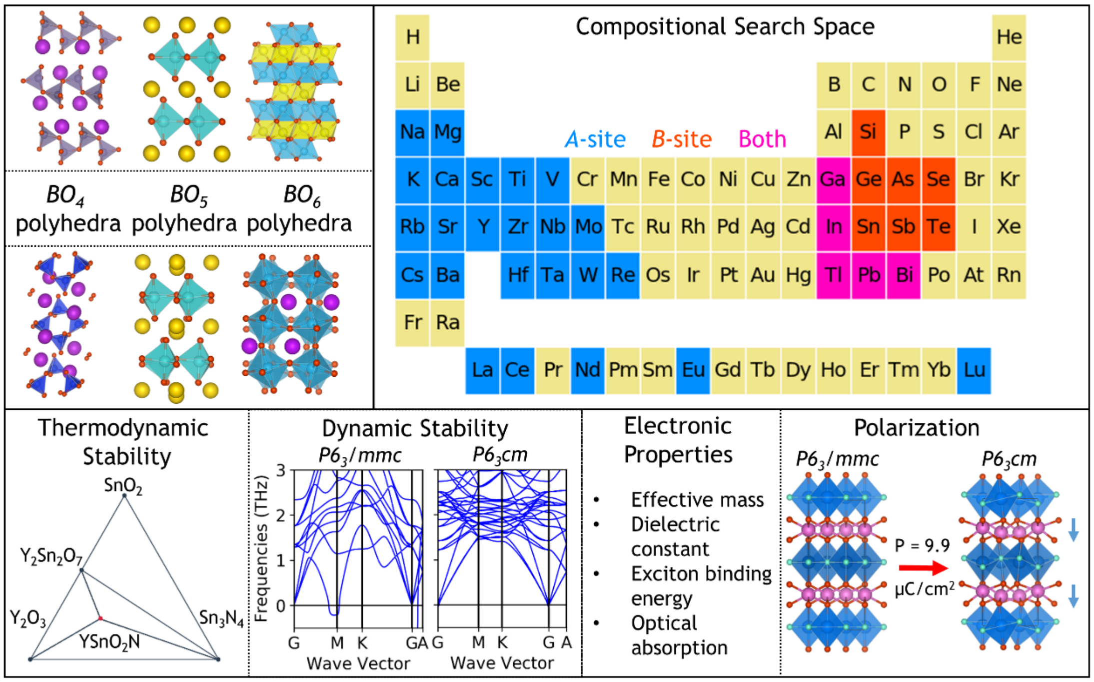

Figure 5.1 A schematic of the search strategy used in this work.
We substituted common oxide and oxynitride structural prototypes with the *A*- and *B*-site cations shown on the periodic table. All new materials were checked for stability or metastability versus known phases in the same composition space. We used mode analysis and phonon calculations to demonstrate the potential ferroelectricity of the stable *A*SnO$_2$N family, and then we analyzed their electronic properties.

5.4 Results

5.4.1 Stability of Competing Structure Types

Our computational screening reveals that *AB*O$_2$N compounds, with *B* chosen from the *p*-block elements, do not typically adopt the common perovskite structure. We tested perovskites having different octahedral tilt patterns and found them to be >100 meV/atom above the convex hull. Instead, we find that the smaller *B*-site cations, such as Si^{4+} (0.4 Å VI-coordinate), As^{5+} (0.46

Å), or Ge^{4+} (0.53 Å), favor tetrahedral coordination, while the larger Sn^{4+} cation (0.69 Å) is more stable in a 5-coordinate environment with trigonal bipyramid coordination.

We find this coordination is stabilized in the oxynitrides by anion ordering, due to the higher site potential of the equatorial site.[31,33,251,252] the equatorial anion sits in a distorted tetrahedron of three Sn^{4+} and one A^{3+}, while the apical anion sits in a distorted tetrahedron of three A^{3+} and one Sn^{4+}. According to Pauling's second crystal rule, the equatorial site is therefore better for the more highly charged anion.[31,33,251] To illustrate the electrostatic effect, we also calculate the electrostatic site potential for the O^{2-} and N^{3-} anion sites in $YSnO_2N$,[253] considering all ions to be in their formal oxidation states. We used an ion sphere radius of 1.5 Å and a reciprocal-space range of 4 $Å^{-1}$. The average equatorial site potential is 35.6 V, compared to an apical site potential of 21.8 V. Of course, this includes the potential from the anion occupying the site; removing one anion and re-calculating the potential at the vacancy, without relaxation, gives values of 22.5 V for the equatorial site and 13.3 V for the apical site. Creation of an unrelaxed anti-site O^{2-}/N^{3-} pair costs 7.29 eV of electrostatic energy, while relaxing it with DFT still leaves a formation energy of 1.14 eV, indicating a strict anion ordering which contrasts with the partial order of the octahedral perovskite oxynitrides.[56] Based on these results, we conclude that electrostatics provide a strong driving force to put the nitride on the equatorial site in $YSnO_2N$, just as in structurally related $YSiO_2N$.

With several possible 4- and 5-coordinate structures to choose from, we examine their symmetry relations in **Figure 2**. The high-symmetry 5-coordinate *P6₃/mmc* structure of Figure 2a has a two-dimensional network of corner-sharing trigonal bipyramids, and is known in a few materials such as high-pressure $InGaO_3$.[254] None of the ABO_2N compositions we have tested have a $P6_3/mmc$ ground state, however. We find that reducing the size of the *B*-site cation contracts the coordination environment to tetrahedral, breaking the bonding network into the isolated rings of Figure 2b, as observed in anion-ordered $YSiO_2N$.[252] The $YSiO_2N$-type structure has been represented with the 30-atom centrosymmetric *Cmcm* unit cell in Figure 2a. While stacking patterns along the *c*-axis can potentially reduce symmetry to polar $P6_122$,[255] both ring structures have wide band gaps and flat bands, which is a consequence of the breaking in polyhedral connectivity.[214,241] We find that ABO_2N (B = Si, Ge, As) all adopt this structure type, with $YSiO_2N$, $EuGeO_2N$, $LaGeO_2N$, $BaAsO_2N$, $CaAsO_2N$, and $SrAsO_2N$ less than 94 meV/atom above the convex hull, a stability criterion which encompasses 90% of known metastable binary oxides calculated with the same DFT parameters as we use here.[110] Because the *Cmcm* materials are insulators with PBE band gaps > 2.5 eV, we do not investigate these tetrahedral ring structures any further in this paper.

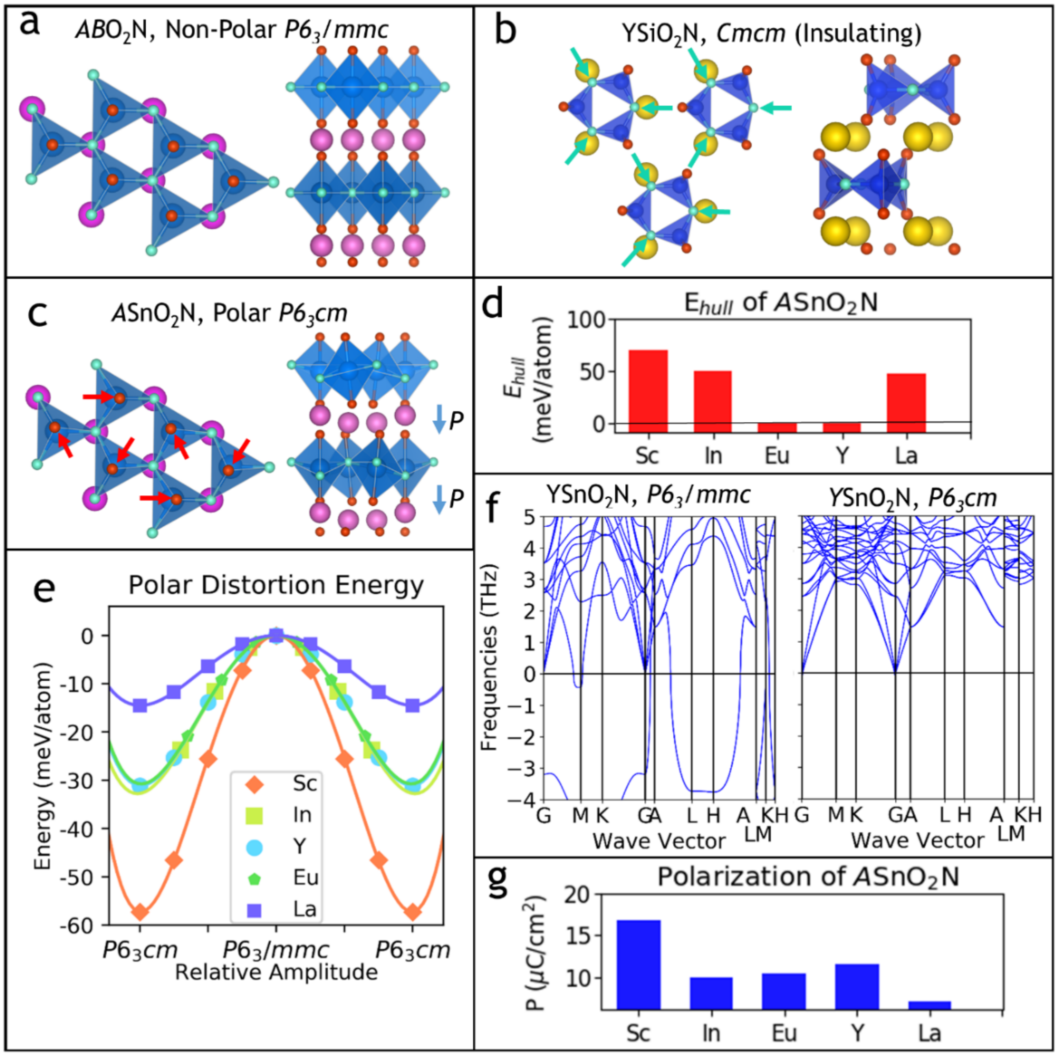

Figure 5.2 Structural Transitions of Novel $ASnO_2N$ Semiconductors

a. The centrosymmetric *P6₃/mmc* structure of ABO_2N, with no polyhedral tilting. b. The polar and insulating *Cmcm* structure adopted by $YSiO_2N$,[252] and other ABO_2N with small *B*. The arrows illustrate the creation of isolated rings as the *B*-site coordination contracts. c. The polar and semiconducting *P6₃cm* structure which is the ground state of $ASnO_2N$ (*A*=Sc, In, Eu, Y, La). The arrows illustrate the polyhedral tilting mode which creates a polarization along the *c*-axis (see 2g for the polarization values). d. Convex hull energies of $ASnO_2N$ with *A* = Sc, In, Eu, Y, La plotted in order of increasing Shannon ionic radius.[38] e. The ferroelectric double-well potential for $ASnO_2N$ as they are switched through the centrosymmetric *P6₃/mmc* phase. f. The calculated phonon spectrum for $YSnO_2N$, in the unstable centrosymmetric *P6₃/mmc* phase (left) with negative phonon frequencies, and the stable polar *P6₃cm* phase (right) with strictly positive phonon frequencies. g. The calculated spontaneous polarization of $ASnO_2N$ along the *c*-axis.

Keeping the *B*-site fixed at Sn^{4+}, but reducing the *A*-site radius, introduces polyhedral tilting to reduce the coordination number of *A* from 8 to 7, as demonstrated previously in the hexagonal manganite multiferroics.[245] The tilting of the trigonal bipyramids shown in Figure 2c removes the center of inversion symmetry located at the *A*-site, lowering the symmetry to polar $P6_3cm$,[245] and the *A*-site cations displace along the *c*-axis. The unit cell triples to include 6 *A* cations, of which 4 displace one direction, and two the other, creating a dipole ~10μC/cm^2. This transition, which is driven by the size mismatch of the two cations, is known as a geometric ferroelectric transition, in contrast to ferroelectrics driven by lone-pair stereochemistry, such as $BiFeO_3$, or by bond hybridization around d^0 cations, such as $BaTiO_3$.[256] Two $P6_3mc$ structures, $EuSnO_2N$ and $YSnO_2N$, are on the convex hull, and $InSnO_2N$, $LaSnO_2N$, and $ScSnO_2N$ are also within 94 meV/atom of the hull, and their hull energies are plotted in Figure 2d. These materials are the most promising result of our search, due to their stability, polarity, and beneficial electronic properties, and we focus on them for the remainder of this paper.

5.4.2 Geometric Ferroelectricity of $ASnO_2N$

Having identified a set of stable and polar tin oxynitrides, we now look at the ferroelectric transition in more detail. We plot the energy difference between the $P6_3/mmc$ and $P6_3mc$ structures in Figure 2e, because this value can be used to approximate the size of the energy barrier to ferroelectric switching. For comparison, isostructural $YMnO_3$ has a calculated barrier of 21 meV/atom,[125] and an experimental ferroelectric transition temperature $T_C = 914$ K.[257] The comparable barrier size of 15-30 meV for *A*=In, Y, Eu, La leads us to predict the polarization of these $ASnO_2N$ to be switchable, but still robust at high temperature. $ScSnO_2N$, at 57 meV/atom, may also be switchable, if the dielectric breakdown field is large. As an additional check, we have calculated the phonon spectra of $YSnO_2N$'s $P6_3/mmc$ and $P6_3mc$ structures; the negative frequencies of $P6_3/mmc$ in Figure 2f indicate that the ferroelectric mode is soft, while the polar $P6_3mc$ has no soft modes and is dynamically stable. Finally, we have calculated the polarization of the 5 stable or metastable tin oxynitrides, which ranges from 7.1 to 16.8 $\mu C/cm^2$, and we show the results in Figure 2g. As polar materials, the ASnO$_2$N family also have relatively large static dielectric constants $\varepsilon \approx 17$, a feature which is beneficial for screening charged defects.

5.4.3 Electronic Properties of ASnO$_2$N

Since the ASnO$_2$N materials are stable and polar, we calculate their band gaps with the more accurate HSE06 functional,[132] to see if they have significant promise for device applications. We find that changing the *A*-site also allows the band gap to be tuned from 1.6 to 3.3 eV, spanning the entire visible spectrum and approaching the gap of $CH_3NH_3PbI_3$, which has a band gap of 1.55 eV,[101] close to the ideal for photovoltaic absorbers. In **Figure 3**a we show the calculated HSE06 band gaps of ASnO$_2$N, compared with several other known perovskite photovoltaic absorbers and *n*-type semiconductors, which serve as benchmarks.

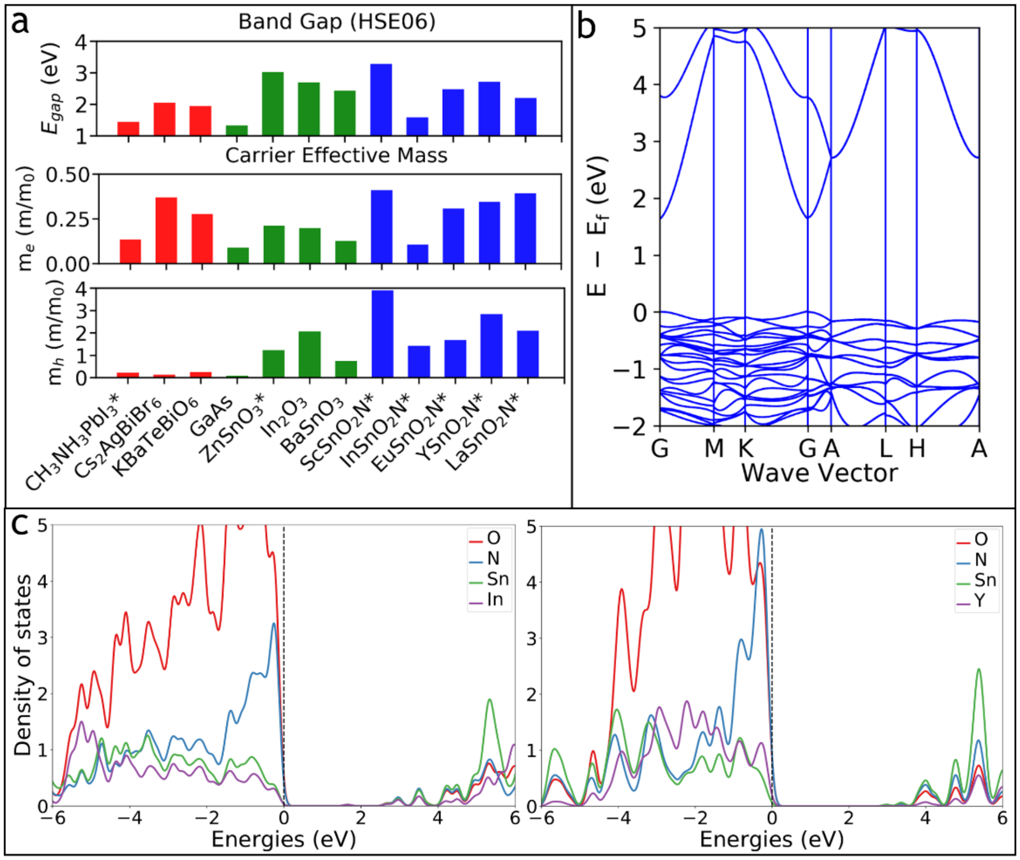

Figure 5.3 Electronic Properties of Novel ASnO$_2$N Semiconductors
a. Top: HSE06 band gap values for *A*SnO$_2$N (red), compared to literature values [111,258-260] for several other semiconductors (blue). Middle: The electron effective masses for the same materials, calculated with the PBE functional.[125] Bottom: the hole effective masses. b. The band structure of InSnO$_2$N, calculated using the HSE06 functional. c. The HSE06 density of electronic states for InSnO$_2$N (left) and YSnO$_2$N (right), projected onto the orbitals of individual atoms.

We also calculate the full electronic band structures, using the inexpensive PBE functional due to computational constraints. Projecting the electronic bands onto atomic orbitals reveals that the VBM of *AB*O$_2$N is composed of both O and N orbitals, as expected. The CBM, meanwhile, is a very dispersive band with contributions from the *s*-orbitals of all four atoms, indicating that the bonding is covalent, with electrons only partially transferred from cation to anion.

InSnO$_2$N has a small band gap of 1.6, compared to the 2.7 eV gap of YSnO$_2$N, and the effect cannot be attributed to polyhedral tilting reducing the degree of covalent orbital overlap.

$YSnO_2N$ has an *A*-site cation 0.10 Å larger than In^{3+}, leading to less tilting, and so by this metric alone $InSnO_2N$ ought to have a larger gap. The small gap of $InSnO_2N$ is instead caused by the high electronegativity of In (1.78) compared with Y (1.22),[11] which increases the strength of the covalent In-O and In-N interactions. Specifically, the In atomic *s*-orbitals lie only 2.15 eV above those of Sn, compared to 5.93 eV for Y,[261] indicating that the conduction band will have a substantial In *s* character as well as Sn *s*. Examination of the projected density of states confirms this. We plot the atom-projected density of states with the HSE06 functional in **Figure 3c**, and investigate further by examining the projections at the VBM and CBM of the PBE band structure. The ratio of atomic contributions to the CBM for $InSnO_2N$ is In 1.43; N 1.19; Sn 1.16; O 1, while for $YSnO_2N$ the CBM is N 4.23; Sn 4.03; O 3.35; Y 1, and so we conclude that the contribution from the low-lying In states lowers the CBM of $InSnO_2N$. $InSnO_2N$ also has a direct gap, compared to the indirect gaps of the other four tin oxynitrides, which are <0.2 eV smaller than their direct gaps. We have confirmed this by re-calculating $InSnO_2N$'s band structure using HSE06, which we show in Figure 3b.

Calculating the band structure also reveals the dispersion of the bands, which is a contributing factor to the mobility of charge carriers. Most photovoltaic or optoelectronic applications require require good charge carrier mobility to reduce non-radiative recombination loss. We continue our investigation of the $ASnO_2N$ oxynitrides by calculating their electron and hole masses, shown in Figure 3a, using the PBE band structure due to the high computational cost of HSE effective mass calculations. All five oxynitrides have very light electrons, with $InSnO_2N$ having $m_e = 0.11m_0$, compared to $BaSnO_3$ at $0.13m_0$ calculated with the same functional. The holes are much heavier as is typical for most metal oxides, with $InSnO_2N$ having holes of 1.43 m_0 mass. The band structure has a dispersive conduction band having substantial Sn *s*-orbital character; the valance band maximum is relatively flat, composed mainly of nonbonding anion *p*-orbitals. Prior studies have also found the same type of band structure for $BaSnO_3$ ($E_{g,\ HSE}$ = 2.43 eV, indirect) and $SrSnO_3$ ($E_{g,\ HSE}$ = 3.50, indirect), although those two perovskite stannates both have experimental gaps >3 eV.[262] The light electrons and high dielectric constant suggest that excitons can be separated easily if $InSnO_2N$ is used as a light absorber. Good exciton separation is important for reducing non-radiative losses due to Auger recombination of electrons and holes.[263] We calculate the exciton binding energy with the Wannier-Mott model[264]

$$E_{bind} = \frac{\frac{m_e^* m_h^*}{m_e^* + m_h^*} R_H}{m_e \varepsilon_{stat}^2} \tag{16}$$

where m_e^* and m_h^* are electron and hole effective masses, R_H is the Rydberg constant, m_e is the free electron mass, and ε_{stat} is the static dielectric constant. We obtain E_{bind} = 4.6 meV from the out-of-plane effective masses and dielectric constant (using in-plane values changes E_{bind} less than a factor of two). This value is much less than the thermal energy ~27 meV at room temperature, so we predict that excitons will separate easily.

While $InSnO_2N$ could be viable in a conventional photovoltaic absorber, its ferroelectricity also enables the bulk photovoltaic effect (BPVE),[265] in which a single uniform layer of ferroelectric can generate a photovoltage. The BPVE proper is the shift current, created in non-centrosymmetric materials when the electron-hole pair are photoexcited with an intrinsic momentum.[109] Other mechanisms, such as separation of charge carriers at domain walls,[266] or the formation of Schottky barriers at absorber/electrode interfaces,[267] also contribute to the total current. BPVE devices facilitate the layering of multiple absorbers with increasing band gaps, in order to make better use of the solar spectrum, because each absorber only requires one layer instead of a full *p*-*n* junction. This strategy was previously employed in the Bi_2FeCrO_6 device which reached 8.1% PCE,[107] in which the band gap was altered by growth conditions. The new tin oxynitrides could be well-suited for a similar approach; for example, $YSnO_2N$ (E_{gap} = 2.7 eV) has only a 1.3% lattice mismatch with isostructural $InSnO_2N$ (E_{gap} = 1.6 eV), which would enable growth of multiple absorber layers.

5.5 Conclusion

In summary, our first-principles search has revealed the stability of a family of $ASnO_2N$ compounds which adopt the polar $LuMnO_3$ structure. By incorporating the *p*-block element Sn into a quaternary oxynitride, we obtain good electronic properties without sacrificing stability or using toxic elements such as Pb. We predict that these new tin oxynitrides have a similar electronic structure to $BaSnO_3$, with a highly dispersive conduction band, and the band gap can be tuned across the entire visible spectrum by varying the *A*-site cation. The combination of light electron mass, ferroelectric polarization, and tunable band gap unlocks several promising applications in visible-light optoelectronics.

Going ahead, there are still several important questions to resolve before these applications can be achieved. While the tin oxynitrides have light electron masses, obtaining good *n*-type conductivity will require the identification of a suitable dopant. Perhaps simply incorporating an excess of Sn during synthesis would lead to Sn^{4+} substitution at the *A*-site, which would avoid the need for a fifth element. Likewise, for many optoelectronic applications, nonradiative recombination lifetime is just as important as charge carrier mobility, and this must be tested through experimental studies. Finally, the amount of photocurrent produced by the BPVE is not yet known for any of these materials. We anticipate that further exploration of the tin oxynitrides will reveal the best ways to use them in devices.

5.6 Computational Methods

Initial screening: We have calculated the energy and electronic ground state properties of 206 $ABO_{3-x}N_x$ compositions in approximately 1,500 total relaxed structures, using the Vienna Ab initio Simulation Package (VASP)[121,163] according to the parameters of the Materials Project.[125] Calculations were set up and run using the Pymatgen and Atomate libraries,[138,268] and the convex hull energies were calculated relative to the other phases in the Materials Project database.

Dielectric and piezoelectric properties. To increase accuracy, we turned off real-space evaluation of projection operators (LREAL = .FALSE) and increased the plane-wave energy cutoff to 600 eV. After relaxing the ground state atomic positions of the 30-atom cell with these settings, we calculated the dielectric and piezoelectric tensors, including both electronic and ionic contributions, using density functional perturbation theory (LEPSILON = TRUE, LPEAD = TRUE) and a k-point grid of 9*5*5 points. Spontaneous polarization was calculated according to the Berry phase method,[143] with the polarization branch between $P6_3/mmc$ and $P6_3cm$ fit using three intermediate images interpolated in ISODISTORT.[269]

Electronic and optical properties: We tested the effect of spin-orbit coupling for heavy elements such as La, but found that it was not required for an accurate band structure, as it created only a very small (<1 meV) splitting of the valence band maximum and conduction band minimum. These states are mainly composed of anion *p* and Sn *s* states, neither of which are expected to show strong spin-orbit coupling. We calculated the HSE06 band gaps using a plane wave cutoff of 500 eV and a 4*4*2 gamma-centered k-points grid, downsampled by a factor of two for the exact exchange potential (NKRED = 2).

Chapter 6: Layered Electrides as Fluoride Intercalation Anodes

This chapter is in preparation for submission as S. Hartman and R. Mishra, “Layered Electrides as Fluoride Intercalation Anodes” (2020).

6.1 Abstract

The fluoride ion is well suited to be the active species of rechargeable batteries, due to its small size, light weight, and high electronegativity. While existing F-ion batteries based on conversion chemistry suffer from rapid electrode degradation with cycling, those based on fluoride intercalation are currently less attractive then cation intercalation battery chemistries due to their low energy densities. Here, using first-principles density-functional-theory calculations, we predict that layered electrides, such as Ca_2N and Y_2C — that have an electron occupying a lattice site — are promising hosts for fluoride intercalation, since their anionic electrons create large interstices. Our calculations indicate that anodes made from layered electrides offer voltage up to –2.86 V vs. La_2CoO_4, capacity > 250 mAh/g, and fast diffusion kinetics with migration barriers as low as 0.15 eV.

6.1 Introduction

Rechargeable batteries enable crucial modern technologies, such as mobile phones, electric cars, and aerial drones, and will be required in even larger numbers for the rapidly growing automotive fleets and grid-scale storage of electricity generated by intermittent renewable sources. Currently, the market is dominated by Li-ion batteries, which shuttle lithium ions between two intercalation electrodes such as graphite and $LiCoO_2$. In these electrodes, the Li ions move into empty spaces in a host material without significantly disrupting the host's structure. While this design has achieved high energy density and adequate cycling stability, the supply risk of lithium and cobalt[112] is predicted to create obstacles for the surge in battery usage. Current, Li-ion batteries also pose safety concerns due to Li dendrite growth and thermal runaway.[270] Therefore, it is desirable to find other high-performance battery chemistries besides Li-ion.

The search for alternative chemistries has primarily been limited to light cations such as Na^+,[271] K^+,[272] Mg^{2+},[273] Zn^{2+},[274] and Al^{3+}.[275] A handful of studies have instead focused on using anions as the active species.[276,277] Amongst the various candidates for active anion batteries, fluoride (F^-) is especially attractive due to its earth-abundance, light weight, high electronegativity, and reasonably fast diffusion in liquid or solid electrolytes.[278-285] But in spite of the success of Li batteries using two intercalation electrodes, most research on fluoride-ion batteries (FiBs) has followed a different path. Most existing fluoride electrodes use conversion reactions,[286,287] pairing metals with metal fluorides, such as:[279]

$$3Sn + 2BiF_3 \rightarrow 3SnF_2 + 2Bi.$$

The theoretical current capacity of conversion electrodes can be very high, such as 669 mAh/g for Ca/CaF_2, compared to 294 mAh/g for $LiCoO_2$. However, these high capacities are difficult to achieve in practice. The phase transformation of the metal to its fluoride during charge/discharge cycles is typically a slow reaction which requires a large overpotential; furthermore, if the resulting volume change is large, the electrode can crumble and degrade during repeated cycling.[288] In addition, the pure metal electrode sometimes dissolves into the electrolyte, further degrading it.[287] These effects are also seen in Li-ion conversion batteries, which have not found commercial success despite extensive research.[289] Therefore, prior experience suggests the value of intercalation FiBs, but no high-capacity fluoride intercalation electrodes have been discovered. The first F^- electrode to be tested was $LaSrMnO_4$/$LaSrMnO_4F_2$,[281] which offered a moderate theoretical capacity of 172 mAh/g, but proved to have very limited reversibility due to destructive side reactions and overpotentials > 1V. La_2CoO_4/La_2CoO_4F later provided improved cycling durability, but at the cost of theoretical capacity (67 mAh/g).[28,286] These electrodes both have relatively little driving force for fluoride intercalation, making them suitable for cathodes, while FiB anodes have not yet been demonstrated.

In this study, we take a new approach to design intercalation FiBs, which is to use the unconventional chemistry of electride crystals to our advantage. These inorganic electrides have interstices occupied by free electrons that act as anions, due to their unusual stoichiometries, which are not charge-balanced in common oxidation states.[290] We use first-principles density-functional-theory (DFT) calculations to show that the electrides can intercalate fluoride stably by replacing the free electron with a F^-. Among the 12 known or predicted electrides which we have examined, we predict Ca_2N and Y_2C as promising candidates for intercalation anodes with theoretical gravimetric capacities ~280 mAh/g, volume change during cycling <15%, voltage < –2.5 V vs. La_2CoO_4, and low kinetic barriers <0.2 eV for fluoride ion transport. These values approach the performance of popular Li-ion electrodes such as $LiCoO_2$, which has theoretical capacity 295 mAh/g, calculated voltage 3.7 V vs. graphite, and migration barriers ~0.3 eV,[125] and Ca_2N in particular is much more earth-abundant than $LiCoO_2$. The excellent performance metrics of Ca_2N and Y_2C, if realized experimentally, will be a major step toward the practical use of FiBs.

6.2 Design Principles for Fluoride Electrodes

6.2.1 Analogy to Li-ion electrodes

First, we consider the crystal structures of Li-intercalation electrodes, to see if the proven design principles can be transferred directly to FiBs. Two of the most successful Li^+ intercalation cathodes, $LiFePO_4$[291] and $LiCoO_2$,[292] are shown in Figures 1 a and b, respectively. They are characterized by anionic polyhedra that are centered on small, highly charged cations (0.65 Å for Fe^{3+}, 0.17 Å for P^{5+}, and 0.53 Å for Co^{4+}). The Li^+ rest in the interstices between these polyhedra. The transition metal, besides providing the redox activity by changing their oxidation state, also serves to hold the crystal together when the Li^+ is absent (in the charged state). Thanks to these framework-preserving cations, $LiCoO_2$ and $LiFePO_4$ have calculated volume changes of only 3% and 7 %,[125] respectively, as Li is removed, promoting durability over many cycles.

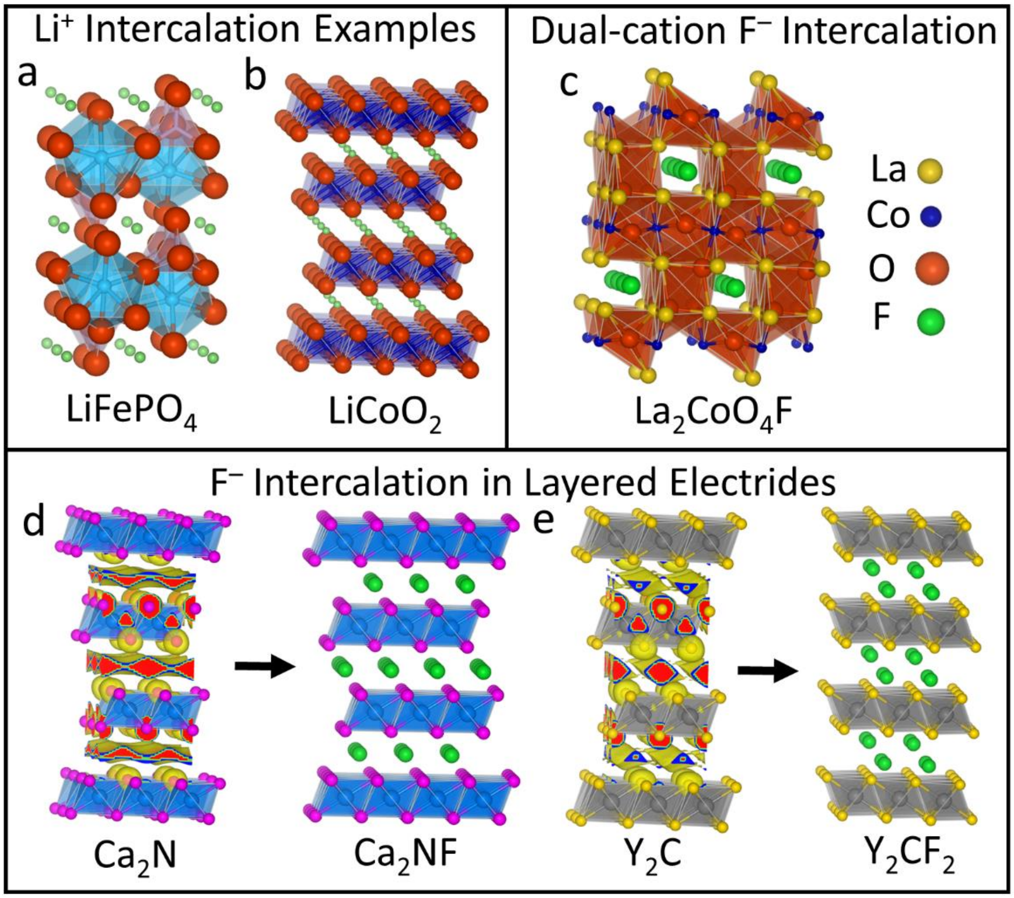

Figure 6.1 Structural principles for intercalation electrode design.
a. The popular Li-ion intercalation electrode $LiFePO_4$, in which Li^+ (green) occupies distorted octahedral sites between PO_4 tetrahedra and FeO_6 distorted octahedra. b. $LiCoO_2$, with Li^+ sitting in octahedral interstices between layers of edge-sharing CoO_6 octahedra. c. The previously known $F^–$ intercalation electrode La_2CoO_4F, with $F^–$ (green) in tetrahedral interstices between strongly distorted La_5CoO octahedra. d. The newly proposed Ca_2NF electrode, with $F^–$ in octahedral interstices between layers of edge-sharing Ca_6N octahedra. The Electron Localization Function[293] of Ca_2N is represented with an isosurface to show the localized electrons between the layers. Ca_2NF's structure is the inverse of $LiCoO_2$'s structure in (b). e. Y_2CF_2, with $F^–$ in tetrahedral interstices between layers of edge-sharing Y_6C octahedra.

Based on these examples, to intercalate $F^–$, we ought to invert the paradigm and have cationic polyhedra centered on some other anion, to maintain the structural integrity in the absence of F ions. However, we immediately notice that anions are generally larger than cations,[38] with $F^–$ having the smallest Shannon radius of 1.33 Å. In addition to making fluoride intercalation more challenging, the large size of anions also restricts the construction of anion-centered polyhedra. Therefore, the best candidates for anion-centered polyhedra are the smaller first-row species such as N^{3-}(1.46 Å), B^{3-}, C^{4-}, and possibly O^{2-} (1.4 Å).[294,295] As for the surrounding cations, they should be large enough to create stable polyhedra with spacious interstices between them. They should also have a low charge to achieve charge balance, since they are more numerous than the central anion even if the polyhedra share many edges and faces. The cation also needs to be light, for good gravimetric capacity, and inexpensive. Finally, it ought to be redox-active, with several stable oxidation states. These constraints are not easily satisfied by a single cation, and indeed all existing fluoride intercalation electrodes combine two or more cation species. Figure 1c shows the most successful to date, La_2CoO_4F,[28,286] which uses larger La^{3+} cations (1.16 Å) to create large tetrahedral interstices in the rock-salt structured LaO layers. We calculate that F^- vacancy-assisted diffusion in La_2CoO_4F has a kinetic barrier of 0.74 eV, which is larger than that of the Li^+ electrodes, but still good enough for reasonable charge/discharge kinetics. The smaller Co^{2+} (0.65 Å) occupies CoO_2 layers which provide the redox activity, as F^- intercalation onto the LaO layers oxidizes Co to 3+. However, the gravimetric capacity is low (67 mAh/g theoretically) because the heavy La is “dead weight” from an electrochemical perspective. This is generally true for similar electrodes such as $MgFeSb_4O_8F$ (39 mAh/g) or $CoFeSb_4O_8F$ (37 mAh/g), [296] although it can be mitigated by using cations lighter than La or Sb, such as Sr (1.26 Å) in $Sr_2TiO_3F_2$ (197 mAh/g), which has been proposed as a FiB anode but not yet tested.[297]

6.2.2 Layered Electrides

We conclude that to keep the electrode light, yet retain large interstitial sites, it should ideally have only one type of cation. Alkali and alkaline earth metals are light, large, inexpensive, and have low charge, satisfying all the constraints except redox activity, so we can expect good results if these metals can be stabilized in oxidation states besides +1 and +2, respectively. Such materials are rare, but a small group of suboxides, subnitrides, and hypocarbides are stable with fewer anions than would be expected by charge balance.[298] One well-studied example is the electride Ca_2N, which from a chemical perspective can be represented as $Ca_2^{2+}N^{3-}e^-$, where e^- is an electron localized at an empty anion site. We show the structure of Ca_2N in Figure 1d. Ca_2N has an inverse $LiCoO_2$ structure, with Ca_6N octahedra instead of CoO_6, and Li replaced by anionic electrons. This suggests the following half-reaction can proceed topochemically, with little volume change:

$$Ca_2N + F^- \rightarrow Ca_2NF + e^-.$$

While Ca_2N is referenced as a possible FiB electrode in a patent application,[299] any related studies remain unpublished, so a detailed theoretical study offers the first opportunity to the understand F^- intercalation properties of Ca_2N.

6.3 Results

6.3.1 Battery Thermodynamics of Ca_2N and Y_2C

To assess the intercalation of Ca_2N with F^- ions, we have calculated the stability of the products and reactants for a variety of fluoride intercalation reactions along with the associated change in voltage and volume using density-functional theory (DFT). For details of these calculations see the section on Computational Methods. We find that both Ca_2N and Ca_2NF, with its structure shown in Figure 1d, are stable against decomposition into known competing phases present in the Materials Project database.[125] The fluoride ion occupies the octahedral site between Ca_2N layers, while the tetrahedral sites, which are twice as many as the octahedral sites, are unoccupied. Placing fluoride into the tetrahedral site costs 0.34 eV more than the octahedral site. Upon geometry optimization, we find that Ca_2NF retains the same rhombohedral $R\bar{3}m$ phase as Ca_2N. For this structure, we can calculate its gravimetric capacity to be 285 mAh per gram of Ca_2N according to:

$$\frac{1\,\text{mol Ca}_2\text{N}}{94\,\text{g Ca}_2\text{N}}\times\frac{1\,\text{mol e}^-}{1\,\text{mol Ca}_2\text{N}}\times\frac{96485\,\text{A}\times\text{s}}{1\,\text{mol e}^-}\times\frac{1000\,\text{mA}}{1\,\text{A}}\times\frac{1\,\text{h}}{3600\,\text{s}} \quad [17]$$

We note that while Ca_2NCl and Ca_2NBr are experimentally reported to exist in the $R\bar{3}m$ phase,[71,300] Ca_2NF has only been made in the $I4_1/amd$ phase,[301] which we find is metastable with respect to the $R\bar{3}m$ phase by 5 meV/atom. We also expect that low-temperature fluorination, which has emerged as a successful strategy to produce metastable fluoride structures, should yield $R\bar{3}m$ Ca_2NF from $R\bar{3}m$ Ca_2N. The $R\bar{3}m$ phase's volume shrinks 13% during fluorination, and the electromotive force is –2.86 V vs. La_2CoO_4/La_2CoO_4F, calculated with:

$$\frac{E_{Ca_2NF} + E_{La_2CoO_4} - E_{Ca_2N} - E_{La_2CoO_4F}}{1} \quad [18]$$

–2.86 V is the same calculated potential as the Li/LiF half-reaction, indicating that Ca_2N is highly electropositive, consistent with its experimentally known sensitivity to air and moisture.[302] Ca_2NF can be further fluorinated to Ca_2NF_2 at –0.78 V vs. La_2CoO_4/La_2CoO_4F, but we do not include this in its theoretical capacity, since it is not clear if the anion-redox capacity is accessible without degrading the electrode. The Ca_2NF_2 phase is 237 meV/atom above the Materials Project convex hull, excluding species such as CaN_6 which are poorly described by DFT,[110] and it might decompose by nitrogen gas evolution to produce Ca_2NF and CaF_2.

Another electride isostructural to Ca_2N, Y_2C [303] is also a promising candidate for FiB anodes. Y_2C, as shown in Figure 1e, can be represented as $Y_2^{3+}N^{3-}2e^-$ with $2e^-$ nominally residing at the octahedral site. Recently, Druffel et al. reported the formation of Y_2CF_2 using a high-temperature solid-state reaction of Y, YF_3, and graphite.[304] F^- ions are observed to occupy the tetrahedral sites in Y_2CF_2, and the Y_2C layers re-stack from their original *ABC* stacking pattern to an AAA stacking in Y_2CF_2 with space group $P\overline{3}m1$, as shown in Figure 1e. As a consequence of the AAA stacking, we find that Y_2CF_2 expands by 8% in volume relative to Y_2C, rather than shrinking. We also calculate its voltage to be –2.56 V vs. La_2CoO_4/La_2CoO_4F, with a gravimetric capacity of 282 mAh/g.

The Y_2CF phase, with F^- in octahedral sites, is unstable by 91 meV/atom with respect to Y_2C and Y_2CF_2, indicating that Y_2C is likely to fluorinate in a one-step process without staging. Further evidence for a one-step reaction is provided by the formation energy of the neutral F^- vacancy, which we calculate to be 0.14 eV at the chemical potential defined by the Y_2C/Y_2CF_2 equilibrium. Creating two adjacent fluoride vacancies costs 0.46 eV. Neglecting entropy, it is easier to defluorinate Y_2CF_2 all at once, than to remove one or two F^- at a time. Most Li-ion batteries discharge by stages because the electrostatic repulsion between Li^+ gradually reduces the driving force to insert additional Li^+,[305] but the empty F^- sites of the electrides can still be occupied by a negatively charged electron, so electrostatically it makes little difference whether the site is filled or empty.

Based on these thermodynamic calculations, we expect the layered electrides to have good energy storage capacity, but the diffusion kinetics are also important. To achieve high power density, a battery electrode must conduct the active ion rapidly. Since the layered structures of

Ca_2NF and Y_2CF_2 match $LiCoO_2$ so closely, it is reasonable to expect them to have fast two-dimensional ion transport kinetics, which we calculate using the climbing-image nudged elastic-band (NEB) technique.[306] We consider three mechanisms: vacancy-assisted diffusion, direct interstitial diffusion, and interstitialcy (kick-out) diffusion. The total activation energy is the formation energy of the relevant electrically neutral defect, plus the kinetic barrier height, and we consider both fluorine-rich and fluorine-poor conditions when calculating the formation energy of the defects. In Ca_2NF, the dominant mechanism switches from vacancy to interstitialcy diffusion when the fluoride chemical potential is increased, as illustrated in Figure 2a and 2b. By contrast, Y_2CF_2 favors vacancy diffusion under any stable fluoride potential, since the F^- vacancy has low formation and migration energies. The intrinsically doped activation energy of Y_2CF_2, 0.3 eV under F-poor chemical potentials, compares well with the 0.3 eV activation energy found experimentally and theoretically for $LiCoO_2$.[307] Due to the low kinetic barrier heights <0.2 eV, both Y_2CF_2 and Ca_2NF can have greatly improved diffusion if extrinsically doped to increase F^- defect concentration. For example, $Ca_{2-x}Y_xNF_{1+x}$ would most likely have fluoride interstitials at the tetrahedral site to balance the greater charge of Y^{3+}.

6.3.2 Fluoride Diffusion Kinetics of Ca_2NF and Y_2CF_2

Based on these thermodynamic calculations, we expect the layered electrides to have good energy storage capacity, but the diffusion kinetics are also important. To achieve high power density, a battery electrode must conduct the active ion rapidly. Since the layered structures of Ca_2NF and Y_2CF_2 match $LiCoO_2$ so closely, it is reasonable to expect them to have fast two-dimensional ion transport kinetics, which we calculate using the climbing-image nudged elastic-band (NEB) technique.[306] We consider three mechanisms: vacancy-assisted diffusion, direct interstitial diffusion, and interstitialcy (kick-out) diffusion. The total activation energy is the

formation energy of the relevant electrically neutral defect, plus the kinetic barrier height, and we consider both fluorine-rich and fluorine-poor conditions when calculating the formation energy of the defects. In Ca_2NF, the dominant mechanism switches from vacancy to interstitialcy diffusion when the fluoride chemical potential is increased, as illustrated in Figure 2a and 2b. By contrast, Y_2CF_2 favors vacancy diffusion under any stable fluoride potential, since the F^- vacancy has low formation (0.14-0.55 eV) and migration (0.16 eV) energies. The intrinsically doped activation energy of Y_2CF_2, 0.3 eV under F-poor chemical potentials, compares well with the 0.3 eV activation energy found experimentally and theoretically for $LiCoO_2$.[307] Due to the low kinetic barrier heights <0.2 eV, both Y_2CF_2 and Ca_2NF can have greatly improved diffusion if extrinsically doped to increase F^- defect concentration. For example, $Ca_{2-x}Y_xNF_{1+x}$ would most likely have fluoride interstitials at the tetrahedral site to balance the greater charge of Y^{3+}.

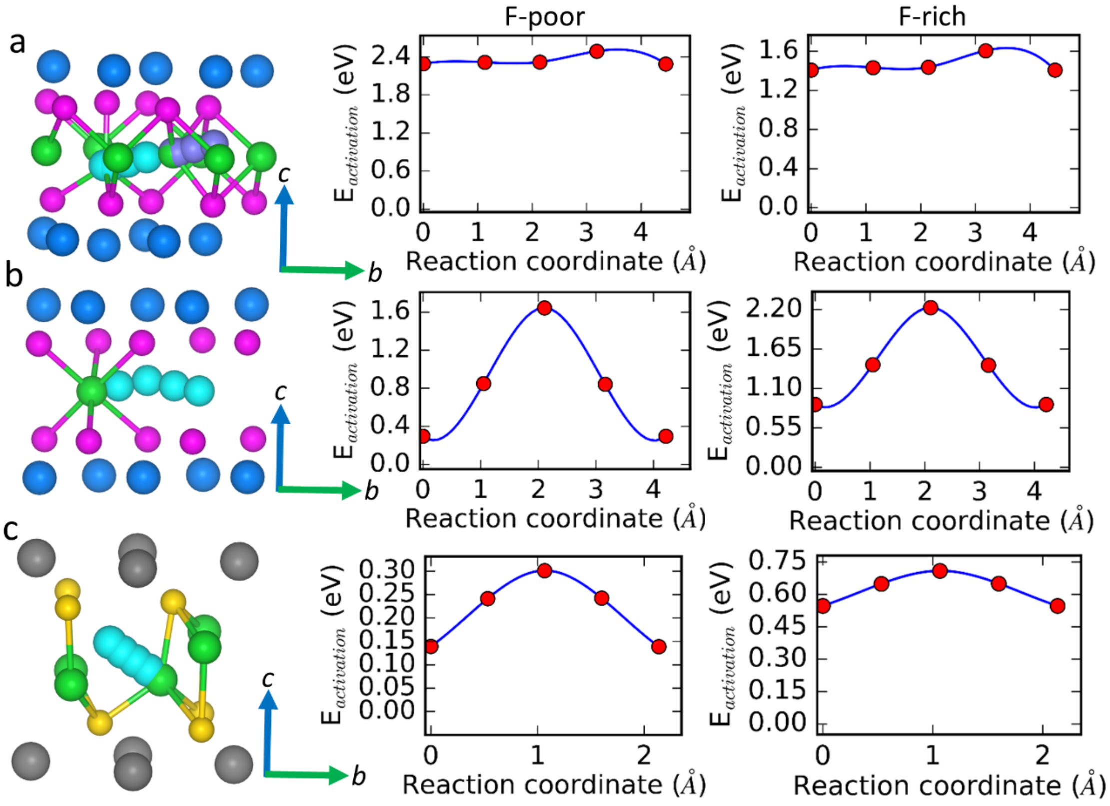

Figure 6.2 NEB study of F^- diffusion kinetics.
a. Interstitialcy mechanism in Ca_2NF, favorable under fluorine-rich conditions. A tetrahedral F^- interstitial (light blue) displaces an octahedral F^- (purple), which moves to a tetrahedral site on the opposite side as the original. The activation energy, equal to the defect formation energy plus the diffusion barrier, is shown for fluorine-poor and fluorine-rich chemical potentials. b. Vacancy mechanism in Ca_2NF, favorable under fluorine-poor conditions. An octahedral F^- moves into another octahedral site. c. Vacancy mechanism in Y_2CF_2, favorable through the whole chemical potential range. A tetrahedral F^- moves to an adjacent tetrahedral site.

6.4 Discussion

While Ca_2N and Y_2C are the most promising electrides for use in FIBs, we have also calculated the F^- intercalation properties of several other electrides, including LaSi, SrSi, Ba_3N, and Ba_2NaO,[308-310] for comparison. In addition, we have calculated the stability and capacity of several known MXenes,[295] which are structurally related to the layered electrides, although their chemical properties are different. We compare the theoretical performance of these different structural families in Figure 3, with popular Li-ion electrodes shown as a reference. Ca_2N and Y_2C have calculated performances closest to that of their structural analogue $LiCoO_2$, while the other electrides are less stable. While the MXenes have high gravimetric capacity - up to 497 mAh/g for Ti_2C - due to their light weight, they also have low voltage and experience large volume changes. This illustrates the advantage of the electride chemistry for FIBs; the free electrons have a very low work function ~2.5 eV,[311] the same as Li metal.[312] Because electrides give up electrons easily, they have a higher voltage vs. the cathode, while they also act in combination with the large Ca^{2+} and Y^{3+} cations to maintain large interstices even in the unfluorinated state.

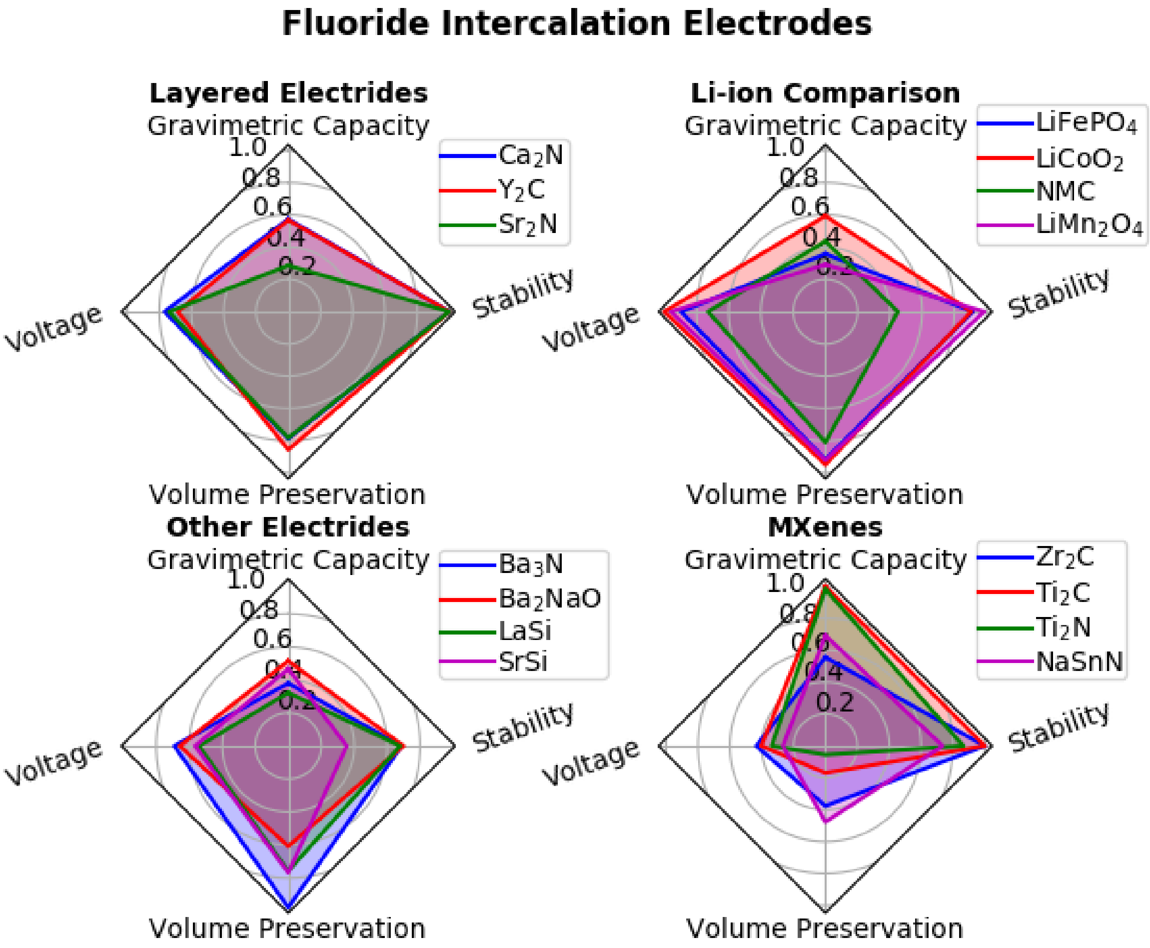

Figure 6.3 Comparison of structural families for intercalation electrodes.

Gravimetric capacity and voltage are normalized with respect to the highest score in each category. The voltage is the average voltage for the complete reaction with La_2CoO_4F or LiC_6, not accounting for any steps in the voltage profile. Stability is calculated as $(0.2 - E_{hull})/0.2$, where E_{hull} is the energy above the convex hull, in eV/atom, of whichever electrode state (charged or discharged) is less stable. Likewise, volume preservation is $(0.6 - \Delta \text{ vol.})/0.6$, where Δ vol. is the volume change of the intercalated phase with respect to the de-intercalated phase. Calculated data for these and other electrodes are in Supporting Information.

Our calculations suggest that Ca_2N and Y_2C can perform very well as FiB anodes. Going forward, there are several other FiB components which require improvement for these anodes to be used at their full capability. The most important target for further research is the voltage stability window of the electrolyte and conductive additive. Ca_2N is likely to form a solid-electrolyte interphase (SEI) in contact with solid fluoride electrodes such as $La_{1-x}Ba_xF_{3-x}$ (LBF), since Li/LiF has the same potential of –2.86 V and is known to reduce LBF,[50] while Y_2C is right on the edge of the stability window. At the other end of the window, La_2CoO_4 is the highest-voltage practical cathode, at 2.86 V vs. Ca_2N/Ca_2NF. Higher-voltage cathodes are known, but at those voltages the commonly used conductive additive, carbon black, reacts irreversibly with F^-.[13, 31, 50] The carbon fluorination may be avoided in the future through the introduction of improved conductors such as SnO_2 or carbon nanotubes.[20] In order to compete with Li-ion batteries, the accessible voltage range must be expanded to >3 V, and intercalation cathodes with higher capacities than La_2CoO_4 or $LaSrMnO_4$ are required.

6.5 Conclusion

In conclusion, we have calculated the properties of different FiB intercalation electrodes, and find that Ca_2N and Y_2C can offer an excellent combination of energy density, power density, and cycling stability. Their useful properties are due to the unique chemistry of layered electrides, which have free anionic electrons occupying vacant anion sites in the defluorinated state. Both materials intercalate F^- with very low kinetic barriers for F^- diffusion, and less volume change than most conversion electrodes, which is ideal for fast and reversible charge/discharge cycles. We expect that these new anodes will significantly advance FiBs' energy storage capability.

6.6 Computational Methods

We performed all DFT calculations using the VASP software,[51-52] and chose our calculation parameters to be compatible with the Materials Project database.[24, 53] Certain calculations could not be converged using the tetrahedron method for electronic smearing, so these were completed using Gaussian smearing with a small SIGMA of 0.01, to minimize the discrepancy compared to the tetrahedron method. To maintain compatibility with the Materials Project, we did not include van der Waals corrections (see Supporting Information for tests of the effects of vdW corrections). All gravimetric capacities were calculated with respect to the mass of the defluorinated or delithiated state, and the reported voltage is the electromotive force driving the complete reaction, which does not include the "steps" seen in many experimental discharge curves due to intermediate phases. The initial locations of fluoride atoms were selected manually, a procedure which is unambiguous for the layered electrides with their clearly defined octahedral and tetrahedral sites.

Summary

This dissertation has used first-principles DFT to explore some of the ways that anion engineering can be used to improve functional ceramics. The substitution of existing anions with others, or the addition of more anions, allows a fine tuning of the materials' properties for a specific application. We have illustrated four specific areas in which anion engineering offers the prospect of improvement.

In the first study, we looked at the use of fluorination to control the charge states of transition metals in complex oxide multiferroics. The hybrid improper ferroelectric mechanism offers the ability to reconcile the conflicting constraints of ferroelectricity and magnetism, since conventional ferroelectricity requires a d^0 transition metal but robust magnetism requires unpaired *d* electrons, but the hybrid improper ferroelectricity is generated by the larger *A*-site cation and the *B*-sites magnetism is not affected. However, the constraint of charge balance remains in force for oxides, and the two +3 cations required for a stable $AA'\mathrm{Fe_2O_6}$ perovskite limit the size of the polarization. We found that replacing oxygen with fluorine allowed the use of *A*-sites with different charges, such as $\mathrm{YCaFe_2O_5F}$, without disrupting the $\mathrm{Fe^{3+}}$ oxidation state needed for robust antiferromagnetism. By searching for the ground state structure across a range of cation compositions and octahedral tilt patterns, we obtained a family of $AA'\mathrm{Fe_2O_5F}$ with stable ferroelectric polarization as high as 13 μC/cm^2. Although the largest *A'* cations led to the largest polarization, they also de-stabilized the polar phase with $a^-a^-c^+$ tilting in favor of a non-polar $a^0b^-c^-$ phase. Since the antiferromagnetic state was stabilized by >100 meV/Fe, which is slightly greater than the equivalent values for chemically related room-temperature antiferromagnets, we predicted that the resulting multiferroics show robust magnetism at room temperature. Replacing Fe with Mn, we found that Mn is more stable in the polar phase than Fe due to the Jahn-Teller ordering of Mn's orbitals, which matches the reduced symmetry of the MnO_5F octahedron.

In the second study, we considered apical oxygen vacancies in the anion sublattice of the high-temperature superconductor $YBa_2Cu_3O_{7-x}$ (YBCO). Nearly all previous research on oxygen vacancies in this technologically important material has focused on the chain oxygen position, which is known to form stoichiometric amounts of vacancies as YBCO is deoxygenated. However, a few early reports had suggested that up to 0.1 vacancies per formula unit formed at the apical oxygen position, and we confirmed this using a combination of first-principles calculations and STEM imaging. We found that the apical vacancies were stable in small concentrations <0.1/f.u., a regime which is important for device applications because it is the doping level which maximizes the critical temperature. Apical vacancies were not stable at high concentrations because they repelled each other, unlike chain vacancies which attracted each other. STEM imaging confirmed that the vacancies were located in the apical position, and the observed crystal distortion around the vacancies matched the predicted distortions from DFT. We analyzed the electronic effects of the apical vacancies using DFT and STEM, finding that the excess electrons were primarily located on the adjacent planar Cu, with possible implications for the material's high-temperature superconductivity. In a follow-up study, we observed that the apical vacancies were most common near Y124 intergrowths, which create up to 2% compressive strain in the adjacent unit cells. DFT calculations indicated that the strain makes the apical vacancies ~50 meV more favorable than the chain oxygen vacancies, providing a mechanism to explain their high concentration near intergrowths.

Our third study looked at oxynitrides with cations from the *p*-block of the periodic table, aiming to create new semiconductors with the stability of oxides, but smaller band gaps and better charge carrier mobility thanks to the covalency of metal-nitride bonding. This strategy was inspired by the success of the lead halide perovskites such as $CH_3NH_3PbI_3$, which have excellent carrier mobility and defect tolerance driven in part by the presence of delocalized *s*-orbitals at the band edges. We searched a variety of structural prototypes in the ABO_2N and $ABON_2$ composition space, and identified a new family of $ASnO_2N$ semiconductors, with at least 2 materials on the convex hull of stability, and three others within 94 meV/atom of the hull. The small size of the *A*-site cation induced a ferroelectric transition which created a polarization of up to 17 $\mu C/cm^2$, and changing the *A*-site also allowed the band gap to be tuned between 1.6 and 3.3 eV. As intended, the *s*-orbitals of Sn^{4+} were located at the conduction band minimum, creating a dispersive band with effective mass as low as 0.12 m_0. The combination of electric polarity, a small and tunable band gap, and light electron mass offers significant promise for photovoltaics or optoelectronics.

Finally, we have investigated battery electrodes which use the fluoride anion as the electrochemically active species. While F^- is a promising competitor to Li^+ due to its light weight (18.998 amu), earth abundance, and high electronegativity, existing fluoride-ion batteries have not achieved high reversible capacities >200 mAh/g because most of them undergo a large volume and structure change through conversion-type reactions, while the few existing F^- intercalation electrodes must be heavy to satisfy basic structural constraints. We have studied the layered electrides as a promising new family for fluoride intercalation anodes, since the free anionic electrons create large sites suitable for the addition of fluoride. We found that two of the known layered electrides, Ca_2N and Y_2C, offered gravimetric current capacities >280 mAh/g. Because the calculated volume changes during cycling were <15% and both charged and discharged structures were on the convex hull, we predicted that the two electrodes would exhibit good reversibility over many cycles. In addition, the F^- migration barriers < 0.3 eV of the two electrides indicated that they should have quick charge/discharge performance. We conclude that Ca_2N and Y_2C are promising anodes for a fluoride-ion battery which can compete with existing Li-ion technology.

References

[1] G. Wang, Y. Yang, D. Han, and Y. Li, Nano Today **13**, 23 (2017).

[2] G. Wang, H. Wang, Y. Ling, Y. Tang, X. Yang, R. C. Fitzmorris, C. Wang, J. Z. Zhang, and Y. Li, Nano Lett. **11**, 3026 (2011).

[3] A. Roos, F. C. M. van de Pol, R. Keim, and J. Schoonman, Solid State Ionics **13**, 191 (1984).

[4] J. K. Harada, N. Charles, K. R. Poeppelmeier, and J. M. Rondinelli, Adv. Mater. **0**, 1805295 (2019).

[5] Y. Kobayashi, T. Yoshihiro, and H. Kageyama, Annual Review of Materials Research (2018).

[6] O. Clemens and R. Slater Peter, in *Reviews in Inorganic Chemistry*2013), p. 105.

[7] Y. Kobayashi, T. Yoshihiro, and H. Kageyama, Annual Review of Materials Research **48** (2018).

[8] H. Kageyama, K. Hayashi, K. Maeda, J. P. Attfield, Z. Hiroi, J. M. Rondinelli, and K. R. Poeppelmeier, Nature Communications **9** (2018).

[9] J. G. Marignac, Comptes Rendus de l' Academie des Sciences (1863).

[10] W. K. V. Haagen and E. F. Smith, J. Am. Chem. Soc. **33**, 1504 (1911).

[11] L. Pauling, J. Am. Chem. Soc. **54**, 3570 (1932).

[12] J. L. Kissick, C. Greaves, P. P. Edwards, V. M. Cherkashenko, E. Z. Kurmaev, S. Bartkowski, and M. Neumann, Physical Review B **56**, 2831 (1997).

[13] E. J. Moon, Y. Xie, E. D. Laird, D. J. Keavney, C. Y. Li, and S. J. May, J. Am. Chem. Soc. **136**, 2224 (2014).

[14] T. Onozuka *et al.*, ACS Appl Mater Interfaces **9**, 10882 (2017).

[15] M. Sturza, H. Kabbour, S. Daviero-Minaud, D. Filimonov, K. Pokholok, N. Tiercelin, F. Porcher, L. Aldon, and O. Mentré, J. Am. Chem. Soc. **133**, 10901 (2011).

[16] J. B. Goodenough, J. Phys. Chem. Solids **6**, 287 (1958).

[17] R. Zhang, M. S. Senn, and M. A. Hayward, Chem. Mater. **28**, 8399 (2016).

[18] J. K. Harada, K. R. Poeppelmeier, and J. M. Rondinelli, Inorg. Chem. (2019).

[19] N. Charles, R. J. Saballos, and J. M. Rondinelli, Chem. Mater. (2018).

[20] A. M. Fry and P. M. Woodward, Crystal Growth & Design **13**, 5404 (2013).

[21] A. K. Mishra, M. R. Marvel, K. R. Poeppelmeier, and U. V. Waghmare, Crystal Growth & Design **14**, 131 (2014).

[22] C. Chen, Y. Wu, and R. Li, Int. Rev. Phys. Chem. **8**, 65 (1989).

[23] M. R. Marvel, J. Lesage, J. Baek, P. S. Halasyamani, C. L. Stern, and K. R. Poeppelmeier, J. Am. Chem. Soc. **129**, 13963 (2007).

[24] P. A. Maggard, T. S. Nault, C. L. Stern, and K. R. Poeppelmeier, J. Solid State Chem. **175**, 27 (2003).

[25] R. L. Withers, F. J. Brink, Y. Liu, and L. Norén, Polyhedron **26**, 290 (2007).

[26] R. A. F. Pinlac, C. L. Stern, and K. R. Poeppelmeier, Crystals **1** (2011).

[27] Y. Hinuma, H. Moriwake, Y.-R. Zhang, T. Motohashi, S. Kikkawa, and I. Tanaka, Chem. Mater. **24**, 4343 (2012).

[28] M. A. Nowroozi, S. Ivlev, J. Rohrer, and O. Clemens, Journal of Materials Chemistry A **6**, 4658 (2018).

[29] O. Clemens, C. Reitz, R. Witte, R. Kruk, and R. I. Smith, J. Solid State Chem. **243**, 31 (2016).

[30] K. Tsukasa, C. Akira, K. Hideyuki, K. Hiroshi, and H. Tetsuya, Applied Physics Express **9**, 025801 (2016).

[31] L. Pauling, J. Am. Chem. Soc. **51**, 1010 (1929).

[32] I. Brown, Acta Crystallographica Section B **48**, 553 (1992).

[33] A. Fuertes, Inorg. Chem. **45**, 9640 (2006).

[34] M. Kaneko, M. Fujii, T. Hisatomi, K. Yamashita, and K. Domen, Journal of Energy Chemistry (2019).

[35] H. Jiang and X. Xu, Journal of Materials Chemistry A (2019).

[36] Y. Kurauchi, T. Katayama, A. Chikamatsu, and T. Hasegawa, The Journal of Physical Chemistry C (2019).

[37] M. A. Hayward, Semicond. Sci. Technol. **29**, 064010 (2014).

[38] R. Shannon, Acta Crystallographica Section A **32**, 751 (1976).

[39] P. Anitha Sukkurji, A. Molinari, C. Reitz, R. Witte, C. Kübel, V. Chakravadhanula, R. Kruk, and O. Clemens, Materials **11** (2018).

[40] C. K. Blakely, J. D. Davis, S. R. Bruno, S. K. Kraemer, M. Zhu, X. Ke, W. Bi, E. E. Alp, and V. V. Poltavets, J. Fluorine Chem. **159**, 8 (2014).

[41] K. Wissel *et al.*, Inorg. Chem. (2018).

[42] O. Clemens, M. Kuhn, and R. Haberkorn, J. Solid State Chem. **184**, 2870 (2011).

[43] O. Clemens, R. Haberkorn, P. R. Slater, and H. P. Beck, Solid State Sci **12**, 1455 (2010).

[44] K. H. Moon, M. Avdeev, and Y.-I. Kim, J. Solid State Chem. **254**, 1 (2017).

[45] C. M. Fang, G. A. de Wijs, E. Orhan, G. de With, R. A. de Groot, H. T. Hintzen, and R. Marchand, J. Phys. Chem. Solids **64**, 281 (2003).

[46] S. K. Suram, S. W. Fackler, L. Zhou, A. T. N'Diaye, W. S. Drisdell, J. Yano, and J. M. Gregoire, ACS Combinatorial Science **20**, 26 (2018).

[47] H. B. Gray, *Electrons and chemical bonding* (W. A. Benjamin, 1964).

[48] Y. Liu, W. Wang, X. Xu, J.-P. Marcel Veder, and Z. Shao, Journal of Materials Chemistry A (2019).

[49] S. Wei and X. Xu, Applied Catalysis B: Environmental **228**, 10 (2018).

[50] A. P. Black, H. Suzuki, M. Higashi, C. Frontera, C. Ritter, C. De, A. Sundaresan, R. Abe, and A. Fuertes, Chem. Commun. **54**, 1525 (2018).

[51] K. Sawada and T. Nakajima, APL Materials **6**, 101103 (2018).

[52] A. Kubo, G. Giorgi, and K. Yamashita, Chem. Mater. **29**, 539 (2017).

[53] X. Wang, Z. Li, and Z. Zou, PCCP **17**, 19631 (2015).

[54] Y. Wu, P. Lazic, G. Hautier, K. Persson, and G. Ceder, Energy & Environmental Science **6**, 157 (2013).

[55] D. Maiti, A. J. Meier, J. Cairns, S. Ramani, K. Martinet, J. N. Kuhn, and V. R. Bhethanabotla, Dalton Transactions (2019).

[56] J. P. Attfield, Crystal Growth & Design **13**, 4623 (2013).

[57] M. Yang, J. Oró-Solé, J. A. Rodgers, A. B. Jorge, A. Fuertes, and J. P. Attfield, Nat Chem **3**, 47 (2011).

[58] A. Fuertes, J. Mater. Chem. **22**, 3293 (2012).

[59] K. Page, M. W. Stoltzfus, Y.-I. Kim, T. Proffen, P. M. Woodward, A. K. Cheetham, and R. Seshadri, Chem. Mater. **19**, 4037 (2007).

[60] L. Clark, J. Oró-Solé, K. S. Knight, A. Fuertes, and J. P. Attfield, Chem. Mater. **25**, 5004 (2013).

[61] D. Oka *et al.*, ACS Nano (2017).

[62] S. Ninova and U. Aschauer, Journal of Materials Chemistry A **5**, 11040 (2017).

[63] H. Johnston, A. P. Black, P. Kayser, J. Oro-Sole, D. A. Keen, A. Fuertes, and P. Attfield, Chem. Commun. (2018).

[64] P. J. Camp, A. Fuertes, and J. P. Attfield, J. Am. Chem. Soc. **134**, 6762 (2012).

[65] R. E. Alonso, M. A. Taylor, A. V. Gil Rebaza, M. Cappelletti, and V. Fernández, Boletín de la Sociedad Española de Cerámica y Vidrio (2017).

[66] M. A. Al-Azzawi, Youngstown State University, 2016.

[67] M. A. Brogan, R. W. Hughes, R. I. Smith, and D. H. Gregory, J. Solid State Chem. **185**, 213 (2012).

[68] M. A. Brogan, R. W. Hughes, R. I. Smith, and D. H. Gregory, Dalton Transactions **39**, 7153 (2010).

[69] A. S. Bailey, R. W. Hughes, P. Hubberstey, C. Ritter, R. I. Smith, and D. H. Gregory, Inorganic Chemistry **50**, 9545 (2011).

[70] A. Bowman, R. I. Smith, and D. H. Gregory, Journal of Solid State Chemistry **178**, 1807 (2005).

[71] A. Bowman, P. V. Mason, and D. H. Gregory, Chemical Communications, 1650 (2001).

[72] H. Demiryont, (Google Patents, 2010).

[73] S. Yamanaka, Annual Review of Materials Science **30**, 53 (2000).

[74] D. A. Headspith, E. Sullivan, C. Greaves, and M. G. Francesconi, Dalton Transactions, 9273 (2009).

[75] N. Vonrüti and U. Aschauer, Journal of Materials Chemistry A **7**, 15741 (2019).

[76] M. Sheeraz *et al.*, Physical Review Materials **3**, 084405 (2019).

[77] I. E. Castelli, D. D. Landis, K. S. Thygesen, S. Dahl, I. Chorkendorff, T. F. Jaramillo, and K. W. Jacobsen, Energy & Environmental Science **5**, 9034 (2012).

[78] Q. Wang *et al.*, Nature Materials **18**, 827 (2019).

[79] M. Valldor, Inorganics **4** (2016).

[80] D. I. Khomskii, J. Magn. Magn. Mater. **306**, 1 (2006).

[81] M. Fiebig, T. Lottermoser, D. Meier, and M. Trassin, Nature Reviews Materials **1**, 16046 (2016).

[82] J. F. Scott, Science **315**, 954 (2007).

[83] A. S. Teja and P.-Y. Koh, Prog. Cryst. Growth Charact. Mater. **55**, 22 (2009).

[84] M. Cesaria, A. P. Caricato, G. Maruccio, and M. Martino, Journal of Physics: Conference Series **292**, 012003 (2011).

[85] A. Filippetti and N. A. Hill, Phys. Rev. B **65**, 195120 (2002).

[86] N. A. Hill, The Journal of Physical Chemistry B **104**, 6694 (2000).

[87] S. T. Hartman, S. B. Cho, and R. Mishra, Inorg. Chem. (2018).

[88] J. Bardeen, L. N. Cooper, and J. R. Schrieffer, Physical Review **108**, 1175 (1957).

[89] H. K. Onnes, Comm. Leiden **122**, 2 (1911).

[90] G.-i. Oya and E. J. Saur, Journal of Low Temperature Physics **34**, 569 (1979).

[91] M. K. Wu, J. R. Ashburn, C. J. Torng, P. H. Hor, R. L. Meng, L. Gao, Z. J. Huang, Y. Q. Wang, and C. W. Chu, Physical Review Letters **58**, 908 (1987).

[92] D. H. Ha, S. Byon, and K. W. Lee, Physica C: Superconductivity **340**, 243 (2000).

[93] R. Liang, D. A. Bonn, and W. N. Hardy, Physical Review B **73**, 180505 (2006).

[94] E. F. Talantsev, N. M. Strickland, S. C. Wimbush, J. G. Storey, J. L. Tallon, and N. J. Long, Applied Physics Letters **104**, 242601 (2014).

[95] R. J. Cava, A. W. Hewat, E. A. Hewat, B. Batlogg, M. Marezio, K. M. Rabe, J. J. Krajewski, W. F. Peck, and L. W. Rupp, Physica C: Superconductivity **165**, 419 (1990).

[96] J. D. Jorgensen, S. Pei, P. Lightfoot, H. Shi, A. P. Paulikas, and B. W. Veal, Physica C: Superconductivity **167**, 571 (1990).

[97] J. C. Cheang Wong, C. Ortega, J. Siejka, I. Trimaille, A. Sacuto, L. M. Mercandalli, and F. Mayca, Journal of Alloys and Compounds **195**, 675 (1993).

[98] A. P. Shapovalov, M. B. Yu, A. I. Ruban, G. G. Gridneva, V. S. Melnikov, and N. P. Pshentsova, Superconductor Science and Technology **5**, 283 (1992).

[99] S. H. Pan, E. W. Hudson, and J. C. Davis, Review of Scientific Instruments **70**, 1459 (1999).

[100] S. T. Hartman, B. Mundet, J.-C. Idrobo, X. Obradors, T. Puig, J. Gázquez, and R. Mishra, Physical Review Materials **3**, 114806 (2019).

[101] A. M. A. Leguy *et al.*, Nanoscale **8**, 6317 (2016).

[102] J. Kim, C.-H. Chung, and K.-H. Hong, Physical Chemistry Chemical Physics **18**, 27143 (2016).

[103] M. H. Du, Journal of Materials Chemistry A **2**, 9091 (2014).

[104] A. Walsh, The Journal of Physical Chemistry C **119**, 5755 (2015).

[105] L. M. Garten *et al.*, Science Advances **5**, eaas9311 (2019).

[106] D. Yang, J. Lv, X. Zhao, Q. Xu, Y. Fu, Y. Zhan, A. Zunger, and L. Zhang, Chemistry of Materials **29**, 524 (2017).

[107] R. Nechache, C. Harnagea, S. Li, L. Cardenas, W. Huang, J. Chakrabartty, and F. Rosei, Nature Photonics **9**, 61 (2014).

[108] N.-K. Kim *et al.*, Scientific Reports **7**, 4645 (2017).

[109] L. Z. Tan, F. Zheng, S. M. Young, F. Wang, S. Liu, and A. M. Rappe, npj Computational Materials **2**, 16026 (2016).

[110] W. Sun, S. T. Dacek, S. P. Ong, G. Hautier, A. Jain, W. D. Richards, A. C. Gamst, K. A. Persson, and G. Ceder, Science Advances **2** (2016).

[111] Y. Mi, H. Odaka, and S. Iwata, Japanese Journal of Applied Physics **38**, 3453 (1999).

[112] C. Helbig, A. M. Bradshaw, L. Wietschel, A. Thorenz, and A. Tuma, Journal of Cleaner Production **172**, 274 (2018).

[113] E. Schrödinger, Physical Review **28**, 1049 (1926).

[114] P. A. M. Dirac and R. H. Fowler, Proceedings of the Royal Society of London. Series A, Containing Papers of a Mathematical and Physical Character **117**, 610 (1928).

[115] P. Hohenberg and W. Kohn, Physical Review **136**, B864 (1964).

[116] W. Kohn and L. J. Sham, Physical Review **140**, A1133 (1965).

[117] D. M. Ceperley and B. J. Alder, Phys. Rev. Lett. **45**, 566 (1980).

[118] J. P. Perdew, K. Burke, and M. Ernzerhof, Phys. Rev. Lett. **77**, 3865 (1996).

[119] F. Bloch, Zeitschrift für Physik **52**, 555 (1929).

[120] P. E. Blöchl, Physical Review B **50**, 17953 (1994).

[121] G. Kresse and D. Joubert, Physical Review B **59**, 1758 (1999).

[122] H. J. Monkhorst and J. D. Pack, Physical Review B **13**, 5188 (1976).

[123] D. J. Chadi and M. L. Cohen, Physical Review B **8**, 5747 (1973).

[124] P. E. Blöchl, O. Jepsen, and O. K. Andersen, Physical Review B **49**, 16223 (1994).

[125] A. Jain *et al.*, APL Materials **1**, 011002 (2013).

[126] J. M. Luttinger and W. Kohn, Physical Review **97**, 869 (1955).

[127] N. Preissler, O. Bierwagen, A. T. Ramu, and J. S. Speck, Physical Review B **88**, 085305 (2013).

[128] J. P. Perdew, Int. J. Quantum Chem **28**, 497 (1985).

[129] J. P. Perdew *et al.*, Proceedings of the National Academy of Sciences **114**, 2801 (2017).

[130] S. L. Dudarev, G. A. Botton, S. Y. Savrasov, C. J. Humphreys, and A. P. Sutton, Physical Review B **57**, 1505 (1998).

[131] G. Trimarchi, Z. Wang, and A. Zunger, Physical Review B **97**, 035107 (2018).

[132] A. V. Krukau, O. A. Vydrov, A. F. Izmaylov, and G. E. Scuseria, The Journal of Chemical Physics **125**, 224106 (2006).

[133] J. W. Gibbs, *Elementary principles in statistical mechanics: developed with especial reference to the rational foundation of thermodynamics* (C. Scribner's sons, 1902).

[134] S. Ping Ong, L. Wang, B. Kang, and G. Ceder, Chem. Mater. **20**, 1798 (2008).

[135] V. Ozoliņš, C. Wolverton, and A. Zunger, Physical Review B **58**, R5897 (1998).

[136] M. K. Aydinol, A. F. Kohan, G. Ceder, K. Cho, and J. Joannopoulos, Physical Review B **56**, 1354 (1997).

[137] S. Kirklin, J. E. Saal, B. Meredig, A. Thompson, J. W. Doak, M. Aykol, S. Rühl, and C. Wolverton, Npj Computational Materials **1**, 15010 (2015).

[138] S. P. Ong *et al.*, Computational Materials Science **68**, 314 (2013).

[139] T. Hahn, U. Shmueli, and J. W. Arthur, *International tables for crystallography* (Reidel Dordrecht, 1983), Vol. 1.

[140] E. A. Nowadnick and C. J. Fennie, Phys. Rev. B **94**, 104105 (2016).

[141] C. T. Capillas, E. S.; de la Flor, G.; Orobengoa, D.; Perez-Mato, J. M.; and Aroyo, M. I., Zeitschrift fur Kristallographie Crystalline Materials **226** (2011).

[142] N. A. Spaldin, J. Solid State Chem. **195**, 2 (2012).

[143] R. D. King-Smith and D. Vanderbilt, Phys. Rev. B **47**, 1651 (1993).

[144] J. H. Lee *et al.*, Nature **466**, 954 (2010).

[145] R. Seshadri and N. A. Hill, Chem. Mater. **13**, 2892 (2001).

[146] J. Young, P. Lalkiya, and J. M. Rondinelli, Journal of Materials Chemistry C **4**, 4016 (2016).

[147] N. A. Benedek and C. J. Fennie, Phys. Rev. Lett. **106**, 107204 (2011).

[148] E. Bousquet, M. Dawber, N. Stucki, C. Lichtensteiger, P. Hermet, S. Gariglio, J. M. Triscone, and P. Ghosez, Nature **452**, 732 (2008).

[149] J. M. Rondinelli and C. J. Fennie, Adv Mater **24**, 1961 (2012).

[150] P. Zuo, C. V. Colin, H. Klein, P. Bordet, E. Suard, E. Elkaim, and C. Darie, Inorg Chem **56**, 8478 (2017).

[151] Y. S. Oh, X. Luo, F.-T. Huang, Y. Wang, and S.-W. Cheong, Nat Mater **14**, 407 (2015).

[152] O. Clemens *et al.*, J. Phys.: Condens. Matter **28**, 346001 (2016).

[153] W. C. Koehler and E. O. Wollan, J. Phys. Chem. Solids **2**, 100 (1957).

[154] S. Ghosh, H. Das, and C. J. Fennie, Physical Review B **92**, 184112 (2015).

[155] J. Alaria *et al.*, Chemical Science **5**, 1599 (2014).

[156] Z. Zanolli, J. C. Wojdeł, J. Íñiguez, and P. Ghosez, Phys. Rev. B **88**, 060102 (2013).

[157] J. Young, A. Stroppa, S. Picozzi, and J. M. Rondinelli, Dalton Trans. **44**, 10644 (2015).

[158] A. Ecija, K. Vidal, A. Larrañaga, A. Martínez-Amesti, L. Ortega-San-Martín, and M. I. Arriortua, Solid State Ionics **201**, 35 (2011).

[159] E. V. Antipov, A. M. Abakumov, and S. Y. Istomin, Inorg. Chem. **47**, 8543 (2008).

[160] P. M. Woodward, E. Suard, and P. Karen, J. Am. Chem. Soc. **125**, 8889 (2003).

[161] A. M. Abakumov *et al.*, J. Solid State Chem. **183**, 2845 (2010).

[162] R. Mishra *et al.*, Nano Lett. **14**, 2694 (2014).

[163] G. Kresse and J. Furthmüller, Physical Review B **54**, 11169 (1996).

[164] J. P. Perdew, A. Ruzsinszky, G. I. Csonka, O. A. Vydrov, G. E. Scuseria, L. A. Constantin, X. Zhou, and K. Burke, Phys. Rev. Lett. **100**, 136406 (2008).

[165] N. Charles and J. M. Rondinelli, Phys. Rev. B **94**, 174108 (2016).

[166] Y. Zhang and M.-H. Whangbo, Inorg. Chem. **50**, 10643 (2011).

[167] P. M. Woodward and P. Karen, Inorg. Chem. **42**, 1121 (2003).

[168] P. M. Woodward and P. Karen, Inorg. Chem. **42**, 1121 (2003).

[169] F. Millange, E. Suard, V. Caignaert, and B. Raveau, Mater. Res. Bull. **34**, 1 (1999).

[170] J. Kanamori, J. Phys. Chem. Solids **10**, 87 (1959).

[171] M. Jansen and U. Wedig, Angew. Chem. Int. Ed. **47**, 10026 (2008).

[172] J. A. Santana, R. Mishra, J. T. Krogel, A. Y. Borisevich, P. R. C. Kent, S. T. Pantelides, and F. A. Reboredo, Journal of Chemical Theory and Computation **13**, 5604 (2017).

[173] M. Y. Shang, C. Y. Zhang, T. S. Zhang, L. Yuan, L. Ge, H. M. Yuan, and S. H. Feng, Appl. Phys. Lett. **102**, 062903 (2013).

[174] E. A. Nowadnick and C. J. Fennie, Phys. Rev. B **94**, 104105 (2016).

[175] R. D. Shannon, Acta Crystallographica Section A **32**, 751 (1976).

[176] P. M. Woodward, Acta Crystallographica Section B Structural Science **53**, 44 (1997).

[177] A. T. Mulder, N. A. Benedek, J. M. Rondinelli, and C. J. Fennie, Advanced Functional Materials **23**, n/a (2013).

[178] A. Zunger, S. H. Wei, L. G. Ferreira, and J. E. Bernard, Phys. Rev. Lett. **65**, 353 (1990).

[179] A. van de Walle *et al.*, Calphad **42**, 13 (2013).

[180] J. E. Saal, S. Kirklin, M. Aykol, B. Meredig, and C. Wolverton, JOM **65**, 1501 (2013).

[181] K. G. Ranmohotti, E. Josepha, J. Choi, J. Zhang, and J. B. Wiley, Adv. Mater. **23**, 442 (2011).

[182] O. Clemens, R. Haberkorn, P. R. Slater, and H. P. Beck, Solid State Sci. **12**, 1455 (2010).

[183] O. Clemens, F. J. Berry, A. J. Wright, K. S. Knight, J. M. Perez-Mato, J. M. Igartua, and P. R. Slater, J. Solid State Chem. **206**, 158 (2013).

[184] J. Rodríguez-Carvajal, M. Hennion, F. Moussa, A. H. Moudden, L. Pinsard, and A. Revcolevschi, Phys. Rev. B **57**, R3189 (1998).

[185] R. J. Cava, B. Batlogg, K. M. Rabe, E. A. Rietman, P. K. Gallagher, and L. W. Rupp, Physica C: Superconductivity **156**, 523 (1988).

[186] G. Deutscher, APL Materials **2**, 096108 (2014).

[187] J. D. Jorgensen *et al.*, Physical Review B **36**, 3608 (1987).

[188] J. Gazquez *et al.*, Advanced Science **3**, 1500295 (2016).

[189] A. Filippetti, G. M. Lopez, M. Mantega, and V. Fiorentini, Physical Review B **78** (2008).

[190] J. D. Jorgensen *et al.*, Physica C: Superconductivity **153-155**, 578 (1988).

[191] J. L. MacManus-Driscoll, J. A. Alonso, P. C. Wang, T. H. Geballe, and J. C. Bravman, Physica C: Superconductivity **232**, 288 (1994).

[192] T. Nishizaki, M. Maki, and N. Kobayashi, Journal of Physics and Chemistry of Solids **69**, 3014 (2008).

[193] T. Nishizaki, K. Shibata, M. Maki, and N. Kobayashi, Journal of Low Temperature Physics **131**, 931 (2003).

[194] M. Maki, T. Nishizaki, K. Shibata, and N. Kobayashi, Journal of the Physical Society of Japan **70**, 1877 (2001).

[195] P. Wisesa, K. A. McGill, and T. Mueller, Physical Review B **93**, 155109 (2016).

[196] L. J. Allen, A. J. D'Alfonso, and S. D. Findlay, Ultramicroscopy **151**, 11 (2015).

[197] N. Roma, S. Morlens, S. Ricart, K. Zalamova, J. M. Moreto, A. Pomar, T. Puig, and X. Obradors, Superconductor Science and Technology **19**, 521 (2006).

[198] X. Obradors, T. Puig, S. Ricart, M. Coll, J. Gazquez, A. Palau, and X. Granados, Superconductor Science and Technology **25** (2012).

[199] R. Ishikawa, E. Okunishi, H. Sawada, Y. Kondo, F. Hosokawa, and E. Abe, Nat Mater **10**, 278 (2011).

[200] J. Gazquez, M. Stengel, R. Mishra, M. Scigaj, M. Varela, M. A. Roldan, J. Fontcuberta, F. Sanchez, and G. Herranz, Phys Rev Lett **119**, 106102 (2017).

[201] N. Gauquelin, D. G. Hawthorn, G. A. Sawatzky, R. X. Liang, D. A. Bonn, W. N. Hardy, and G. A. Botton, Nature Communications **5**, 4275 (2014).

[202] E. Pavarini, I. Dasgupta, T. Saha-Dasgupta, O. Jepsen, and O. K. Andersen, Physical Review Letters **87**, 047003 (2001).

[203] Y. Y. Peng *et al.*, Nature Physics **13**, 1201 (2017).

[204] S. Kim, X. Chen, W. Fitzhugh, and X. Li, Physical Review Letters **121**, 157001 (2018).

[205] P. W. Anderson, Science **279**, 1196 (1998).

[206] S. Kaiser *et al.*, Physical Review B **89**, 184516 (2014).

[207] R. Mankowsky *et al.*, Nature **516**, 71 (2014).

[208] J. Yu, K. T. Park, and A. J. Freeman, Physica C: Superconductivity **172**, 467 (1991).

[209] NREL Best Research-Cell Efficiency Chart. Available at https://www.nrel.gov/pv/cell-efficiency.html (Accessed on February 4, 2020).

[210] C. C. Stoumpos and M. G. Kanatzidis, Adv Mater **28**, 5778 (2016).

[211] C. C. Stoumpos, C. D. Malliakas, and M. G. Kanatzidis, Inorganic Chemistry **52**, 9019 (2013).

[212] Q. Dong, Y. Fang, Y. Shao, P. Mulligan, J. Qiu, L. Cao, and J. Huang, Science **347**, 967 (2015).

[213] M. I. Saidaminov *et al.*, Nat Commun **6**, 7586 (2015).

[214] A. S. Thind, X. Huang, J. W. Sun, and R. Mishra, Chemistry of Materials **29**, 6003 (2017).

[215] Q. Lin, A. Armin, R. C. R. Nagiri, P. L. Burn, and P. Meredith, Nat Photon **9**, 106 (2015).

[216] W. J. Yin, T. Shi, and Y. Yan, Adv Mater **26**, 4653 (2014).

[217] W.-J. Yin, T. Shi, and Y. Yan, Applied Physics Letters **104**, 063903 (2014).

[218] M. H. Du, J. Mater. Chem. A **2**, 9091 (2014).

[219] A. S. Thind, G. Luo, J. A. Hachtel, M. V. Morrell, S. B. Cho, A. Y. Borisevich, J. C. Idrobo, Y. Xing, and R. Mishra, Adv Mater **31**, 1805047 (2019).

[220] J. M. Frost, K. T. Butler, F. Brivio, C. H. Hendon, M. van Schilfgaarde, and A. Walsh, Nano Lett **14**, 2584 (2014).

[221] J. M. Frost, K. T. Butler, and A. Walsh, APL Materials **2**, 081506 (2014).

[222] H. Röhm, T. Leonhard, M. J. Hoffmann, and A. Colsmann, Energy & Environmental Science **10**, 950 (2017).

[223] Y. Kutes, L. Ye, Y. Zhou, S. Pang, B. D. Huey, and N. P. Padture, J Phys Chem Lett **5**, 3335 (2014).

[224] Y. Rakita *et al.*, Proc Natl Acad Sci U S A **114**, E5504 (2017).

[225] L. M. Garten *et al.*, Sci Adv **5**, eaas9311 (2019).

[226] Y. Liu *et al.*, Nat Mater **17**, 1013 (2018).

[227] Z. Fan, J. Xiao, K. Sun, L. Chen, Y. Hu, J. Ouyang, K. P. Ong, K. Zeng, and J. Wang, J Phys Chem Lett **6**, 1155 (2015).

[228] S. G *et al.*, The Journal of Physical Chemistry Letters **7**, 2412 (2016).

[229] G. A. Sewvandi, K. Kodera, H. Ma, S. Nakanishi, and Q. Feng, Sci Rep **6**, 30680 (2016).

[230] O. Yaffe *et al.*, Physical Review Letters **118** (2017).

[231] X. Zhao and N.-G. Park, Photonics **2**, 1139 (2015).

[232] G. P. Nagabhushana, R. Shivaramaiah, and A. Navrotsky, Proc Natl Acad Sci U S A **113**, 7717 (2016).

[233] A. Babayigit, D. D. Thanh, A. Ethirajan, J. Manca, M. Muller, H. G. Boyen, and B. Conings, Scientific Reports **6** (2016).

[234] A. Babayigit, A. Ethirajan, M. Muller, and B. Conings, Nat Mater **15**, 247 (2016).

[235] Y. Li and K. Yang, Energy & Environmental Science **12**, 2233 (2019).

[236] A. S. Thind *et al.*, Chemistry of Materials **31**, 4769 (2019).

[237] M. R. Filip, S. Hillman, A. A. Haghighirad, H. J. Snaith, and F. Giustino, J Phys Chem Lett **7**, 2579 (2016).

[238] E. T. McClure, M. R. Ball, W. Windl, and P. M. Woodward, Chemistry of Materials **28**, 1348 (2016).

[239] A. H. Slavney, T. Hu, A. M. Lindenberg, and H. I. Karunadasa, J Am Chem Soc **138**, 2138 (2016).

[240] G. Volonakis, M. R. Filip, A. A. Haghighirad, N. Sakai, B. Wenger, H. J. Snaith, and F. Giustino, J Phys Chem Lett **7**, 1254 (2016).

[241] X. Huang, S. Huang, P. Biswas, and R. Mishra, Journal of Physical Chemistry C **120**, 28924 (2016).

[242] Z. Xiao, W. Meng, J. Wang, D. B. Mitzi, and Y. Yan, Mater. Horiz. (2017).

[243] W.-J. Yin, B. Weng, J. Ge, Q. Sun, Z. Li, and Y. Yan, Energy & Environmental Science **12**, 442 (2019).

[244] E. Arca *et al.*, J. Am. Chem. Soc. **140**, 4293 (2018).

[245] B. B. Van Aken, T. T. M. Palstra, A. Filippetti, and N. A. Spaldin, Nature Materials **3**, 164 (2004).

[246] K. Maeda and K. Domen, The Journal of Physical Chemistry C **111**, 7851 (2007).

[247] Y.-I. Kim, P. M. Woodward, K. Z. Baba-Kishi, and C. W. Tai, Chemistry of Materials **16**, 1267 (2004).

[248] D. Wan *et al.*, Chemistry of Materials **31**, 2320 (2019).

[249] Y. Wu, P. Lazic, G. Hautier, K. Persson, and G. Ceder, Energy Environ. Sci. **6**, 157 (2013).

[250] I. E. Castelli, T. Olsen, S. Datta, D. D. Landis, S. Dahl, K. S. Thygesen, and K. W. Jacobsen, Energy Environ. Sci. **5**, 5814 (2012).

[251] P. E. D. Morgan, Journal of Materials Science **21**, 4305 (1986).

[252] P. E. D. Morgan, P. J. Carroll, and F. F. Lange, Materials Research Bulletin **12**, 251 (1977).

[253] K. Momma and F. Izumi, J. Appl. Crystallogr. **44**, 1272 (2011).

[254] R. D. Shannon and C. T. Prewitt, Journal of Inorganic and Nuclear Chemistry **30**, 1389 (1968).

[255] L. Ouyang, H. Yao, S. Richey, Y.-N. Xu, and W. Y. Ching, Physical Review B **69**, 094112 (2004).

[256] T. Tohei, H. Moriwake, H. Murata, A. Kuwabara, R. Hashimoto, T. Yamamoto, and I. Tanaka, Physical Review B **79**, 144125 (2009).

[257] Z. J. Huang, Y. Cao, Y. Y. Sun, Y. Y. Xue, and C. W. Chu, Physical Review B **56**, 2623 (1997).

[258] A. S. Thind *et al.*, Chemistry of Materials **31**, 4769 (2019).

[259] A. Walsh, J. L. F. Da Silva, Y. Yan, M. M. Al-Jassim, and S.-H. Wei, Physical Review B **79**, 073105 (2009).

[260] M. R. Filip and F. Giustino, The Journal of Physical Chemistry C **120**, 166 (2016).

[261] S. Kotochigova, Levine, Z.H., Shirley, E.L., Stiles, M.D., and Clark, C.W., 2003).

[262] H. Mizoguchi, H. W. Eng, and P. M. Woodward, Inorganic Chemistry **43**, 1667 (2004).

[263] Y. Yang, M. Yang, Z. Li, R. Crisp, K. Zhu, and M. C. Beard, The Journal of Physical Chemistry Letters **6**, 4688 (2015).

[264] G. H. Wannier, Physical Review **52**, 191 (1937).

[265] A. M. Glass, D. von der Linde, and T. J. Negran, Applied Physics Letters **25**, 233 (1974).

[266] S. Y. Yang *et al.*, Nature Nanotechnology **5**, 143 (2010).

[267] Z. Tan *et al.*, NPG Asia Materials **11**, 20 (2019).

[268] K. Mathew *et al.*, Computational Materials Science **139**, 140 (2017).

[269] B. J. Campbell, H. T. Stokes, D. E. Tanner, and D. M. Hatch, J. Appl. Crystallogr. **39**, 607 (2006).

[270] D. H. Doughty and E. P. Roth, The Electrochemical Society Interface **21**, 37 (2012).

[271] N. Yabuuchi, K. Kubota, M. Dahbi, and S. Komaba, Chemical Reviews **114**, 11636 (2014).

[272] J. C. Pramudita, D. Sehrawat, D. Goonetilleke, and N. Sharma, Advanced Energy Materials **7**, 1602911 (2017).

[273] J. Song, E. Sahadeo, M. Noked, and S. B. Lee, The Journal of Physical Chemistry Letters **7**, 1736 (2016).

[274] D. Kundu, B. D. Adams, V. Duffort, S. H. Vajargah, and L. F. Nazar, Nature Energy **1**, 16119 (2016).

[275] N. Jayaprakash, S. K. Das, and L. A. Archer, Chemical Communications **47**, 12610 (2011).

[276] X. Zhao, S. Ren, M. Bruns, and M. Fichtner, Journal of Power Sources **245**, 706 (2014).

[277] X. Zhao, Z. Zhao-Karger, M. Fichtner, and X. Shen, Angewandte Chemie International Edition **0** (2019).

[278] M. Oka, H. Kamisaka, T. Fukumura, and T. Hasegawa, Computational Materials Science **167**, 92 (2019).

[279] I. Mohammad, R. Witter, M. Fichtner, and M. Anji Reddy, ACS Applied Energy Materials (2018).

[280] V. K. Davis *et al.*, Science **362**, 1144 (2018).

[281] M. A. Nowroozi, K. Wissel, J. Rohrer, A. R. Munnangi, and O. Clemens, Chemistry of Materials **29**, 3441 (2017).

[282] F. Gschwind, G. Rodriguez-Garcia, D. J. S. Sandbeck, A. Gross, M. Weil, M. Fichtner, and N. Hörmann, Journal of Fluorine Chemistry **182**, 76 (2016).

[283] F. Gschwind and J. Bastien, Journal of Materials Chemistry A **3**, 5628 (2015).

[284] C. Rongeat, M. Anji Reddy, R. Witter, and M. Fichtner, ACS Applied Materials & Interfaces **6**, 2103 (2014).

[285] M. Anji Reddy and M. Fichtner, Journal of Materials Chemistry **21**, 17059 (2011).

[286] M. A. Nowroozi and O. Clemens, ACS Applied Energy Materials (2018).

[287] D. T. Thieu, M. H. Fawey, H. Bhatia, T. Diemant, V. S. K. Chakravadhanula, R. J. Behm, C. Kübel, and M. Fichtner, Advanced Functional Materials **27**, 1701051 (2017).

[288] L. Zhang, M. A. Reddy, and M. Fichtner, Journal of Solid State Electrochemistry **22**, 997 (2018).

[289] A. Kraytsberg and Y. Ein-Eli, Journal of Solid State Electrochemistry **21**, 1907 (2017).

[290] K. Lee, S. W. Kim, Y. Toda, S. Matsuishi, and H. Hosono, Nature **494**, 336 (2013).

[291] A. K. Padhi, K. S. Nanjundaswamy, and J. B. Goodenough, Journal of The Electrochemical Society **144**, 1188 (1997).

[292] K. Mizushima, P. C. Jones, P. J. Wiseman, and J. B. Goodenough, Materials Research Bulletin **15**, 783 (1980).

[293] B. Silvi and A. Savin, Nature **371**, 683 (1994).

[294] S. V. Krivovichev, O. Mentré, O. I. Siidra, M. Colmont, and S. K. Filatov, Chemical Reviews **113**, 6459 (2013).

[295] M. Naguib, V. N. Mochalin, M. W. Barsoum, and Y. Gogotsi, Advanced Materials **26**, 992 (2014).

[296] M. A. Nowroozi, B. de Laune, and O. Clemens, ChemistryOpen **7**, 617 (2018).

[297] K. Wissel *et al.*, Journal of Materials Chemistry A (2018).

[298] A. Simon, Coordination Chemistry Reviews **163**, 253 (1997).

[299] K. Omichi, Q. Xu, and C. Brooks, (Google Patents, 2019).

[300] C. Hadenfeldt and H. Herdejürgen, Zeitschrift für anorganische und allgemeine Chemie **545**, 177 (1987).

[301] R. A. Nicklow, T. R. Wagner, and C. C. Raymond, Journal of Solid State Chemistry **160**, 134 (2001).

[302] E. T. Keve and A. C. Skapski, Chemical Communications (London), 829 (1966).

[303] M. Atoji and M. Kikuchi, The Journal of Chemical Physics **51**, 3863 (1969).

[304] D. L. Druffel, M. G. Lanetti, J. D. Sundberg, J. T. Pawlik, M. S. Stark, C. L. Donley, L. M. McRae, K. M. Scott, and S. C. Warren, Chemistry of Materials (2019).

[305] A. Urban, D.-H. Seo, and G. Ceder, npj Computational Materials **2**, 16002 (2016).

[306] G. Henkelman, B. P. Uberuaga, and H. Jónsson, The Journal of Chemical Physics **113**, 9901 (2000).

[307] M. Okubo, Y. Tanaka, H. Zhou, T. Kudo, and I. Honma, The Journal of Physical Chemistry B **113**, 2840 (2009).

[308] Q. Zhu, T. Frolov, and K. Choudhary, Matter (2019).

[309] L. A. Burton, F. Ricci, W. Chen, G.-M. Rignanese, and G. Hautier, Chemistry of Materials **30**, 7521 (2018).

[310] T. Tada, S. Takemoto, S. Matsuishi, and H. Hosono, Inorganic Chemistry **53**, 10347 (2014).

[311] M. M. Menamparambath, J.-H. Park, H.-S. Yoo, S. P. Patole, J.-B. Yoo, S. W. Kim, and S. Baik, Nanoscale **6**, 8844 (2014).

[312] P. A. Anderson, Physical Review **75**, 1205 (1949).

Vita

2012-2016: B. S. Chemistry, Cedarville University, Cedarville, Ohio, USA

2016-2020: Ph. D. Student, Institute of Materials Science and Engineering, Washington University in St. Louis, St. Louis, Missouri, USA

Selected Publications

1. S. T. Hartman, S. B. Cho, and R. Mishra, Multiferroism in Iron-based Oxyfluoride Perovskites. *Inorganic Chemistry* **57**(17), 10616-10624 (2018).
2. S. T. Hartman, B. Mundet, J. C. Idrobo, X. Obradors, T. Puig, J. Gazquez, and R. Mishra, Direct Observation of Apical Oxygen Vacancies in the High-Temperature Superconductor $YBa_2Cu_3O_{7-\delta}$. *Physical Review Materials* **3**(11), 114806 (2019).
3. B. Mundet, S. T. Hartman, R. Guzman, X. Obradors, T. Puig, R. Mishra, and J. Gazquez, Local Strain-Driven Migration of Oxygen Vacancies to Apical Sites in $YBa_2Cu_3O_{7-\delta}$. *Nanoscale* **(**pages not yet assigned, 2020).